



Insight into low-frequency high-magnitude mass movement events using novel luminescence methods in the Pokhara valley [Nepal]

Photo on front page taken by the author during the October 2019 field trip in Nepal

Anna Maartje de Boer

Student number: 960126081070

MSc Earth and Environment

Track: Soil Geography and Earth Surface Dynamics

Wageningen University & Research

Soil Geography and Landscape (SGL) chair group

First supervisor: Tony Reimann (SGL)

Second supervisor: Wolfgang Schwanghart, Potsdam University

Examiner: Jakob Wallinga (SGL)

Submitted: May 2020



Abstract

Researching the origin, dynamics and diversity of Earth's terrain is of high importance, especially in the current era in which humankind has to cope with the effects of climate change on nature and society. Mass movement events are crucial processes in landscape dynamics. Dating and reconstructing mass movement dynamics in high and active mountain ranges is challenging. Luminescence burial dating offers potential in dating these challenging sedimentary settings. However, the commonly used quartz OSL signal is expected to be insensitive in those sedimentary settings due to a combination of short transport distances and recent bedrock erosion. Quartz minerals become more sensitive over repeated cycles of burial and light exposure. Recently, it is proposed that single-grain (pIR)IR luminescence dating of feldspar minerals may be a suitable methodological approach in dating turbid water-lain sediments which have a high chance of poor light exposure during transport and/or deposition. However, a major drawback in this approach is the sensitivity of feldspar minerals to anomalous fading. The goals of this thesis are to assess the applicability of luminescence dating and reconstructing transport dynamics of mass movement processes in an active mountain range. The study is conducted on thick mass movement deposits in the Pokhara valley [Nepal], which provide a unique setting for a case-study. An extensive independent calibrated radiocarbon dataset is used as benchmark for the obtained (pIR)IR burial ages. Moreover, heterogeneous bleaching proxies could presumably provide information on the nature of the paleo-event in the Pokhara valley. Results show that the IRSL50 signal is better bleached than the pIRIR150 signal and therefore more suitable in determining burial ages in catastrophic sedimentary settings. A bootstrapped Minimum Age Model (MAM) is applied to retrieve the youngest subpopulation, which represents the well-bleached grains within the heterogeneous distributions. After correction for anomalous fading, based on a measured fading rate of $7.2 \pm 0.9\%$ /decade, 20% of the IRSL50 burial age samples agrees within their two sigma confidence interval with the average of the calibrated radiocarbon ages of the Pokhara formation at 0.82 ± 0.49 ka (n=26). In similar settings without independent age control, this 20% samples representing the "true burial age" can be distinguished from the other incorrect burial ages by simple statistics. The 20% samples show a higher number of grains contributing to the bootMAM-paleodose and a lower number of grains in saturation than on average. 0% of the pIRIR150 samples agree with the "true radiocarbon burial age". However, as expected, the pIRIR150 signal is a more stable signal with a lower fading rate of $0.89 \pm 0.87\%$ /decade. Burial ages obtained using this signal tend to overestimate by 31.10 ± 8.62 ka, this is on average 6.63 ± 2.18 ka for the IRSL50 signal. While pIRIR150 are less suitable for dating in this environment due to incomplete resetting of the signal, the results are of great use to infer sediment transport processes leading to deposition of the Pokhara formation. The heterogeneous bleaching patterns indicate turbid flow conditions of the water-lain sediments, in which grains were rarely exposed to light resulting in poor-bleaching. The non-spatial correlated results of the saturation proxy - assessing the percentage of grains that were not light exposed during transport - as well as the bootMAM proxy - assessing the percentage of well-bleached grains present - underline the catastrophic nature of the event. The proven applicability of single-grain feldspar in dating and transport reconstructing of young Holocene mass movement deposits, offers potential in future research: in studying similar sedimentary settings, as well as studying geologically older deposits.

Table of Contents

Abstract	3
1. Introduction	6
1.1 Luminescence dating	8
1.2. Potential of luminescence in dating and reconstructing mass movement processes	8
1.3. Unique field setting: the Pokhara valley	10
1.4. Research objectives and questions	12
2. Luminescence background	13
2.1. Principles of luminescence dating.....	13
2.1.1. Optically Stimulated Luminescence (OSL).....	13
2.1.2. (Single-grain) post-infrared infrared dating (pIRIR).....	16
2.1.3. Assessing luminescence burial dating by the use of independent dating proxies	18
2.2. Luminescence as a process reconstruction tool	18
2.2.1. Bleaching	19
2.2.2. Saturation	20
2.2.3. Spatial analysis.....	20
3. Site description	21
3.1. General information	21
3.2. Geology of the Pokhara Valley	22
3.3. Pokhara valley sedimentary infill	23
4. Methods.....	25
4.1. Sampling	25
4.2. Experimental details	28
4.3. Data analysis	30
4.3.1. Dating	31
4.3.2. Reconstructing sediment dynamics.....	32
5. Results.....	33
5.1. Sedlogs and river network analysis	33
5.2. Dating	34
5.2.1. Dose recovery ratio.....	34
5.2.2. De-distributions	34
5.2.3. Burial ages and fading rates.....	38

5.2.4. Radiocarbon overestimation ratio	40
5.3. Reconstructing sediment dynamics	42
5.3.1. Saturation proxy	42
5.3.2. BootMAM proxy	43
6. Discussion	44
6.1. Potential of luminescence dating in catastrophic settings.....	44
6.2. Potential of luminescence in reconstructing mass movement processes	47
6.3. Local sediment dynamics of the Pokhara valley	48
7. Conclusions.....	50
8. Recommendations.....	51
Acknowledgments	52
References	53
Appendix.....	59
Appendix I: Measurement sequences	59
Appendix II: Radial plots	60
Appendix III: Kernel Density plots	64
Appendix IV: Sedimentary logs	68
Appendix V: Snapping distance.....	75

1. Introduction

Environmental awareness made that landscape evolution theories and modelling are prominently present on the contemporary scientific research agenda. Researching the origin, dynamics and diversity of Earth's terrain is of high importance, especially in the current era in which humankind has to cope with the effects of climate change on nature and society (Tucker & Hancock, 2010). Low-frequency high-magnitude landmass movement events are crucial processes in landscape dynamics. Several study fields of physical geography are concerned with retrieving in-depth knowledge of sedimentary transport mechanisms: by studying sediment budgets (Rosati, 2005), sediment provenance (Weltje & von Eynatten, 2004) and by conducting sediment erosion and transport modelling studies (Merritt *et al.*, 2003). Insight into sediment transport mechanisms is key in understanding (local) landscape evolution.

The interplay between tectonic and climatic influence controls how landscapes evolves, especially in the study area of this thesis: the Himalayas (Anoop *et al.*, 2012). The Himalayas function as an orographic barrier and in combination with the Indian summer monsoons, makes the region susceptible for landsliding (Bookhagen *et al.*, 2005a). Moreover, high denudation and precipitation rates form additional triggering factors in the process of landslide formation. In the context of climate change it is shown that high climatic variability led to a five times higher sediment-flux in the Himalayas at earlier stages of geological history (Bookhagen *et al.*, 2005b). High sediment-fluxes cause direct local impact in the form of mass movements, thereby threatening local societies (Rimal *et al.*, 2015). Besides local impact, global impact is profound by the high denudation rates which are coupled to high weathering levels of Himalayan parent rock. Carbon dioxide is stored within rocks and released upon rock weathering into the atmosphere. This positive feedback loop enhances climate instability (Taylor *et al.*, 2016). Researching local sediment dynamics is thus of life importance for local as well as global society in coping with direct and indirect effects of climate change.

The study field of geochronology focusses on retrieving absolute ages of (paleo-) deposits in order to untangle landscape dynamics and plays an important role in developing landscape evolution theories (Walker, 2005). Various geochronological (absolute) dating methods are in common use to date sediment exposure and/ or burial ages, such as: radiocarbon, luminescence, annual counting (varves or ice layers), tephrochronology, U/Th dating, fallout radionuclides, dendrochronology and cosmogenic nuclide dating. Those methods operate at specific temporal and spatial scales (figure 1), therefore not always suitable for dating in specific settings (G. Duller, 2000; Walker, 2005). In dating mass movement deposits, several methods are a feasible option: radiocarbon, luminescence and/ or exposure dating. In order to acknowledge the two main research goals of this study, luminescence techniques are applied. Luminescence burial dating has the potential to determine the age of the dynamic mass movement event. On top of that, luminescence techniques can be of value in reconstructing sedimentary processes and eventually contribute to landscape evolution theories.

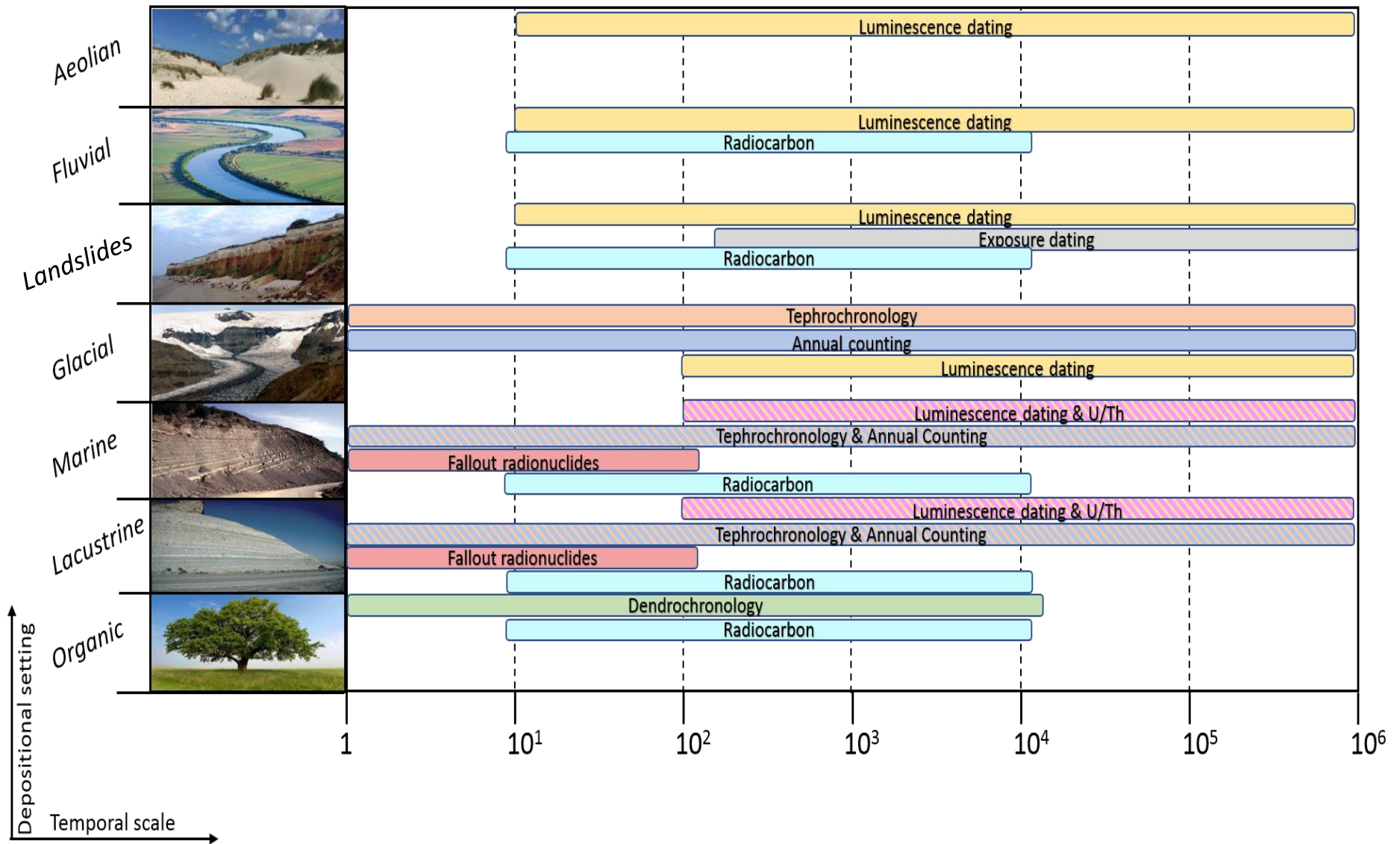


Figure 1: Overview of the applicability of dating methods on varying temporal scales and in different environmental settings. Data retrieved after (Walker, 2005 and Rhodes, 2011).

1.1 Luminescence dating

Deriving landscape dynamics and dating of mass movement deposits originating from high, dynamic and active mountain ranges is not straightforward. However, several studies showed the potential of the use of luminescence techniques in dating mass movement deposits (Eriksson *et al.*, 2000; M. Fuchs *et al.*, 2010; Tatumi *et al.*, 2003). As shown in figure 1, not all environmental depositional settings are suitable for luminescence dating. Aeolian deposits are ideal: it can be expected that sediment is well bleached because of aeolian transport mechanisms and therefore results are less prone to age overestimation (Thomsen *et al.*, 2016). For non-aeolian environments it can be more difficult to apply luminescence techniques because of low luminescence sensitivity (Markus Fuchs & Owen, 2008) and poor bleaching effects leading to age overestimation (Hu *et al.*, 2015). The term bleaching describes the removal of trapped atomic charge by light exposure. If sediment is poorly bleached, not all trapped charge is removed and therefore the sample carries an inherited signal (Rhodes, 2011). Hence, luminescence dating is universally applied and often concentrated in aeolian depositional environments (Rhodes, 2011; Walker, 2005). An interesting challenge, in developing the potential of luminescence dating and sediment tracing and/ or reconstruction techniques, lies in dynamic (high mountainous) environments (Bonnet *et al.*, 2019; Brill *et al.*, 2018; Catto, 2019; Chamberlain & Wallinga, 2019).

1.2. Potential of luminescence in dating and reconstructing mass movement processes

In 1985 the first research about optically stimulated luminescence (OSL) was published in the context of geosciences thereby proposing a new technique for dating sediments (Huntley *et al.*, 1985). This field of research developed quickly and is nowadays a common geochronological method to establish sediment burial ages (Aitken, 1998; Bøtter-Jensen *et al.*, 2003; Rhodes, 2011; Ann G. Wintle, 2008). Over the past decades research has focussed on developing and fine-tuning different luminescence procedures, such as OSL, infra-red stimulated luminescence (IRSL), thermoluminescence (TL) as reviewed in (Rhodes, 2011) and post-infrared infrared-stimulated (pIRIR) luminescence dating (Thomsen *et al.*, 2008). In the field of TL dating, the sample is not stimulated optically but by heating of the sample. Whilst OSL, IRSL and pIRIR dating are based on optical stimulation. The luminescence signal of IRSL and pIRIR is stimulated by infrared and the OSL signal by optical light sources (Rhodes, 2011). The IRSL is the initial part (lower temperature) of the signal, whereas the pIRIR is the later part (higher temperature) of the signal (Thomsen *et al.*, 2008). Furthermore, the research focus has been on comparing multiple-grain versus single-grain dating methods and laying bare their potential and limitations (Bonnet *et al.*, 2019; G. A. T. Duller, 2008).

With the advancement of luminescence techniques, it is more often proposed in literature that pIRIR is a suitable methodological approach in dating poorly light-exposed dynamic sampling locations (Bonnet *et al.*, 2019; Reimann *et al.*, 2012). Several studies show that if convenient quartz OSL dating is not applicable for mass movement deposits and/ or in dynamic high mountain ranges, that pIRIR dating could be a successful alternative (Sawakuchi *et al.*, 2018; R. K. Smedley, 2014; Tatumi *et al.*, 2003). The advantage of pIRIR dating in those settings lies in the use of feldspar versus quartz minerals and in measuring on single-grain level instead of multigrain level.

First of all, mass movement deposits are (on geological timescales) freshly eroded from the bedrock. This entails that quartz minerals are often less sensitive than feldspar minerals (G. A. Duller, 2006; Preusser *et al.*, 2006) and that the quartz signal sensitivity is often strongly varying over sedimentary

settings (Preusser *et al.*, 2009). In mountainous areas, such as the Himalayas, freshly eroded quartz often shows very poor luminescence sensitivity (Jaiswal *et al.*, 2009). In other words: feldspar minerals from plutonic or metamorphic bedrock are more sensitive to bear a measurable luminescence signal and have a stronger inherited signal than quartz minerals (Guralnik *et al.*, 2015).

Secondly, the transport distance from the bedrock to the depositional environment plays a major role. Short spatial transport distances can result in poorly bleached samples. Especially feldspar minerals are prone to poor bleaching on short spatial scales (Reimann *et al.*, 2012). The luminescence signal in feldspar minerals is reset by exposure to sunlight at slower rates than in quartz minerals (Thomsen *et al.*, 2008). This drawback of poorly bleached samples can possibly be overcome by the application of single-grain instead of multi-grain measurement techniques. Single-grain data analysis enables to distinguish between well-bleached and poorly-bleached grains within samples (G. A. T. Duller, 2008). For poorly bleached samples – insufficient light exposure to reset the luminescence signal - single-grain dating could systematically yield less age overestimation. On single-grain level it is distinguishable which grains capture the “true burial age” and which grains inherit a poorly bleached signal. By the use of statistical modelling, like the Minimum Age Model (MAM), studies showed that single-grain dating can be decisive in overcoming age overestimation (Brill *et al.*, 2018; A. S. Murray *et al.*, 2012).

By the same token, it is demonstrated that the pIRIR luminescence signal can produce burial age data for relatively young sediments (Madsen *et al.*, 2011; Reimann *et al.*, 2011). Still, only several studies have been researching single-grain pIRIR applications (Reimann *et al.*, 2017; Reimann *et al.*, 2012; R. Smedley *et al.*, 2015; Thomsen *et al.*, 2016; Thomsen *et al.*, 2008). The usage of single-grain pIRIR dating seems promising, however feldspar minerals are prone to anomalous fading, which is a major drawback in using feldspar signals for dating sediments. Nonetheless, recently developed approaches can correct for the age underestimation effects of anomalous fading on burial age determination (Li *et al.*, 2014; Reimann *et al.*, 2012; Roberts, 2012; Thomsen *et al.*, 2008). All in all, this young study field offers opportunities in dating mass movement deposits from dynamic mountainous areas.

On top of that, recent scientific research (Bonnet *et al.*, 2019; Chamberlain & Wallinga, 2019; Gray *et al.*, 2019; Reimann *et al.*, 2015; Riedesel *et al.*, 2018) showed that luminescence – especially single-grain approaches – is more than only a dating technique. Heterogeneous bleaching can be used to unravel past sediment dynamics. It is shown that not only single-grain quartz (G. A. T. Duller, 2008) but also single-grain feldspar methods are promising in tracing and reconstructing sediment dynamics of geologically young sediments (Riedesel *et al.*, 2018).

1.3. Unique field setting: the Pokhara valley

The flat sediment body in the Pokhara valley [Nepal], connected to a big drainage basin upwards in the Annapurna Massif of the Himalayan mountains, is an excellent example of a low-frequency high-magnitude mass movement relict (Schwanghart *et al.*, 2016; Stolle *et al.*, 2017). The Pokhara sedimentary valley has a length of over 70 kilometres and is filled with mass movement deposits. Nepal's second largest city – Pokhara - is located on top of this mass movement body (figure 2).

The origin of those gravels is heavily debated in literature and several theories have passed under review over the years. The earliest one is from 1969 and interprets the valley deposits as a former lake basin (Hagen, 1969), which is commonly seen in the valley of Kathmandu. Others linked the gravels as lacustrine deposits to river damming (Hormann, 1974). Subsequent studies, however, dated the deposits by radiocarbon dating and started doubting the suggested Pleistocene origin of the gravels (Fort, 1984; Yamanaka, 1982). Radiocarbon results indicated Late-Holocene origin, for the first time conclusions were drawn that seismic activity could be one of the causes of Pokhara gravel presence far downstream in the valley (Fort, 1987). Calibration of the available radiocarbon data in order to link the data with the historic record of major seismic events, made that research results followed a commonly agreed line in acknowledging seismic trigger as possible explanation of the valley infill origin (Fort, 2010; Hanisch & Koirala, 2010). An extensive new radiocarbon dataset in combination with recalibration of all old available radiocarbon data plus a detailed sedimentological interpretation of the debris flow and a sediment provenance analysis, led to the well-substantiated interpretation made by (Schwanghart *et al.*, 2016).

Schwanghart (2016) pointed out that seismic activity is highly likely the triggering mechanism behind the mass movement. That study linked the deposition age of the radiocarbon dated sediment bodies, to historical sources of earthquake activity (Schwanghart *et al.*, 2016). Supplementary independent geochronological datasets could affirm the nature of the catastrophic event with more confidence. This unique setting, with an extensive calibrated radiocarbon dataset as benchmark, could be augmented by luminescence research. As argued in section 1.1., single-grain pIRIR luminescence is a promising approach to obtain “true burial age data” despite the dynamic mountainous setting. Augmenting a burial age dataset with pIRIR dating has been conducted previously (Reimann *et al.*, 2012; Sohbaty *et al.*, 2016), although not for dynamic mountainous settings as the mass movement deposits in the Pokhara valley. In general there is a lack of luminescence burial data for deposits in and around the Himalayan mountain range (Hu *et al.*, 2015). Besides obtaining an independent burial age dataset, pIRIR measurements of the mass movement infill have the potential to unravel the dynamic history of the event by studying bleaching rate variations over the fan apex.

High uplift rates and seismic activity in the Himalaya is accompanied by rapid erosion rates which makes sediment available for transport and creates instable sedimentological conditions (Lavé & Avouac, 2001). Tectonic activity is quantified by mountainous uplift rates derivable from luminescence data on a global scale and/ or from basin wide erosion rates (Choi *et al.*, 2009; Cunha *et al.*, 2008; M Fuchs & Lang, 2001). Application of OSL thermochronometry in the eastern Himalayas, showed the ability to derive exhumation rates over the past million years (King *et al.*, 2016). However, several studies indicated that there is a lack of uplift rate research in the Pokhara valley (Fort, 1996; Gabet *et al.*, 2008;

Jackson & Bilham, 1994). The ramp-flat-ramp geometry of the Pokhara valley is suggested to be the cause for high local uplift rates in the Higher Himalayas and lower uplift rates in the Lesser Himalayas (Avouac, 2015). The tectonically instable Himalayas and frequent occurrence of major earthquakes (Bungum *et al.*, 2017), make that the big sediment budget available from the Himalayas can be a threat to the city of Pokhara. In addition, the presence of a seismic gap in the Central Himalayas, makes the study area prone to prospective seismic events which can be damaging in combination with the steep topography (Rajendran *et al.*, 2017). Getting insight into (earthquake-triggered) paleo-mass movement deposits and their dynamics can be of life importance for a city like Pokhara. In recent years the city of Pokhara is expanding quickly, thereby stressing its environment and increasing natural hazard risks (Rimal *et al.*, 2015). Geochronological and geomorphological knowledge about the Pokhara valley can be of help in natural hazard risk assessment. Subsequent modelling studies are vital for a city with rapid demographic transitions in one of the world’s highest and sharpest relief contrasted mountain ranges.

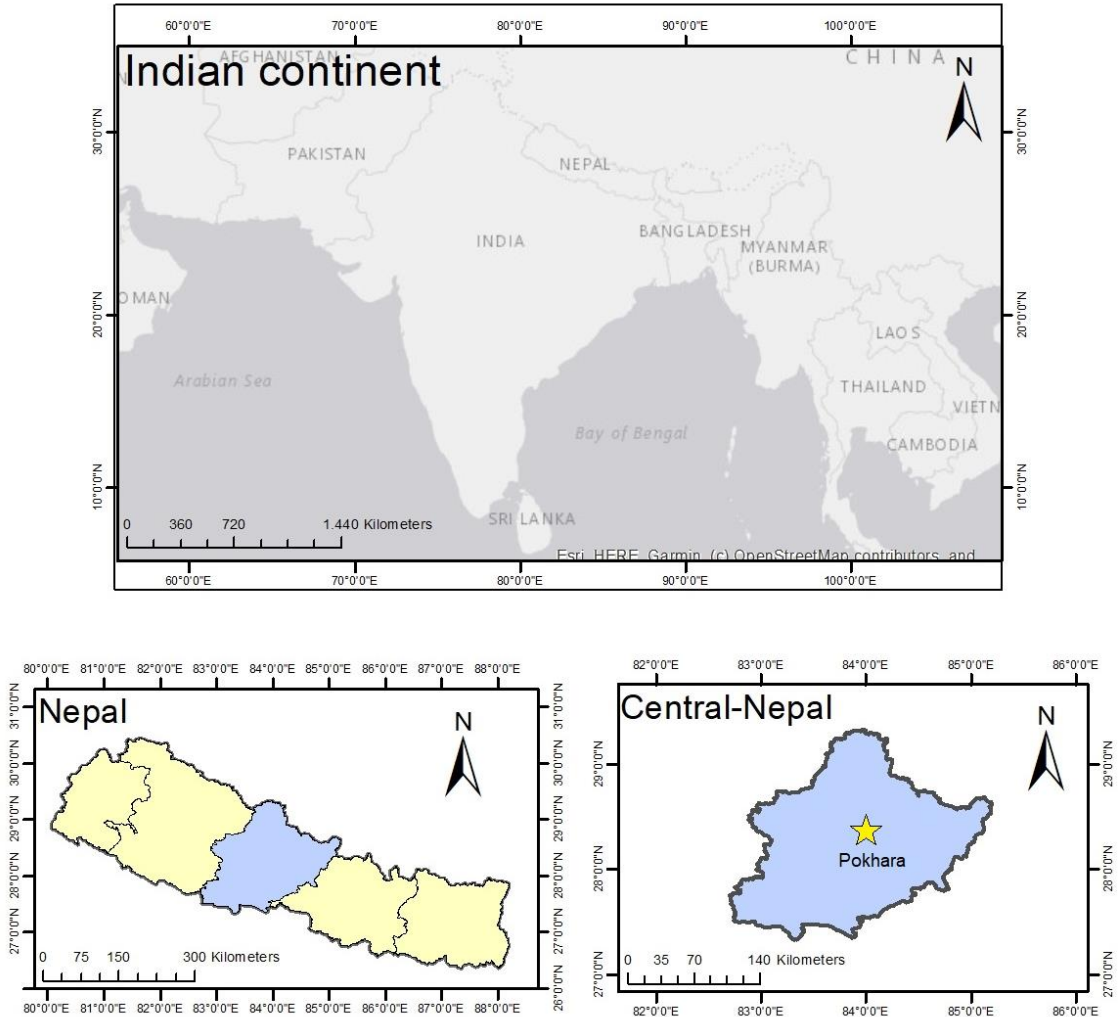


Figure 2: Map of the study area: Nepal is located north of India and borders China and Bhutan. The Pokhara valley is located in Central-Nepal, just southwards of the Himalayan mountain range.

1.4. Research objectives and questions

This study serves methodological and applied research objectives, in total four objectives are indicated:

1. Methodological: assessing the applicability of single-grain (pIR)IR luminescence dating in a dynamic high mountain range setting by the use of standardized protocols (Thomsen *et al.*, 2008).
2. Methodological: studying the potential of reconstructing mass movement processes by the use of luminescence techniques.
3. Applied: obtaining burial ages of the Pokhara valley-infill in Central-Nepal.
4. Applied: unveiling landscape dynamics of the event-driven Pokhara valley-infill deposits.

The research questions are aggregated, according to methodology or application, into two main research questions which are in turn subdivided into several sub questions.

“Is single-grain feldspar dating suitable in studying the timing and process dynamics of catastrophic mass movement deposits in highly dynamic mountainous settings such as the Pokhara valley [Nepal]?”

- Are IR50 and/ or pIRIR150 luminescence signals valid burial age indicators in highly dynamic mountainous settings?
- What signals and proxies can be used to derive information on process dynamics of mass movement deposits?
- To what extent does poor bleaching affect the validity of single-grain feldspar dating for low-frequency high-magnitude events on different timescales?

“Does luminescence dating and process reconstruction succeed to unveil the age and the local landscape dynamics of the Pokhara valley [Nepal]?”

- What is the luminescence burial age of the Pokhara and Ghachok formation?
- Is there a systematic difference between the luminescence burial ages and calibrated radiocarbon ages for the Pokhara deposits?
- What information do parameters related to heterogeneous bleaching yield with regard to the event dynamics of the Pokhara formation?
- What do the process reconstruction results of the Pokhara case-study imply for application in other low-frequency high-magnitude settings?

2. Luminescence background

2.1. Principles of luminescence dating

2.1.1. Optically Stimulated Luminescence (OSL)

Optically Stimulated Luminescence (OSL) is used to date when a sand grain (mineral) has last been exposed to light, in other words: the moment of sediment burial is measured. Minerals like quartz or feldspar, are able to store energy within their crystal lattices and can release that energy upon light or heat stimulation. This process is similar to the functioning of a battery (figure 3): trapped charge can be released by daylight exposure of sediments (or heat stimulation) in the natural environment, the battery is emptying (figure 3, 1A). If sediments are buried, light exposure will be cut off and a trapped charge can build up in the minerals (battery) under the influence of the environmental ionizing radiation (figure 3, 1B). The buried sediments can be sampled for OSL dating and the luminescence signal can be measured in the lab by evicting the trapped charge with light stimulation (optical dating) or heat stimulation (thermal dating), the battery is emptied again (figure 3, 1C) (Rhodes, 2011; Walker, 2005).

Figure 3 conjointly contains the energy band gap model in comparison to the battery analogue to get a good grip on luminescence dating. The first figure in-set (figure 3, 2A) shows the initial situation. The electrons traps are filled, although at room temperature low thermal stability traps close to the conduction band are empty and hole centres (luminescence centres) are available (Rhodes, 2011). On light exposure the traps can be cleared out (bleaching) and the electrons can recombine at luminescence centres or get trapped elsewhere via the conduction band (figure 3, 2B). The degree of bleaching depends on the intensity and duration of the (sunlight) exposure (R. K. Smedley, 2014). In absence of light, i.e. after burial of the sediment, environmental ionising radiation initiates electron-hole pair production and some are trapped in the minerals crystal lattice at the created point defects (figure 3, 2C). Over time the OSL signal gradually builds up. Electron lifetime depends on leakage of electrons from their traps. The lifetime has to be sufficient in order to neglect the leaking effect. The distance between the trap and the conduction band is the determining factor in electron lifetimes (R. K. Smedley, 2014). After sampling the electrons can be evicted from their traps by intense light stimulation in a laboratory, thereby emitting UV luminescence for quartz minerals and blue light (410 nm) if assessing feldspar minerals. A photomultiplier tube detects the OSL signal (figure 3, 2D) (Rhodes, 2011). Afterwards varying laboratory radiation doses (regeneration-doses) are applied in order to calibrate the emitted natural luminescence signal and determine the equivalent dose in the grain (D_e) from the dose-response curve (R. K. Smedley, 2014).

The single aliquot regenerative-dose (SAR) protocol is often applied and originally developed for quartz studies (Murray & Wintle, 2000, 2003), later also tailored to feldspar IRSL techniques (Thomsen *et al.*, 2008). The dose-response curve includes regenerative-doses but also test-doses in order to obtain a sensitivity-correlated luminescence signal. The natural luminescence signal is normalized by the test-dose (L_n/T_n), the same procedure is valid for the regenerative-doses (L_x/T_x). Those parameters are plotted in the dose-response curve: the L_x/T_x values are interpolated and the D_e value in Gray (Gy) is shown at the crossing point with the L_n/T_n line (figure 4) (Wallinga, 2002).

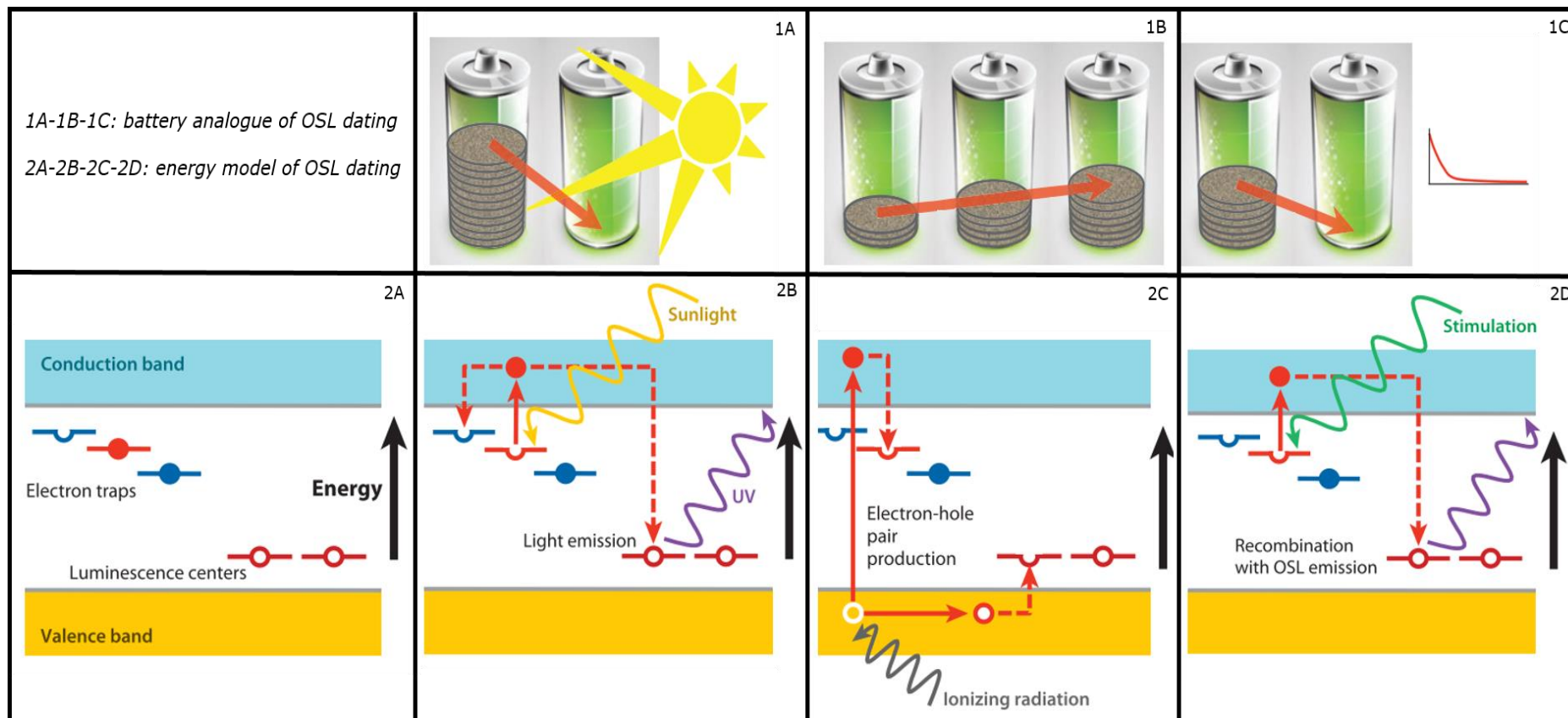


Figure 3: Battery analogue (1A, 1B, 1C) and energy band gap model (2A, 2B, 2C, 2D) of OSL dating after Rhodes, 2011. The type of signal detection is dependent on the mineral selection: signal emission in the form of UV corresponds with quartz minerals and signal emission in the form of blue light (410 nm) corresponds with feldspar minerals (preference of this study).

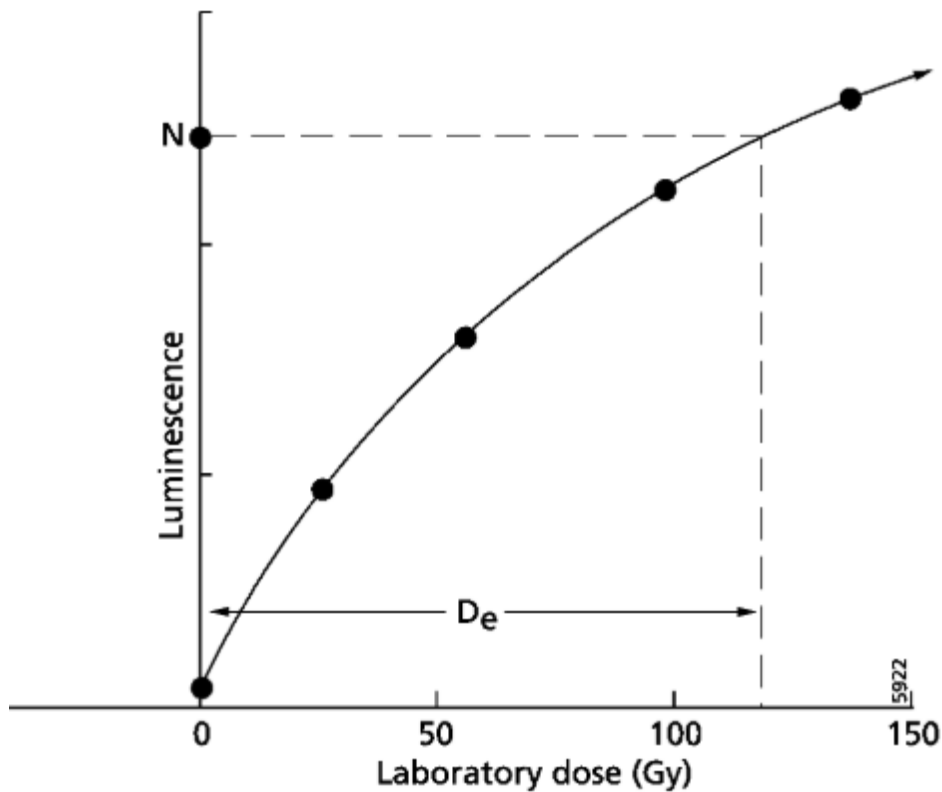


Figure 4: The dose response curve shows the sensitivity-corrected natural dose (L_n/T_n) on the x-axis and the sensitivity-corrected regenerative doses on the y-axis (L_x/T_x). The corresponding D_e value is indicated by the arrow range (Wallinga, 2002). The recycling ratio assesses the sensitivity correction, whereby the final sensitivity-corrected dose (L_7/T_7) should equal the start sensitivity-corrected dose (L_2/T_2). The recycling ratio is in an ideal case equal or close to one (Rhodes, 2011). Another test of the SAR protocol is the dose recovery test (Ann G Wintle & Murray, 2006). The natural signal is zeroed and each sample receives a known laboratory dose, a full SAR measurement protocol is conducted to assess whether the given dose is obtained back (Rhodes, 2011). A dose recovery test can also indicate if there is a non-bleachable residual component within the obtained luminescence signal. Moreover, the SAR protocol includes the zero dose cycle which assesses the influence of charge transfer processes like recuperation. Recuperation is charge movement triggered by light exposure to less stable traps before thermal transfer influence; both transfer types can increase the measured equivalent dose values (Rhodes, 2011).

An interpretation of all D_e -values is made in order to obtain the paleodose [Gy] per sample, models applied differs per field setting. Besides this paleodose, the environmental dose rate (D_r) should also be retrieved. The dose rate depends on the amount of radiation each mineral grain has been exposed to during burial, coming from radioactivity decay (α -, β -, γ -radiation) and cosmic rays. The dose rate is measured in Gray per kilo annum [Gy/ka] in the laboratory from sediment directly sampled around the sample in its natural environment. To calculate the burial age of the sample, the estimated paleodose is divided by the retrieved dose rate:

$$\text{Luminescence age (ka)} = \frac{\text{Paleodose (Gy)}}{D_r \left(\frac{\text{Gy}}{\text{ka}} \right)}$$

2.1.2. (Single-grain) post-infrared infrared dating (pIRIR)

In this study it is chosen to use K-feldspars for dating. K-feldspars have high intrinsic brightness, which means that they are more sensitive than quartz minerals and have an improved minimum detection limit (Thomsen *et al.*, 2008). Intrinsic brightness is probably due to crystal defects in the mineral and trace impurities (Krbetschek *et al.*, 1997). Furthermore, feldspar signals can grow larger doses and they are sensitive to infrared stimulation (Hütt *et al.*, 1988; M Jain *et al.*, 2005). Of higher importance for this study is the theory that feldspar minerals might be more sensitive to bleaching under subaquatic conditions than quartz minerals. Bleaching mechanisms would function quicker without blue and UV light stimulation due to the subaquatic conditions (Ollerhead & Huntley, 2011). However, when dating feldspar minerals there are several points of attention that should be taken into account in comparison to quartz dating.

1. Signal stability: the major drawback of feldspar dating is anomalous fading, which describes the a-thermal loss of luminescence signal over burial time. Electrons are evicted from thermally stable traps without light or heat stimulation (Spooner, 1994; Thomsen *et al.*, 2008; Ann G Wintle, 1973). Anomalous fading depends on several recombination patterns possible within the K-feldspar lattice (see next paragraph) (Mayank Jain & Ankjærgaard, 2011). Thomsen (2008) studied several stimulation types and temperatures in order to understand the influence of anomalous fading rates on the emitted luminescence signal. The fading rate of the initial part (IRSL) of the luminescence signal is greater than for late part (pIRIR), since the signal from the second part of the decay curve is more stable. The luminescence signal of the decay curve is also more stable after stimulation at higher temperatures. The pIRIR signal shows lower anomalous fading rates because it is stimulated at higher temperatures than the IRSL signal. Moreover, K-feldspars are better suitable for dating than Na-feldspars because of their lower anomalous fading rates (Thomsen *et al.*, 2008).
2. More and different recombination routes in K-feldspar lattice: the band gap model (figure 3) is not representative for electron behaviour in feldspar minerals. In K-feldspar grains, recombination of electrons with luminescence centres can happen via different recombination routes as opposed to recombination within quartz grains. The feldspar luminescence model as shown in figure 5 is developed by (Mayank Jain & Ankjærgaard, 2011). The model shows that the luminescence signal of feldspars strongly depends on the distance (parameter r in the diagram) between the donor (trap) - acceptor (recombination centre) pairs. The most important message to get from this figure is the several recombination routes possible, indicated by the letters a till f. Where a and b represent thermal and optical excitations, respectively, which are also common in quartz dating. Especially, d and e are typical for IRSL signals from feldspar minerals: electron transfer from excited to lower band-tail states under the conduction band (d) and tunnelling to a recombination centre (e) (Mayank Jain & Ankjærgaard, 2011; Thomsen *et al.*, 2008). The IRSL and pIRIR signal behave differently: IRSL signal preheating of 50°C mostly recombines proximal donor-acceptor pairs, whilst in the second signal (pIRIR) the more distal donor-acceptor pairs are reached; which contributes to signal stability (Mayank Jain & Ankjærgaard, 2011) and therefore a lower anomalous fading rate (Thomsen *et al.*, 2008).

3. Density separation and internal K-content: there are a lot of different feldspar types ranging from Orthoclase to Albite (alkali feldspars) to Anorthite (plagioclase feldspars), the types change with chemical composition. In preparing a sample for luminescence dating, density separation is conducted in order to separate the different minerals from each other. K-feldspars and Na-feldspars have different internal luminescence properties. A bright Na-feldspars luminescence signal can influence a K-feldspar measurement, even if the normal wavelength peak of Na-feldspars is lower (400 nm) than for K-feldspars (570 nm) (Krbetschek *et al.*, 1997; R. K. Smedley, 2014). Density separation is thus very important to prevent sample contamination. However, it is shown that commonly used density separation methods are not perfect (D. Godfrey-Smith & Cada, 1996; R. K. Smedley, 2014; Thomsen *et al.*, 2008).
4. Poor bleaching due to slow signal resetting: the initial quartz signal bleaches faster than the initial feldspar signal. The bleaching behaviour of feldspar grains is often more incomplete (D. I. Godfrey-Smith *et al.*, 1988; Thomsen *et al.*, 2008). Therefore it is expected that multi-grain feldspar analysis will not capture the true burial age (Reimann *et al.*, 2011), but leads to age overestimation (Hu *et al.*, 2015). To obtain the burial age and discriminate a possible inherited signal, measurements on single-grain level are needed in order to be able to identify well-bleached grains within the feldspar fraction (Reimann *et al.*, 2012; Reimann *et al.*, 2011).

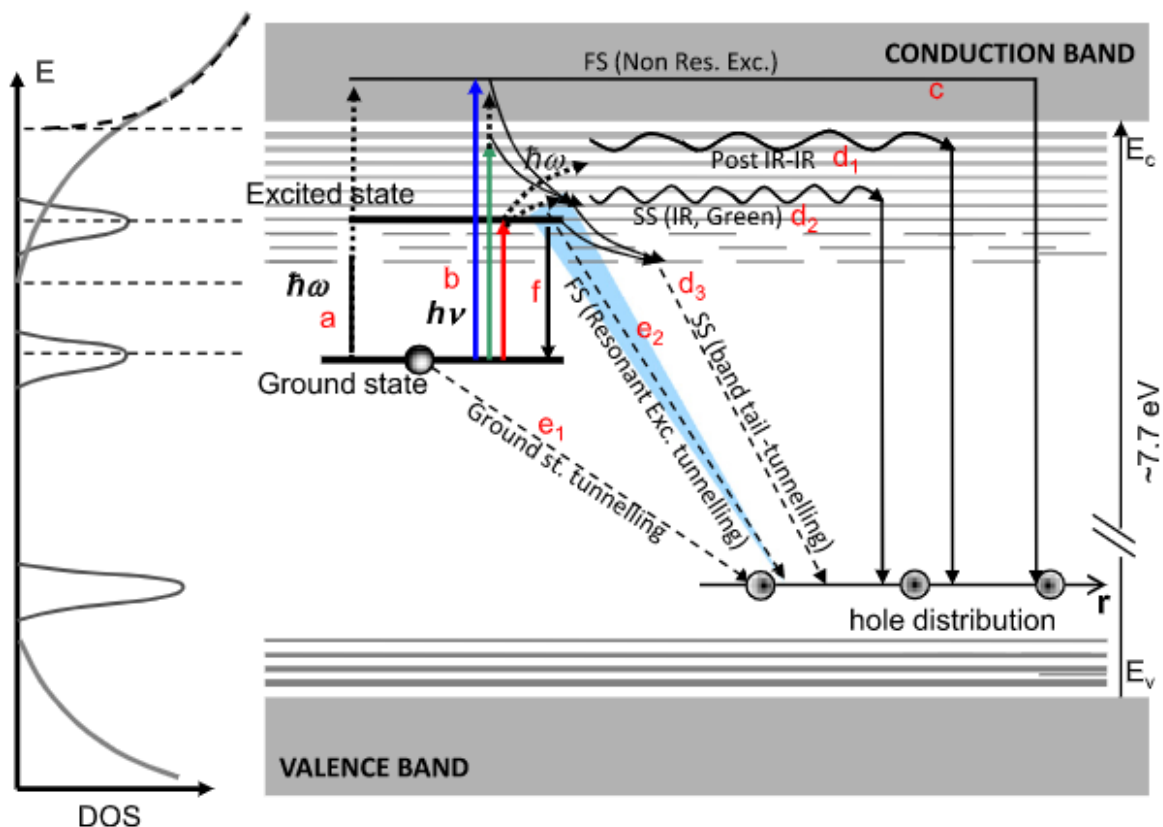


Figure 5: Distribution of density states (DOS) on the left and the band model for K-feldspars on the right. Where letters a till f show the different recombination routes possibly within the feldspar crystal lattice: a. thermal excitations, b. optical excitations, c. recombination throughout conduction band, d. transitions from band tail states, e. tunnelling from ground state and f. retrapping. The y-axis represents the distance (not on scale) between donor-acceptor pair recombination (Jain & Ankaergaard, 2011).

2.1.3. Assessing luminescence burial dating by the use of independent dating proxies

Radiocarbon overestimation ratio

As this is one of the first studies to apply luminescence dating for such catastrophic sedimentary environments of freshly eroded material in the Himalayas (Hu *et al.*, 2015), it is important to carry out independent chronological age control. The availability of the extensive radiocarbon dataset by Schwanghart *et al.* (2016), enables verification of the results obtained with the applied single-grain (pIR)IR protocol (Reimann *et al.*, 2012). Radiocarbon ages are often used as independent datasets in the substantiation of luminescence dating results (M. Fuchs *et al.*, 2010; Riedesel *et al.*, 2018).

In this study the radiocarbon dataset is explicitly used as the benchmark dataset; the extensiveness, quality and agreement within that dataset makes it a reliable benchmark. Regarding the expected event dynamics, radiocarbon samples from fallen trees and/ or other plant material do highly likely have a causal link with the event: it is well-possible that this extreme event collected a lot of organic material in its way into the valley, which became stored within the mass movement deposits. The ¹⁴C chronology is introduced in the form of a radiocarbon overestimation ratio: this ratio is applied as a proxy in measuring the possible overestimated luminescence age against the radiocarbon dataset. By introducing this proxy, the validity of the obtained luminescence burial ages can be addressed and thereby the burial age of the Pokhara debris flow deposits.

Local stratigraphy

The second proxy on the stratigraphic record of the sediment body, can contribute in assessing if the luminescence burial ages corresponds to the relative burial ages as derived from local stratigraphic layering. The local stratigraphy was described at every sampling location during the field trip and is displayed by establishing sedimentary logs (Appendix IV). Further assessment of this proxy is substantiated by the detailed sedimentary descriptions of the Pokhara gravels by Stolle (2017).

2.2. Luminescence as a process reconstruction tool

Recent ongoing developments in the application of luminescence techniques introduced the method as a sediment tracer, sediment provenance and as a process reconstruction tool (Bonnet *et al.*, 2019; Brill *et al.*, 2018; Chamberlain & Wallinga, 2019; Chamberlain *et al.*, 2017; Gray *et al.*, 2019; Gray *et al.*, 2017; McGuire & Rhodes, 2015; Reimann *et al.*, 2015; Riedesel *et al.*, 2018; Sawakuchi *et al.*, 2018). It is particularly applied in fluvial environments, since sediments are often heterogeneously bleached due to insufficient light exposure from sub-aqueous transport conditions (Cunningham *et al.*, 2015; Wallinga, 2002). The common thread of sediment process reconstruction tools is based on the concept that heterogenous and/ or homogeneous insufficient bleaching can be representative for sediment transport dynamics or for sediment dynamics prior to transport. A study on fluvial terraces and the underlying fluvial dynamics, showed that sediment tracing is successful in deriving past fluvial records and thereby local sediment dynamics (Bonnet *et al.*, 2019). Like the study of Bonnet *et al.* (2019), this study also focusses on retrieving extreme sediment dynamics.

Several luminescence proxies are developed in retrieving sediment dynamics from the incomplete bleached luminescence signals. First of all, the spread of equivalent dose distributions contain information on bleaching during the last burial cycle (Chamberlain & Wallinga, 2019). Moreover, the

percentage of grains contributing to age calculation from the total equivalent dose population, tells also something about the total spread and therefore the bleaching within the distribution. Secondly, an assessment of grains in saturation can indicate well or poorly bleached samples: a high percentage of grains in saturation represents unbleached or infinitely old (bedrock) grains (Bonnet *et al.*, 2019; Gong *et al.*, 2014). Thirdly, differences in doses between signals with different bleaching rates can give insight into the amount of bleaching, in its turn explaining sediment sources and transport routes (Chamberlain *et al.*, 2017; Reimann *et al.*, 2015). Preferably, signals for both quartz and feldspar are measurable within the particular environmental setting. Since, quartz signals are expected to be insensitive in the setting of this study, the use of this proxy is not convenient. Fourthly, luminescence sensitivity of quartz minerals, enable studying spatial dependency. The more sensitive the mineral is, the bigger the spatial distance it travelled, since natural cycling of the minerals tends to increase the minerals luminescence sensitivity (Pietsch, 2009; Sawakuchi *et al.*, 2018). However, in the course of the Pokhara deposits, a sensitivity analysis will not be conducted. Considering the short spatial transport distances (Preusser *et al.*, 2009) and the low natural sensitivity of the freshly eroded minerals in the Himalayan mountain range (Jaiswal *et al.*, 2009). Moreover only limited studies have been conducted on the spatial dependent sensitivity change of feldspar minerals. Preliminary results are indicating slight desensitization for IRSL and pIRIR signals over transport distance (Reimann *et al.*, 2019). Fifthly, age offset from an expected age can be used to understand dynamics of the sediment deposits; which is translated into the radiocarbon overestimation ratio within this thesis.

2.2.1. Bleaching

Spread in De-distribution

Spread in De distributions can be caused by experimental errors. Experimental errors are errors associated with measurements errors, parameter fitting errors and/ or measurement equipment errors. Overdispersion is a measure of the spread within a De distribution that cannot be explained by the individual uncertainties of the De estimates and is associated with incomplete bleaching or soil mixing. Spread due to incomplete zeroing of the luminescence signal, may produces skewed De distributions instead of normal distributions associated with well-bleached samples. The relatively big tail of the distribution represents the poorly bleached grains (Rhodes, 2011). In this study, Kernel Density distributions (KDE) are used to show the spread of the equivalent dose per aliquot (on single-grain level). Additionally, evaluation of the degree of bleaching is done by the use of the equivalent dose spread in radial plots. The heterogeneous bleached sample shows two De-populations, whilst for a well-bleached sample only one clear population is visible in the dataset (figure 6). In this particular example this is conducted by use of the residual dose based on quartz OSL, which should equal zero in case of complete bleaching (most right plot of figure 6). Notwithstanding, degree of bleaching can also be assessed on radial plots of equivalent doses representing the natural signal (Bonnet *et al.*, 2019; Chamberlain & Wallinga, 2019). Commonly the degree of bleaching for feldspar minerals is assessed on the pIRIR150 signal, since the relative contribution of anomalous fading is lower than for the IRSL signal. However, the IRSL signal is easier to bleach and could therefore be a good alternative in assessing poorly bleached samples (Bonnet *et al.*, 2019).

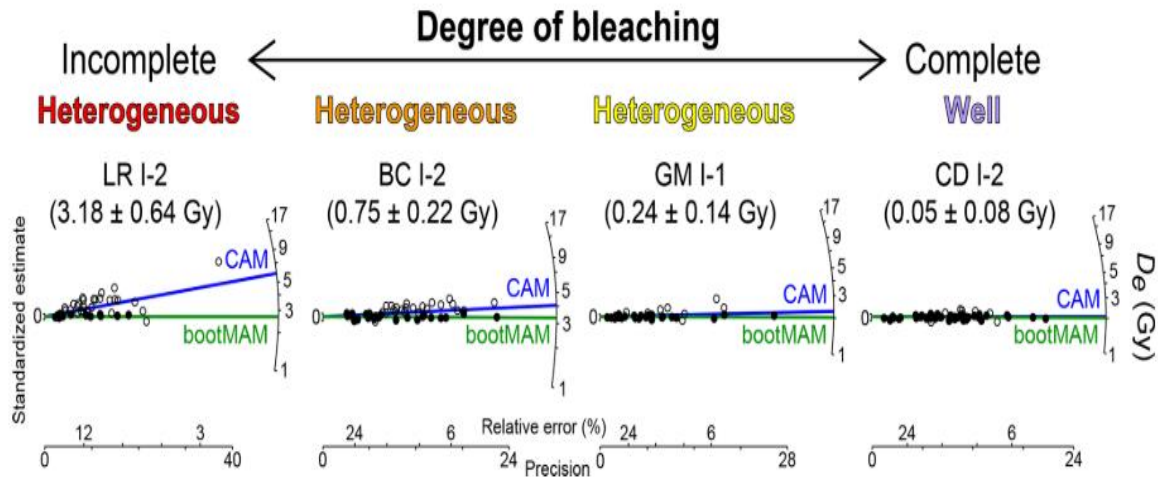


Figure 6: Assessing the degree of bleaching based on residual dose difference between the differences in equivalent dose (D_e) obtained by the bootstrapped Minimum Age Model (bootMAM) and the Central Age Model (CAM) and based on quartz OSL (Chamberlain et al., 2019). Ranging from incomplete (left) to complete (right) bleached aliquots.

Percentage of grains well-bleached in MAM-range

The Minimum Age Model (MAM) is a statistical model used to identify the equivalent doses of the best bleached grains within a poorly bleached sample and often applied in fluvial settings, since fluvial samples are often poorly bleached (Cunningham & Wallinga, 2012; Rhodes, 2011; Rodnight *et al.*, 2006). The MAM estimates the equivalent dose corresponding to the youngest subpopulation in the distribution (Galbraith *et al.*, 1999). A bootstrapped version of the MAM (bootMAM) measures the average statistical properties of a subsample, as the relation between a subsample and a sample is considered the same as the relation between a subpopulation and a sample (Cunningham & Wallinga, 2012). The percentage of grains used to calculate the bootMAM-equivalent dose, can be identified by scanning how much grains of the total population correspond with the bootMAM-equivalent dose value within 2σ of their uncertainty boundaries. It is expected that the outcome of this proxy can be translated into bleaching dynamics: the lower the percentage of grains used to identify the bootMAM- D_e , the higher the spread in the distribution.

2.2.2. Saturation

Reimann et al. (2017) proposed to use the percentage of saturated grains in the context of soil mixing as a proxy for soil reworking rates. Consecutively, Bonnet et al. (2019) used the percentage of grains in saturation as a proxy for the percentage of unbleached bedrock grains. To differentiate between grains above and below saturation, the $2 \cdot D_0$ criteria is applied (Ann G Wintle & Murray, 2006). This proxy represents the opposite of the percentage of grains within the MAM-range does: it assesses the grains which the other proxy does not assess.

2.2.3. Spatial analysis

The results of the luminescence proxies described in the previous paragraphs, can be translated into sediment dynamics when projected spatially. This proxy reveals spatial sediment dynamics dependency along the river course in the Pokhara valley.

3. Site description

3.1. General information

The study area is located in Nepal and restricted to the Pokhara Valley in Central Nepal (figure 2). The Seti Khola is the main river in the intermountain fluvial Pokhara valley and has its origin in the Sabche Cirque in the northern located Annapurna Massif which is part of the Himalayan mountain range (Schwanghart *et al.*, 2016). The Annapurna Himal embodies the Annapurna I (8091 m), Annapurna II (7937 m), Annapurna III (7555 m), Annapurna IV (7525 m), Gangapurna (7455 m), Dakshin (7219 m) and Machhapuchhre (6993 m) peaks. The city of Pokhara (28°13'N, 83°59'E, 870 m above sea-level) lies in the centre of the study area close to the lakes of Phewa, Rupa and Begnas, and at a horizontal distance of only 25 kilometres from the Machhapuchhre peak (Parsons *et al.*, 2016; Schwanghart *et al.*, 2016). This steep orographic gradient is one of the steepest topographical gradients in the world (Stolle *et al.*, 2017).

The number of population density in Pokhara city is increasing with a high rate: from 1991 to 2011 the population almost doubled to 446.764 inhabitants in 2011. Over the last decades the city has been exposed to multiple natural hazard risks, like sinkholes, floods, avalanches, earthquakes, land subsidence and glacial outburst floods (GLOF's) (Rimal *et al.*, 2015).

Nepal is known for its different climate types which are influenced in summer by monsoonal circulation and in winter by westerly circulation. This results in more precipitation in summer in the northeast and in the northwest during winter times. The mean temperature in Pokhara city varies between 16 till 20°C. The Pokhara valley forms the wettest region (5000 mm/yr) in Nepal because of the steep orographic gradient. The high orographic gradient functions as a barrier in the weather system and leads to rainfall band formation (figure 7) (Bookhagen & Burbank., 2010). According to Köppen-Geiger climate classification the Pokhara Valley is classified in the Cwa category: a temperate climate with dry winters and hot summers (Karki *et al.*, 2016).

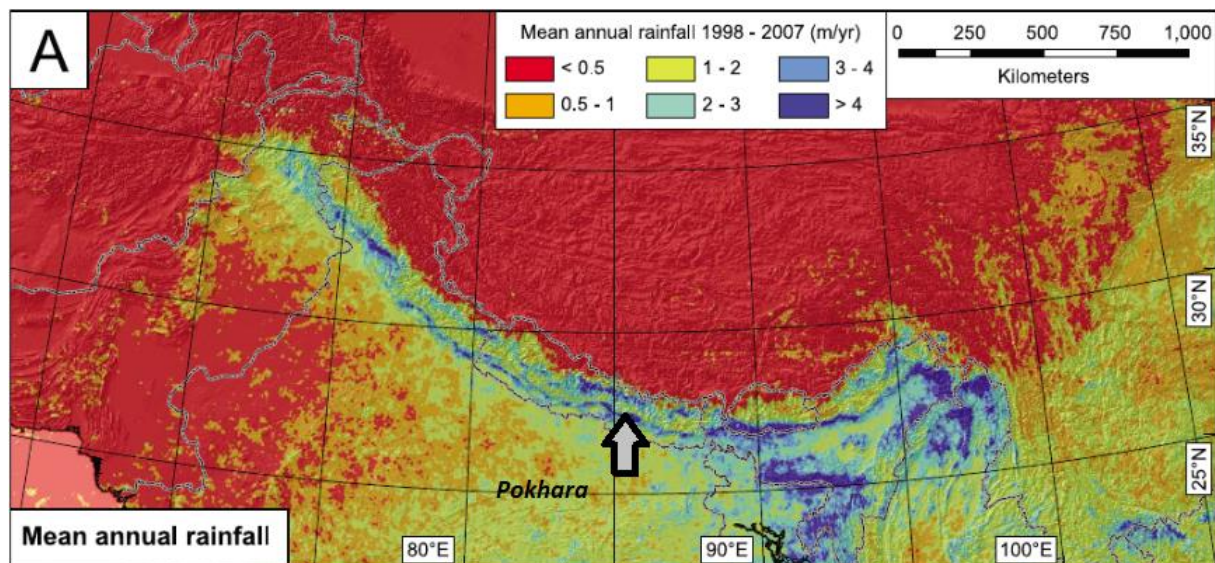


Figure 7: Mean annual rainfall distribution pattern for the Himalayas. Location of Pokhara city [Nepal] is indicated by the arrow (after Bookhagen & Burbank, 2010).

3.2. Geology of the Pokhara Valley

The Nepal Himalayas make part of an active collision zone; the Indian plate moves northward in direction of the Eurasian plate. As a consequence high uplift rates of ~5 mm/year occur in the higher Himalayas (Lavé & Avouac, 2001). The uplift velocity at the front of the Annapurna massif is 7 mm/yr (Grandin *et al.*, 2012). The geology of the (Annapurna-) Himalaya can roughly be divided into four main zones (figure 8) (Parsons *et al.*, 2016; Stolle *et al.*, 2017):

1. The Sub-Himalayan Zone (SHZ): non-metamorphosed sedimentary rocks of Miocene to Pleistocene origin deposited in the Himalayan foredeep system, like mudstones, siltstones, shales and conglomerates. The SHZ is located southwards of the study area.
2. The Lesser Himalayan Series (LHS): meta-sediments of Mid Proterozoic to Early Palaeozoic age from the Indian continent, like slates, sandstones, phyllites, quartzites and shales. On both sides the LHS is bounded by thrusting systems with NW-SE strike and NE dip: to the south by the Main Boundary Thrust (MBT) and to the north by the Main Central Thrust (MCT). The metamorphic grade increases towards the NE of the geological map (figure 8).
3. The Greater Himalayan Crystalline (GHC): metamorphic core of the Himalaya ranging from low metamorphic phyllites to high metamorphic gneisses of Early Palaeozoic age. In the south the GHC is bounded by the MCT and in the north by South Tibetan Detachment (STD) which comprises the hanging-wall of the shear zone. Important to note is that the Nilgiri limestones belong to the STD; they are present in the riverbed downstream.
4. The Tethyan Himalayan Sequence (THS): marine sedimentary rocks from the Cretaceous originating from the Tethyan sea on the Indian shelf continent. The THS consists of enormous amounts of limestones and calcareous sediments. The THS bounds the GHC in the south and the Tibetan plain in the north. The highest peaks in the region such as the Annapurna I consist of THS rocks.

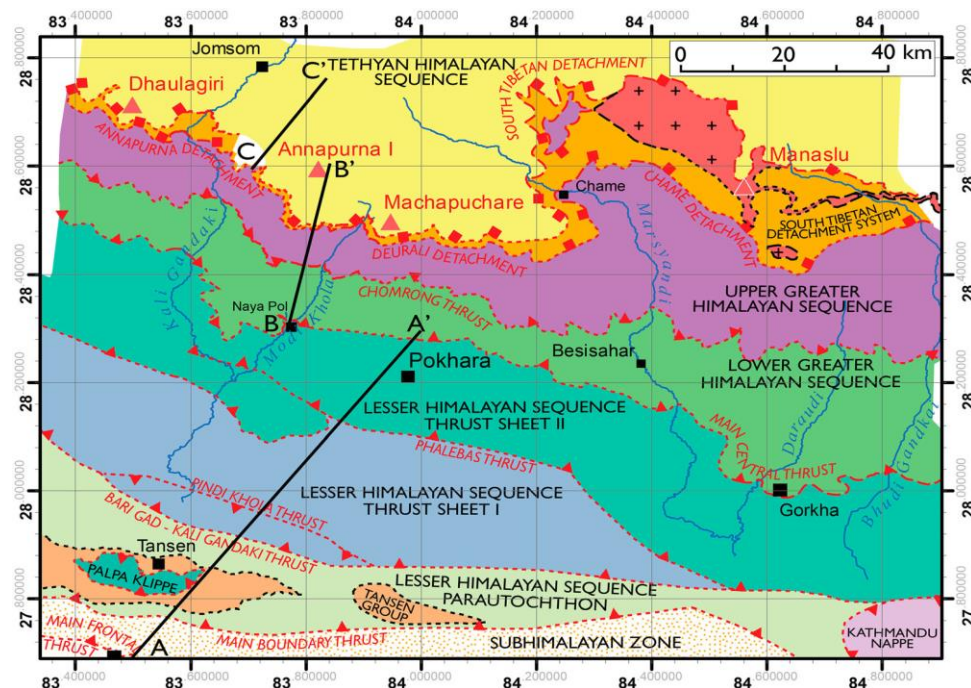


Figure 8: General tectono-geological map of the Pokhara region [Nepal]. Red dotted lines indicate faults and shear zones, whilst coloured polygons indicate geological units. Detailed cross-section profiles can be found in original reference (Parsons *et al.*, 2016).

3.3. Pokhara valley sedimentary infill

The steep orographic gradients results in a dynamic Pokhara Valley in terms of erosion, denudation and sedimentation (Lavé & Avouac, 2001). The valley has a width and length of approximately 20 and 70 kilometres, respectively. Remarkable is that the valley bottom is a more or less flat plain instead of a sharply incised gorge as can be found stream upwards. The plain is slightly inclined, thereby dipping to the south (Schwanghart *et al.*, 2016). The interest of this study is in the valley infill material, consisting of three distinct lithological formations: the Pokhara (Pk), Ghachok (Gh) and Tallakot (Tk) formation. Their origin is non-local and mainly from the GHC and THS, as proven by sediment provenance analysis studies (Schwanghart *et al.*, 2016; Stolle *et al.*, 2017). Moreover, sedimentological studies and radiocarbon dating implied that the debris flow deposits associated with the Pokhara formation are due to a high-magnitude low-frequency event linked to Medieval earthquake activity (Schwanghart *et al.*, 2016; Stolle *et al.*, 2017).

The implication that earthquake activity caused the presence of debris flow deposits in the Pokhara valley, can be underlined by the tectonic setting and regional climate of the region:

1. Climate as a conditional factor: the steep orographic gradient causes on average higher precipitation rates (Karki *et al.*, 2016). A wet period with high water availability could more easily lead to landslide development, since increased subsurface fluid pressure decreases the frictional force (Roback *et al.*, 2018).
2. Tectonics as a conditional factor: transect B (figure 8) (Parsons *et al.*, 2016) gives insight into the local tectonic setting. The northern faulting system (STD) in the transect is a detachment faulting system (several normal faults combined). Bedding structures on the transect indicate that the angle of this faulting system is 55 degrees to the south. In other words: the rock layers are positioned more or less parallel to the slope. Because of this detachment faulting system, the THS rock formation is moving downwards. Whilst the GHC is moving upwards. In the south bounded by the MCT, this faulting system causes the upward movement. In the southern overthrust system of transect B there is extension, because the compression rates in the north are higher. The whole geological structure contains weak zones and is therefore prone to landslides and other mass movement events, especially since the rock layers are in line with the slope angles in the current geomorphology.
3. Furthermore, it is very likely that earthquake activity could have been acting as a triggering factor. Analysis of past earthquake activity in the Annapurna region showed that earthquakes with high magnitudes on Richter's scale have been occurring in the study area (Rajaure & Paudel, 2018, Bollinger *et al.*, 2014).

In several studies the Pokhara formation was dated by using radiocarbon dating on trees and charcoal, comparable age ranges are obtained (Fort, 1986; Fort, 1987; Yamanaka, 1982). Whereas one radiocarbon date showed that the Ghachok formation could be deposited about 10.000 years BP (Koirala *et al.*, 1997). As to my best knowledge there are no more burial ages of the Pokhara, Ghachok and Tallakot formation available in scientific literature.

Since deposition in Medieval times, the Seti Khola and its river stream network incised rapidly into the deposits up to ~ 100 metres locally. This rapid incision is enhanced by high regional uplift rates of 7 mm/yr (Grandin *et al.*, 2012). Those sediment bodies are nowadays present as river terrace levels on the course of the river Seti Khola and its tributaries (figure 9A). It is deduced that the formations are of different age, since they have distinct lithologies, terrace level heights and spatial occurrence, which can be described as following (Stolle *et al.*, 2017):

1. Pokhara formation: is the most extensive unit in the study area which extends up to 7.5 kilometres into tributaries thereby blocking small channels and covering older LHS hillslopes. Clast-supported conglomerates alternate with matrix-supported conglomerates and sand and silt layers (figure 9B & 9C). The very fine light grey silt layers are interpreted as slackwater deposits (Schwanghart *et al.*, 2016), which can settle from high-density tidal sediment flows (Carling, 2013). Slack water is the moment in time before a tidal stream reverses in opposite direction.
2. Ghachok formation: located from the fan source at Mirsa southwards up to the city of Pokhara a few tenth of meters above the Pokhara formation and below the Tallakot formation. The formation consists of conglomerates in a light brown silty matrix high in chalk (Yamanaka, 1982), the chalk contribution is probably derived from the presence of the Nilgiri limestones and THS limestones stream upwards (figure 9D). The Ghachok formation has a steeper surface gradient than the Pokhara formation. The concreted calcareous sediments can support sinkholes and caves southwards of the city of Pokhara (Gautam *et al.*, 2000).
3. Tallakot formation: present in the northern part of the study area as the highest elevated terraces and probably buried by Ghachok and Pokhara formations more downstream into the valley. The lithology of the Tallakot resembles the Ghachok lithology. However, the unit is more cemented and contains bigger conglomerates up to boulder-sizes (Yamanaka, 1982).



Figure 9: Field images from the Pokhara valley. A. River terraces along the Seti Khola with in the background the Annapurna Massif and the Machhapuchhre peak (fishtail mountain). The lower terrace used for rice agriculture concerns the Pokhara formation; the higher tree vegetated terrace is of Ghachok origin. B. Road outcrop of the Pokhara formation: several course layers intertwined by sand and finer silt layers. C1. & C2. Zoom-in of outcrop B: detail picture of the sand layering within the outcrop. D. Road outcrop of the Ghachok formation in the upstream area of the Seti Khola.

4. Methods

4.1. Sampling

All samples are taken during a fieldwork trip in October 2019 in the Pokhara valley [Nepal] (figure 10), beforehand a sampling strategy was developed. The strategy addresses three main objectives: recording the spatial variation from source to sink, ascertaining minimal distances between luminescence and radiocarbon sampling locations and being able to derive local geochronology of the gravels. In total 16 samples have been collected during the October 2019 fieldwork and two samples were added additionally from a previous fieldwork by Amelie Stolle (Table 1). More samples were collected than could be analysed in the purpose of this master thesis. The decisions made, in establishing a priority list for laboratory analysis, are based on the topographical setting and the Digital Elevation Model (DEM) of the area, thereby acknowledging the research questions.

Samples are taken by the use of metal tubes and secured by plastic lids and tape. The Ghachok formation was so concreted that it was impossible to take tube samples; therefore it is decided to collect the samples in the form of lumps (all samples of which the field sample numbers start with Gh). Additionally, sediment directly circumcising the sample location was taken as an extra in case the dose rate material from the tube would not be sufficient. In retrieving samples in the field, the OSL guideline of the Utah State University was followed (Nelson *et al.*, 2019). This guideline describes how to retrieve the OSL samples in such a way that light contamination is minimal. For every sample taken a sedimentological log (visual representation of sedimentological obtained field data) is created. In total 9 sedimentary logs are created with the program Sedlog of the Royal Holloway University London (Zervas *et al.*, 2009). Besides each log a photograph of the outcrop is added and sediment facies are indicated (Appendix IV).

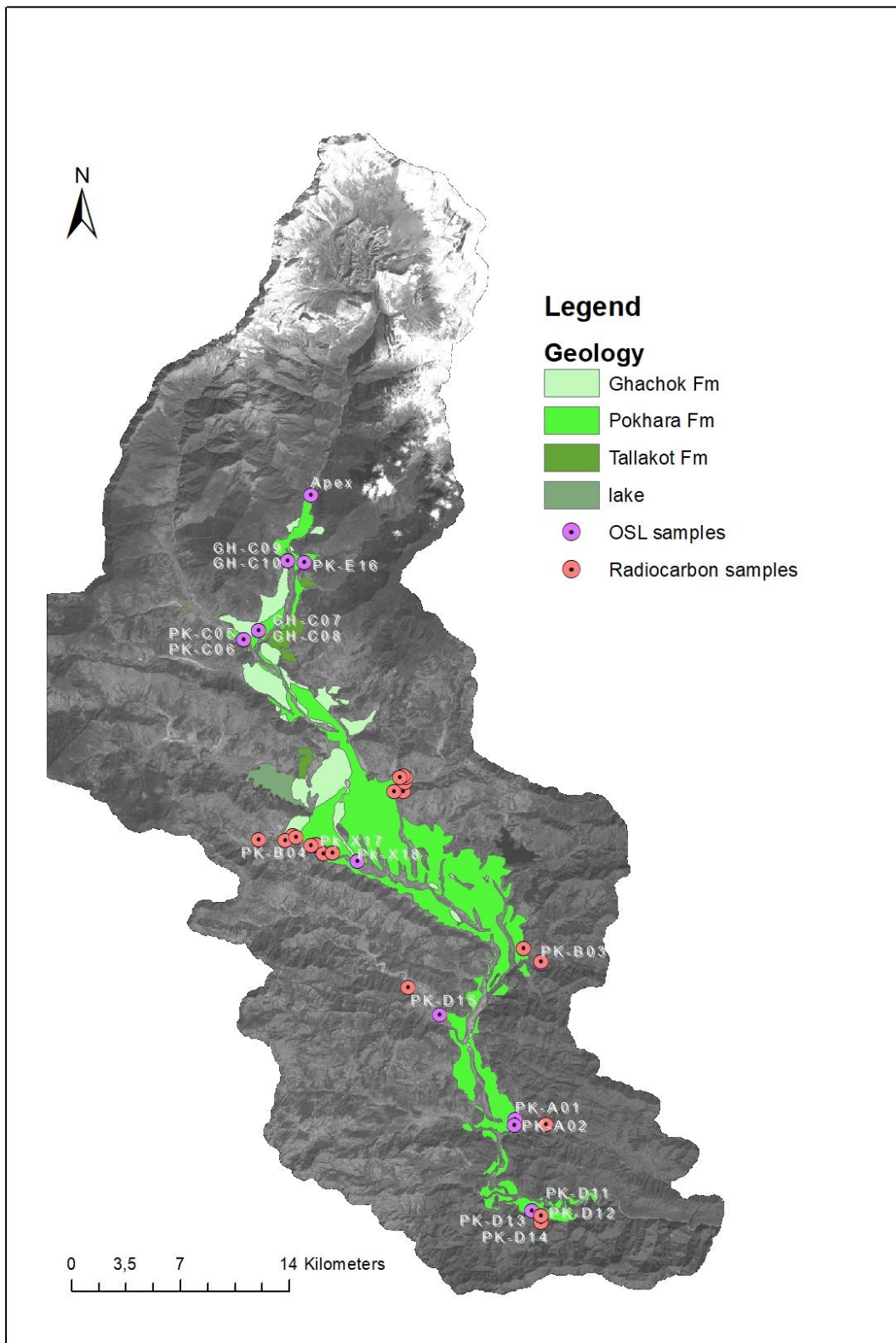


Figure 10: Map of the study area, created by the use of satellite imagery. The radiocarbon and OSL sample locations (inclusive name reference) are indicated by points. Polygons show the geological borders of the Pokhara, Ghachok and Tallakot formation.

Table 1: Field and NCL laboratory sample numbers with corresponding coordinates, as well as the distance to the apex of the debris fan . *samples analysed in this thesis **samples collected by Amelie Stolle during previous field visit. Sampling depth was unknown for samples collected by Stolle, for that reason an arbitrary value of 1 meter is applied.

Field sample numbers	NCL-numbers	Latitude	Longitude	Distance to apex [m]	Elevation [m]	Sampling depth [m]
Fan apex	-	28.3827	83.9735	0	-	
Pk-A01	NCL-7619108	28.018	84.097	63987	469	30
Pk-A02*	NCL-7619109	28.015	84.096	64068	448	1.5
Pk-B03*	NCL-7619110	28.108	84.116	49266	576	3
Pk-B04*	NCL-7619111	28.176	83.975	40371	723	5.5
Pk-C05*	NCL-7619112	28.3	83.927	13641	1053	25
Pk-C06	NCL-7619113	28.3	83.927	13641	1053	25
Gh-C07*	NCL-7619114	28.305	83.937	12532	1144	17
Gh-C08	NCL-7619115	28.305	83.937	12532	1144	17
Gh-C09	NCL-7619116	28.345	83.957	6357	1341	2
Gh-C10*	NCL-7619117	28.345	83.957	6357	1341	2
Pk-D11	NCL-7619118	27.965	84.106	72575	428	9
Pk-D12	NCL-7619119	27.961	84.112	73835	430	5
Pk-D13*	NCL-7619120	27.962	84.112	73699	409	5.3
Pk-D14*	NCL-7619121	27.962	84.112	73699	409	5.3
Pk-D15*	NCL-7619122	28.08	84.049	55252	549	1
Pk-E16*	NCL-7619123	28.344	83.968	6318	1231	0.5
Pk-X17*/**	NCL-7619124	28.18	83.97	41296	714	1
Pk-X18*/**	NCL-7619125	28.17	83.998	37508	695	1

4.2. Experimental details

Sample preparation

All the OSL samples are analysed at the Netherlands Centre for Luminescence Dating (NCL) at Wageningen University & Research (WUR). Two additional radiocarbon samples are sent to the Poznan radiocarbon laboratory in Poland. The sample preparation of OSL samples is conducted by the guidelines of the NCL laboratory under dimmed red light conditions. Samples are opened and the outer three centimetres of both outer edges is removed and used for environmental dose rate (Dr) measurements. The inner sediment is used for the estimation of paleodoses, through the measurement of single-grain equivalent doses (De), at least 100 grams of sediment is required. The lump samples were treated very carefully, in the best possible way it is tried to retrieve only inner material from the lump to prevent contamination.

De -samples are sieved with the use of a waterflow sieving machine. Sieve sizes used are: 250, 212 and 180 μm . Material with a grain size of 212-250 μm is used for further analysis. A 10% HCl solution is added to the 212-250 μm fraction in order to remove chalk components with 40 minutes of treatment time, afterwards rinsed with demi-water. Consecutively, a 10% H_2O_2 solution is added in order to remove organic matter (OM). This is an endothermic reaction and treatment time is around 30 minutes, afterwards rinsed with demi-water. Magnetic separation can be used to remove magnetic grains from the sample, since quartz and feldspar grains both do not have magnetic properties. Due to maintenance on the magnetic separation machine, the samples analysed in this thesis are not magnetically separated. Next is the heavy density separation of quartz and feldspar grains, target is to obtain K-feldspars with a density ranging between 2.50 and 2.56 g/cm^3 . First quartz minerals are removed by adding a liquid with a density of 2.63 g/cm^3 . Afterwards the K-feldspars are isolated from the Na-feldspars by adding a liquid with a density of 2.58 g/cm^3 , the K-feldspars sink in the substance and are collected. Quartz grains are etched by a 10% HF solution to remove potential feldspar contamination, thereby also slightly etching their outer parts. Rinsing with demi-water removes the contamination after the HF treatment. Once sample treatment is finished, single-grain discs are prepared for all De and other measurements within this project. Only the fading test is conducted on multiple grain discs.

The Dr -samples are processed into a puck: sediment is dried overnight at 105°C to be able to calculate the soil moisture content (Loss On Ignition (LOI)) (Heiri *et al.*, 2001), sediment is ashed overnight at 550°C to be able to calculate organic matter (OM) content and grinded to obtain a homogeneous sample with particles smaller than 300 μm . Afterwards, pucks are formed by adding melted wax.

Measuring the dose rate (Dr)

The total dose rate is dependent on several internal and external components. The obtained soil moisture and organic matter content contribute to the external dose rate calculation. Gamma spectrometry is applied on the pucks in order to determine the contribution to: the external dose rate by isotope activity from the Uranium and Thorium decay chains, the internal dose rate by ^{40}K activity and the internal and external dose rate by ^{87}Rb activity (R. K. Smedley, 2014). Furthermore, the contribution of cosmic radiation to the dose rate is determined following a protocol (Prescott & Hutton, 1994).

Measuring the equivalent dose (D_e)

All measurements were performed on an automated Risø TL/OSL reader (DA 15). The samples were irradiated by a $^{90}\text{Sr}/^{90}\text{Y}$ beta-source with a dose rate of 0.098 Gy/s for all single-grain measurements and with a dose rate of 0.114 Gy/s for all multi-grain measurements. All feldspar grains were detected by a I-410 filter to capture the K-feldspar rich emission at 410 nm for the IRSL (at 50 °C) and pIRIR (at 150 °C) signal. All quartz grains were detected by a U-340 filter for green light OSL.

In total five types of measurement sequences are applied within this study in the following order: multiple-grain quartz IR test – single-grain feldspar dose recovery test - single-grain feldspar equivalent dose – single-grain quartz equivalent dose – multiple-grain feldspar fading test. The single-grain feldspar and quartz equivalent dose sequences, as well as the feldspar fading sequence, can be found in table 2 and table 3, respectively. For the dose recovery measurement, sample NCL-7619125 was bleached in a solar simulator for 46 hours, thereby receiving daylight five times stronger than natural daylight. The fading test sequence was time-wise optimised. All sequences – except the ones presented here – can be found in Appendix I.

Table 2: Measurement protocol of single-grain quartz equivalent dose measurements. This protocol is applied to two samples: NCL-7619111 and -123.

Single-grain quartz equivalent dose protocol		
Step	Treatment	Measurement
1	Natural or regenerative dose	
2	Preheat at 220 °C for 10 s	
3	IR LED at 30 °C for 40 s	
4	SG green light OSL at 125 °C for 1 s	Lx
5	Test dose: 5 Gy	
6	Preheat at 200 °C for 10 s	
7	SG green light OSL at 125 °C for 1 s	Tx
8	Hot-bleach at 210 °C for 40 s	
	Repeat steps 1 till 8 for irradiation [Gy]: Natural – 5 – 10 – 20 – 50 – 100 – 200 – 0 – 5 – 5	

Table 3: Measurement protocol of single-grain feldspar equivalent dose measurements. This protocol is applied to ten samples: NCL-7619109, -110, -111, -112, 120, -121, -122, -123, -124 and -125 (all Pokhara formation). Two samples of the older – expected – Ghachok formation are also measured with the same protocol, however the irradiation doses are set higher (in Gy): Natural – 10 – 20 – 40 – 80 – 160 – 240 – 360 – 0 – 10.

Single-grain feldspar equivalent dose protocol		
Step	Treatment	Measurement
1	Natural or regenerative dose	
2	Preheat at 175 °C for 120 s	
3	SG infrared stimulation at 50 °C for 2 s	Lx – IRSL50
4	SG infrared stimulation at 150 °C for 2 s	Lx – pIRIR150
5	Test dose: 10 Gy	
6	Preheat at 175 °C for 120 s	
7	SG infrared stimulation at 50 °C for 2 s	Tx – IRSL50
8	SG infrared stimulation at 150 °C for 2 s	Tx – pIRIR150
9	IR wash at 150 °C for 500 s	
	Repeat steps 1 till 8 for irradiation [Gy]: Natural – 10 – 20 – 40 – 80 – 160 – 240 – 0 – 10	

4.3. Data analysis

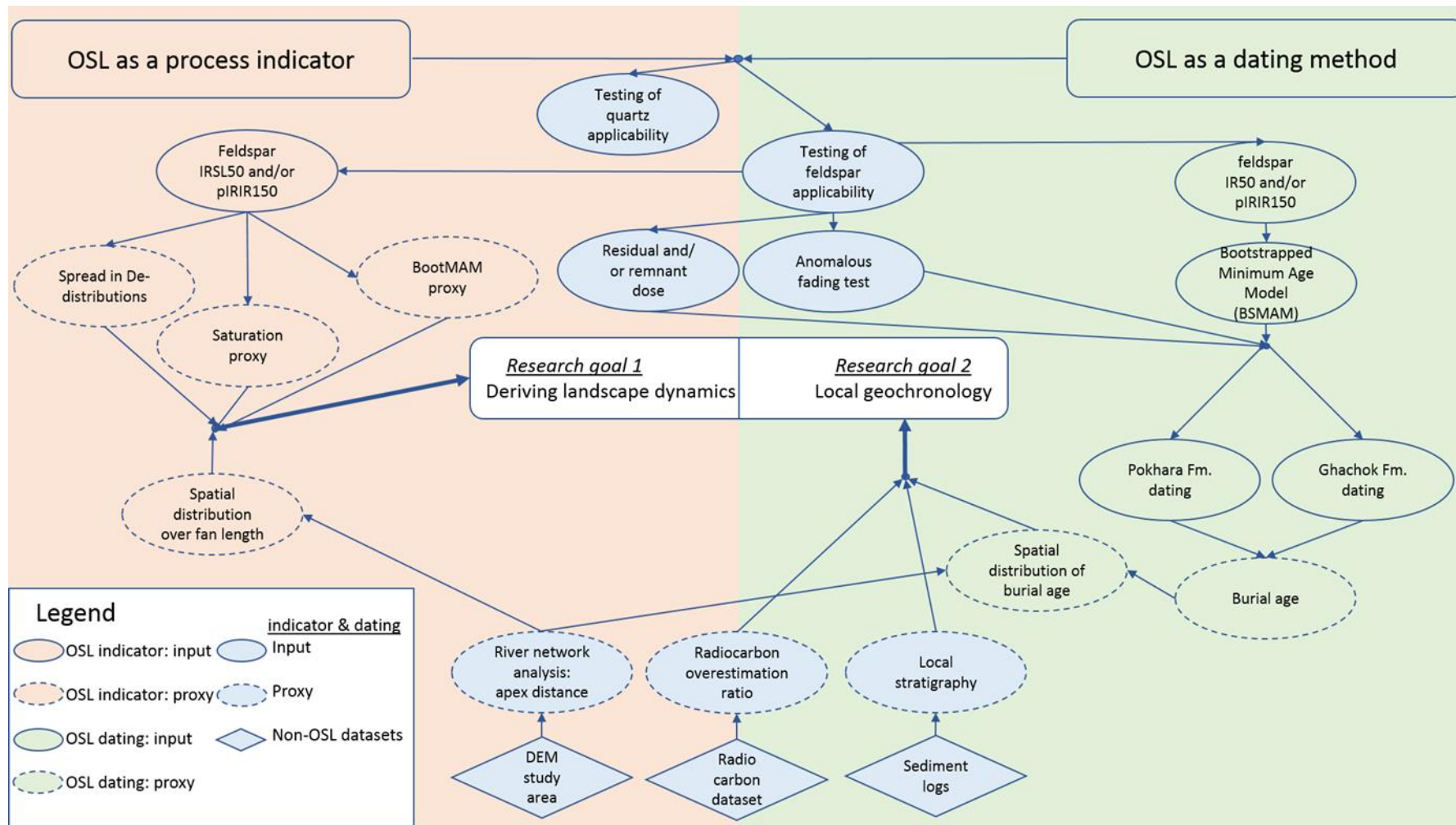


Figure 11: Data analysis work flow scheme. The left side (in orange) marks the work flow adapted to reach research goal 1: deriving landscape dynamics, whilst the right side (in green) marks the work flow adapted to research goal 2: local geochronology. Balloons in blue indicate processes which apply for both research goals. The oval balloon is input into the work flow, the dotted oval balloon indicates a proxy and the diamond shaped balloon indicates additional non-OSL datasets. How the factors shown in this diagram are assessed within this thesis, is explained in the subsequent text sections. Data interpretation is only conducted on feldspar data, since quartz showed to be non-applicable in this setting.

4.3.1. Dating

Acceptance criteria - Risø Analyst Software

All measurements were analysed by the use of Risø Analyst Software – version 4.31.9 (G. Duller, 2015), thereby applying the same acceptance criteria for all test types and samples. For feldspar measurements the signal integration limits were set between channel 6 and 8 and for the background signal between channels 45 and 55. Resulting in measuring the signal between 0.18 and 0.21 s and measuring the background signal between 1.35 s and 1.65 s. For quartz measurements the signal integration limits were set between channel 6 and 8 and for the background signal between channels 15 and 20. Resulting in measuring the signal between 0.18 and 0.21 s and measuring the background signal between 0.45 s and 0.60 s. Every dose response curve was fitted exponentially, forced through the origin and errors were incorporated when fitting. Additionally, 100 Monte Carlo repeats were calculated in curve fitting. Acceptance criteria are all set at a maximum of 20%: this is valid for the recycling ratio limit, the maximum test dose error and the maximum recuperation. The recycling ratio assesses whether the sensitivity changes following the first SAR cycle can be correctly monitored by the SAR protocol. The maximum test dose error assesses if a sufficiently bright luminescence signal is emitted by the grains. The recuperation assessment focusses on the sensitivity-corrected zero dose signal. After exposure the obtained signal should equal zero, however often residual doses remain within the signal.

Once the data was analysed in Risø Analyst it was exported to an excel file; which serves as the input data format for the further data analysis conducted within the R software environment by the use of the Luminescence package (Dietze *et al.*, 2013; Kreutzer *et al.*, 2012).

SAR assessment: dose recovery ratio

The analysed residual and dose recovery doses are imported into the R environment and assessed by the use of the Central Age Model (CAM) (Kreutzer *et al.*, 2012). The residual dose CAM-value is subtracted from the dose recovery CAM-value and subsequently divided by 15 Gray (the given known dose) to obtain the dose recovery ratio. The residual dose assesses the hard to bleach inherited signal (R. Kars *et al.*, 2014). Whereas the dose recovery assesses if a given known laboratory dose can be measured 1:1 as paleodose.

Bootstrapped Minimum Age Model (MAM)

To assess the paleodose based on the De-distributions, the Minimum Age Model (MAM) is applied. This model assesses the youngest subpopulation of the total population, the choice to use this model is justified because of the expected dynamic nature of the depositional process. And thus samples are expected to be very poorly bleached and only the youngest subpopulation (well-bleached grains) can indicate the “true burial age”. The bootstrap function is applied: subsets are taken and average statistical properties are determined for those subsets. A sigma-b value of 0.3 was applied based on sigma-b values used in comparative literature (Brill *et al.*, 2018; R. K. Smedley, 2014). It is important to use a best guess of the sigma-b value, if the value is too high the MAM De value will be overestimated and if the value is set too low the MAM De value will be underestimated (R. K. Smedley, 2014). The results of the MAM application are shown by the use of radial and KDE (Kernel density) plots using the functions *plot_RadialPlot* and *plot_KDE* (Dietze, 2012; Kreutzer *et al.*, 2012).

Anomalous fading rates and corrections

The average fading rate was obtained within the Risø Analyst Software for both feldspar signals (IRSL50 and pIRIR150), thereby averaging the rate per sample. Within R this rate is used to correct the burial ages for fading by the use of the *calc_FadingCorr* function, which requires the following input parameters: the uncorrected burial ages (with their corresponding errors in Gy), the fading rates (with their errors in %/decade), the tc value (in seconds), the tc.g_value (in seconds) and the amount of Monte Carlo repeats (100). The burial ages are calculated by dividing the obtained bootMAM-De by the calculated dose rates. The tc_value represents the time between the moment of irradiation and the prompt measurement, which is 255 seconds. The tc.g_value also represents the time between the moment of irradiation and the prompt measurement but applied for the fading rate calculation and is set to the standard value of two days (172800 seconds).

Radiocarbon overestimation ratio

The calibrated radiocarbon dataset (Schwanghart *et al.*, 2016), is used to obtain the best guess radiocarbon age of the Pokhara formation. The calibrated ages (and their corresponding errors) are averaged and this value is assumed to represent the best guessed radiocarbon age. Since radiocarbon ages are presented in years BP (Before Present = 1950 CE), the value is calculated in unity with luminescence data representation in ka (kilo annum = 2019 CE) and corrected for the 69 years indifference. This value is set as the ratio of 1, luminescence ages are compared to this value in order to retrieve an overestimation ratio compared to the “true burial age” as shown by the radiocarbon data.

4.3.2. Reconstructing sediment dynamics

Saturation proxy

To distinguish between grains above and below the luminescence signal saturation, the $2 \cdot D_0$ criteria is applied as previously done by (Bonnet *et al.*, 2019). This criterion makes sure that grains which fall within the flat part of the dose recovery curve, where \ln/T_n is above 85% full saturation, are indicated as grains in saturation. The saturation proxy is then calculated by evaluating the percentage of grains of the total population that are in saturation. In other words, this proxy assesses the non-beached and/ or inventively old grains, like bedrock grains without an exposure history.

BootMAM proxy

This proxy evaluates the opposite grains as are evaluated by the saturation proxy: it assesses the grains which are used to calculate the bootMAM De-values. The function *plot_RadialPlot* shows these grains in a bar around the calculated De-value. Grains that fall within this bar are the grains of which their value including error bar margins of 2-sigma, overlaps with the calculated bootMAM De-value. The bootMAM proxy is then calculated by evaluating the percentage of grains of the total population that fall within this bar. In other words, this proxy assesses the amount of “relatively” well-bleached grains.

River network analysis

In ArcMAP the river network is extracted by the use of several tools from the Hydrology toolbox. In R the riverdist package is used to calculate the distances between the sample locations and the apex fan along the course of the river network with the *riverDistance* function. In this way it is made sure that transport distances are assessed along the river course.

5. Results

5.1. Sedlogs and river network analysis

In appendix IV the sedimentary logs of each sample location are presented. Each log is supplemented with a picture of the sedimentary unit. The visual analysis of the pictures, augmented by field observations and textural interpretations of the sediments, shows that in general the grain size of the material declines downstream. As well for the sediment matrix and for the loose boulders within this matrix.

The river network analysis main result is the calculation of the distance between sample location and the fan apex at the small town of Mirsa. Figure 12 shows the river network assessed for those calculations with the sample locations indicated. In appendix V, a histogram of the so-called snapping distance between sample location and its corresponding river point along the river network is shown. This snapping distance is calculated in order to establish a distance calculation along the river network instead of horizontal distance. The histogram shows that most sample locations are located 500 up to 1000 meters from the main river stream (Seti Khola).

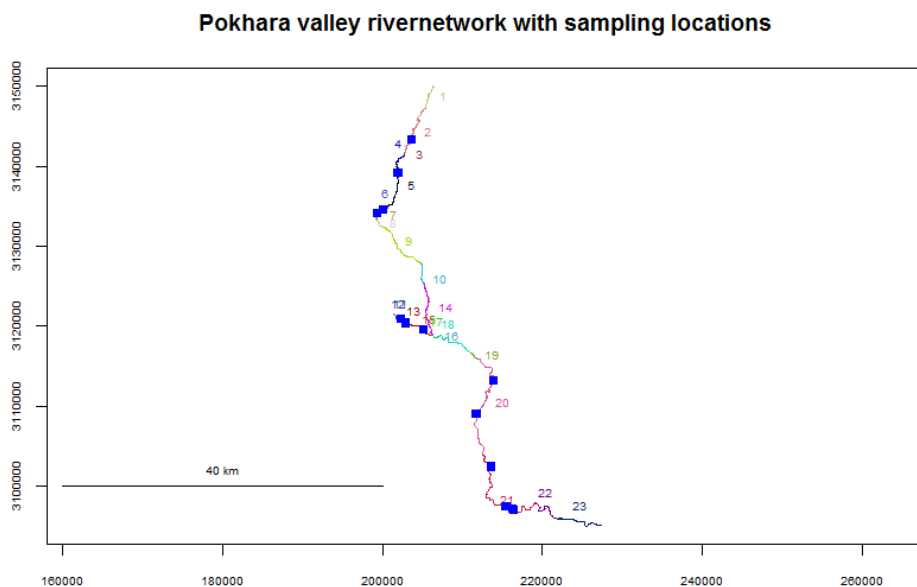


Figure 12: River network pattern of the Seti Khola catchment within the Pokhara valley. The blue squares are depicting the luminescence sample locations visited in the field in October 2019.

5.2. Dating

5.2.1. Dose recovery ratio

Table 4 shows the number of grains and paleodoses [Gy] of the residual and dose recovery doses obtained by the application of the CAM for the IRSL50 and pIRIR150 signal. The residual dose and the dose recovery CAM-De values are lower for the IRSL50 signal than for the pIRIR150 signal. Remarkably, is that the dose recovery ratio for the IRSL50 signal of 0.88 ± 0.01 , lies below the common acceptance range (0.90 – 1.10) (Rhodes, 2011; Ann G Wintle & Murray, 2006). This implies that obtained laboratory measurements are not directly representing the true natural doses. The dose recovery ratio for the pIRIR150 signal of 0.95 ± 0.01 , is well within the range of acceptance.

Table 4: Number of grains, paleodoses and dose recovery ratios for the IRSL50 and pIRIR150 signal. The given dose is 15 Gray.

IRSL50 signal CAM-De [Gy]	Residual dose 0.43 ± 0.06 (n=29)	Dose recovery 13.69 ± 0.20 (n=68)	pIRIR150 signal CAM-De [Gy]	Residual dose 1.18 ± 0.15 (n=12)	Dose recovery 15.40 ± 0.30 (n=51)
Dose recovery ratio	<i>0.88 ± 0.01 (IRSL50)</i>		Dose recovery ratio	<i>0.95 ± 0.01 (pIRIR150)</i>	

5.2.2. De-distributions

Pokhara formation

The single-grain Quartz De-measurements on samples of the Pokhara formation resulted in less than 1% luminescence signal sensitivity (table 5). In total an estimated amount of 540 grains were assessed and only two grains provide a sufficiently bright OSL signal, furthermore 13 grains provide OSL signals which are clearly feldspar contaminated, as visible from their shine-down curves and the rejection criteria. A sample reproducibility study showed that a minimum of 50 De-values is needed to obtain a good paleodose estimation (Rodnight *et al.*, 2006). This entails that a minimum of 150 discs (6 discs * (50/2)) are needed to establish a robust paleodose in the case of single-grain Quartz dating of the Pokhara formation.

Table 5: Properties of luminescence sensitivity of the single-grain Quartz measurements on the Pokhara formation.

# of total Qz-grains	# of luminescence grains	# of feldspar contaminated grains	% luminescence
540*	2	13	< 1%
*540 grains is based on an average of 90 grains per discs times the number of discs (6)			

In contrast, a sensitive luminescence signal is retrieved by assessing feldspar grains of the Pokhara formation. For that reason, all further De-measurements are only conducted on the feldspar minerals. The De-distributions of the obtained datasets are introduced by the use of radial and KDE plots for the IRSL50 and the pIRIR150 signals separately (Appendix II and III).

Two radial plot examples are shown in figure 13: a radial plot shows how all measured De-values [Gy] are distributed (log-scale z-axis) and subsequently show their relative standard error [%] and precision (x-axis). The subtitles of the figure indicates the amount of De-values displayed in the distribution (n), the percentage of De-values within 2-sigma from the paleodose and the amount of saturated grains (n.sat) which are not shown in the distribution. From figure 13 it is directly clear that the De-values are distributed over a large range, ranging from a few Gray to even over 500 Gray for the pIRIR150 signal. The huge spread in both De-distributions indicate that sample NCL-7619125 is very poorly bleached. Although, application of the bootMAM on those De-distributions show that there are still some well-bleached grains retrievable with lower De-values. For both signals approximately the same number of grains is used to calculate this paleodose, as is shown by parameter n. However, the amount of grains in saturation (n.sat) is much higher for the IRSL50 signal than for the pIRIR150 signal, which is true for all samples. As stated all other radial plots are presented in appendix II. An overall trend is clear: all samples are very poorly bleached, however some De-distributions may offer potential to extract lower paleodoses by using the bootMAM model. Another important result from assessment of all radial plots is that the De-distributions, and therefore the paleodoses of the IRSL50 signal systematically contains lower values. This implies that the IRSL50 paleodose can be expected younger.

Two Kernel Density Estimation plots are shown in figure 14: a KDE plot shows the distribution of the De-values [Gy] along with a fitted probability density function. The form of this function tells something about the spread of the data: the narrower the density graph, the more the estimated De-values are concentrated around the same value. The number of grains presented in the KDE plot is presented by parameter n and the number of saturated grains by n.sat. The paleodose value determined by the bootMAM is shown in the subtitle. In figure 14 only the KDE plots for sample NCL-7619125 (both signals) are shown, the rest can be found in appendix III. The KDE plots show that in general the density graphs cover a wide distribution; another sign that the samples are very poorly bleached. In general the KDE plots of the IRSL50 signals are narrower than the pIRIR150 signal distributions. In other words, the IRSL50 KDE plots contain a slightly more clearly visible leading edge population on the younger end of the distribution. However, this observation is strongly dependent on the number of grains assessed within the KDE plot.

Figure 13: Radial plots showing the D_e -distributions for the IRSL50 and pIRIR150 signals of sample NCL-7619125. The paleodose interpretation is conducted by bootMAM application ($\sigma = 0.3$) and shown by the green line. The amount of grains within the distribution is shown by parameter n .

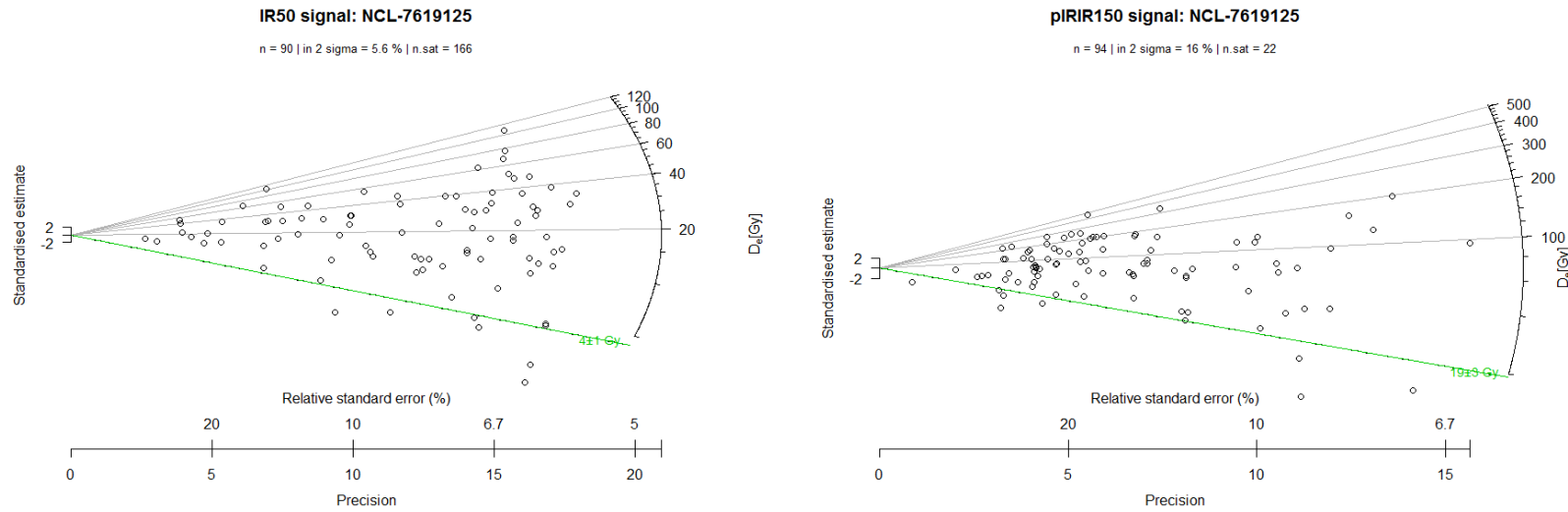
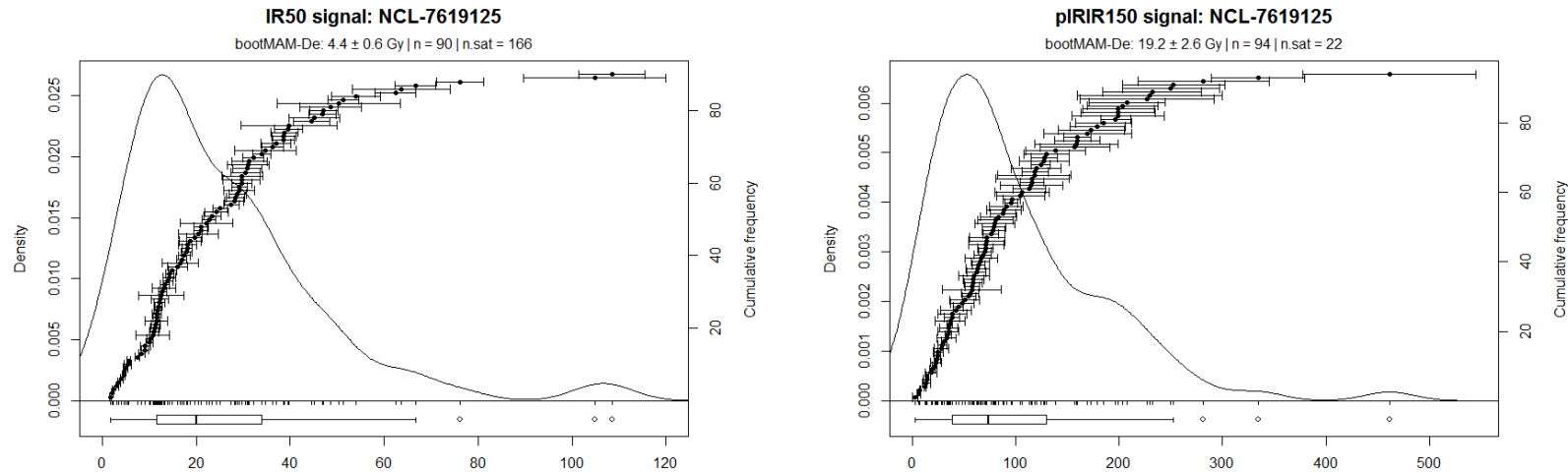


Figure 14: Kernel Density Estimation (KDE) plots showing the D_e -distributions for the IRSL50 and pIRIR150 signals of sample NCL-7619125. The paleodose interpretation is conducted by bootMAM application ($\sigma = 0.3$) and noted in the subtitle of the plot. The amount of grains within the distribution is shown by parameter n .



The paleodoses [Gy], as shown in figure 13 and 14 in the sub captions, are plotted over the length of the fan apex in the Pokhara valley to get insight into spatial variability. In studying the spatial distribution of the luminescence data, it is chosen to plot the paleodoses instead of the fading corrected burial ages, since it is assumed that fading is more or less similar for all samples. In figure 15 the paleodoses are plotted for the IRSL50 signal. It seems that there are two populations present within the dataset, in figure 15 they are separated and called population1 and population2. The application of a linear regression model to both populations, result in a R^2 of 0.29 for population1 and in a R^2 of 0.34 for population2. The R^2 assess how well the data fits the regression model, also called the goodness of fit. In other words, it determines the variability in the dependent variable (paleodose) that can be explained by the independent variable (distance to apex). The paleodose variability of the IRSL50 signal, can partly be explained by its spatial occurrence according to the R^2 values. The paleodoses of population1 follow a slight decreasing trend with increasing distance to the apex, whilst the doses of poulation2 show a more or less constant spatial trend.

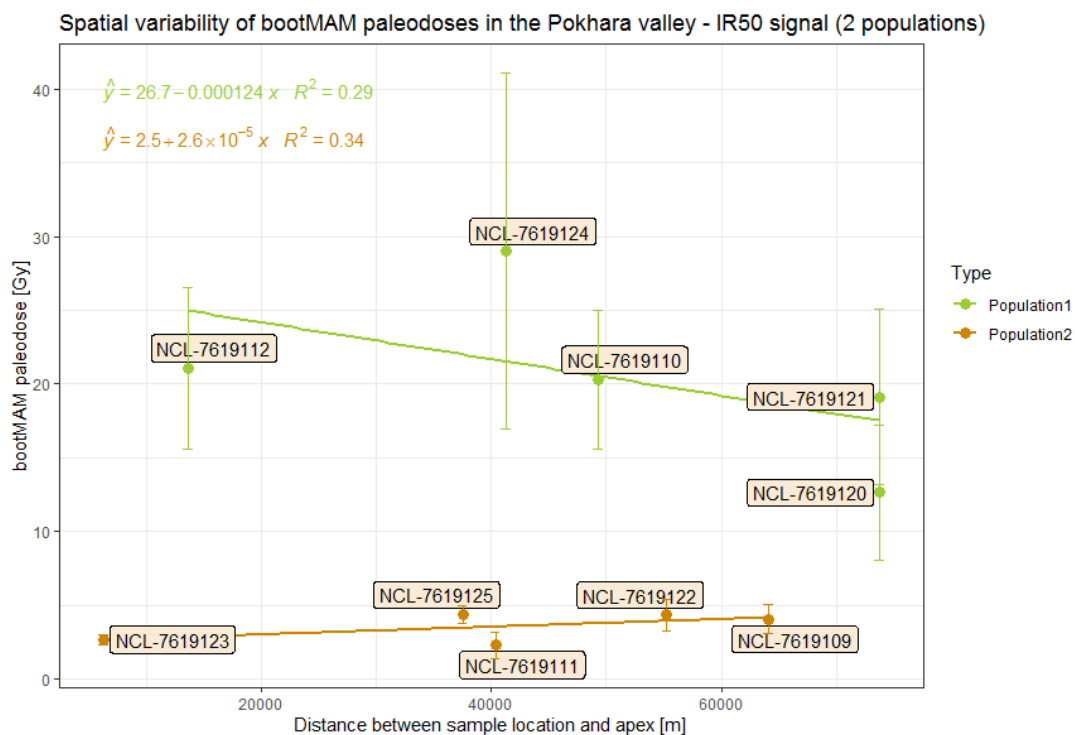


Figure 15: Paleodoses [Gy] of the IRSL50 signal as obtained by application of the bootMAM in their spatial context. The x-axis represents the distance between the fan apex at Mirsa to the sampling locations. Distance is calculated along river network and expressed in meters. A linear regression model is applied to obtain the R^2 value.

In figure 16 the paleodoses of the pIRIR150 signal are plotted over the fan length. Within the data of the pIRIR150 signal there seems not to be a clear presence of different populations as for the IRSL50 data, for that reason only one linear regression model is fitted to the pIRIR150 paleodose data. The low R^2 of 0.0064 indicates that variations in the pIRIR150 paleodoses can hardly be explained by spatial variability. If comparing the absolute values of the paleodoses of both signals with each other, it is clear that there are more differences between samples in heterogeneous bleaching for the pIRIR150 signal. The paleodoses of the IRSL50 signal range between a few Gray up to 30 Gray, whilst the pIRIR150 paleodoses vary between a few Gray up to over 300 Gray (note: the y-axes of figure 15 and 16 are logarithmic).

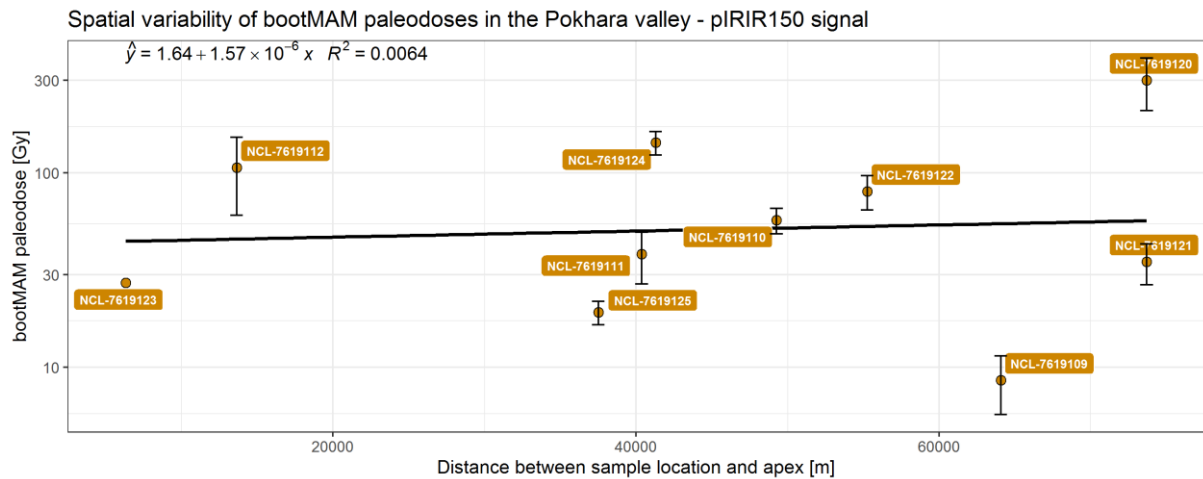


Figure 16: Paleodoses [Gy] of the pIRIR150 signal as obtained by application of the bootMAM in their spatial context. The x-axis represents the distance between the fan apex at Mirsa to the sampling locations. Distance is calculated along river network and expressed in meters. A linear regression model is applied to obtain the R^2 value.

Ghachok formation

The single-grain feldspar measurements conducted on the Ghachok samples showed that nearly all De-values were in or near saturation. For this reason, this dataset is not suitable for data analysis in the scope of this report: too less grains gave a bright measurable luminescence signal per disc. More discs should be measured in order to obtain enough De-values to determine a robust paleodose. Notwithstanding, less grains per disc emit a bright luminescence signal in comparison to grains from the Pokhara formation. This difference in IRSL sensitivity could be a measurement artefact or hint towards sediment formation sensitivity dissimilarities. However, the quantity of the data obtained in this thesis can't provide a conclusive answer.

5.2.3. Burial ages and fading rates

Table 6 and 7 show for each sample and for both feldspar signals the bootMAM paleodoses, the dose rates, burial ages and fading corrected burial ages. The paleodoses divided by the dose rate results in the burial age of a sample. Since the individual paleodoses are already described in section 5.2.2., they will not be addressed again here. The dose rate values are ranging between 2 till 4 and centred around a value of 3. As expected the dose rates are aligning for the different samples, since the sample setting is more or less equal.

The burial ages of the IRSL50 signal, as presented in table 6, show a range between 0.73 ka for the best bleached sample (NCL-7619123) and 11.78 ka for the worst bleached sample (NCL-7619124). Five out of ten samples have a burial age lower than 2 ka (samples -109, -111, -122, -123 and -125). Another observation is that the higher the burial age, the higher its uncertainty is. The subsequent column shows the fading corrected burial ages, these ages were all corrected for a fading rate of $7.20 \pm 0.89\%$ /decade. This high fading rate results in older burial ages. However, the five out of ten samples still have a burial age lower than 3 ka.

Table 6: Results per sample for the bootstrapped Minimum Age Model (bootMAM) calculated paleodoses, their corresponding dose rates, calculated burial ages and subsequently the for fading corrected burial ages of the IRSL50 signal.

NCL-numbers	bootMAM-paleodose [Gy]	Dose rates [Gy/ka]	Burial age [ka]	Burial age _ corrected [ka]
NCL-7619109	4.06 ± 1.00	3.50 ± 0.03	1.16 ± 0.28	2.22 ± 0.75
NCL-7619110	20.30 ± 4.69	3.05 ± 0.02	6.66 ± 1.54	14.07 ± 5.18
NCL-7619111	2.30 ± 0.89	2.72 ± 0.03	0.85 ± 0.33	1.59 ± 0.65
NCL-7619112	21.08 ± 5.50	3.74 ± 0.04	5.64 ± 0.23	2.28 ± 0.55
NCL-7619120	12.64 ± 4.57	3.05 ± 0.03	4.14 ± 1.50	8.50 ± 4.14
NCL-7619121	19.14 ± 5.92	2.86 ± 0.03	6.69 ± 2.07	14.13 ± 5.38
NCL-7619122	4.35 ± 1.05	2.97 ± 0.03	1.46 ± 0.35	2.84 ± 1.08
NCL-7619123	2.69 ± 0.34	3.67 ± 0.03	0.73 ± 0.09	1.37 ± 0.27
NCL-7619124	28.99 ± 12.07	2.46 ± 0.02	11.78 ± 4.91	25.73 ± 8913.71
NCL-7619125	4.38 ± 0.60	3.65 ± 0.03	1.20 ± 0.16	2.31 ± 0.45

Table 7: Results per sample for the bootstrapped Minimum Age Model (bootMAM) calculated paleodoses, their corresponding dose rates, calculated burial ages and subsequently the for fading corrected burial ages of the pIRIR150 signal. *error could not be calculated.

NCL-numbers	bootMAM-paleodose [Gy]	Dose rates [Gy/ka]	Burial age [ka]	Burial age _ corrected [ka]
NCL-7619109	8.57 ± 2.85	3.50 ± 0.03	2.45 ± 0.81	2.63 ± 0.87
NCL-7619110	57.12 ± 8.66	3.05 ± 0.02	18.75 ± 2.84	20.33 ± 3.79
NCL-7619111	38.22 ± 11.39	2.72 ± 0.03	14.06 ± 4.19	15.23 ± 5.07
NCL-7619112	106.48 ± 46.08	3.74 ± 0.04	28.47 ± 12.32	30.93 ± 11.15
NCL-7619120	299.30 ± 90.39	3.05 ± 0.03	98.01 ± 29.61	107.01 ± 34.42
NCL-7619121	34.83 ± 8.30	2.86 ± 0.03	12.17 ± 2.90	13.18 ± 3.53
NCL-7619122	80.45 ± 16.16	2.97 ± 0.03	27.07 ± 5.44	29.40 ± 6.04
NCL-7619123	27.19*	3.67 ± 0.03	7.40*	*
NCL-7619124	143.12 ± 19.82	2.46 ± 0.02	58.16 ± 8.07	63.37 ± 10.73
NCL-7619125	19.17 ± 2.62	3.65 ± 0.03	5.26 ± 0.72	5.67 ± 0.87

The burial ages of the pIRIR150 signal, as presented in table 7, show a range between 2.45 ka for the best bleached sample (NCL-7619109) and 98.01 ka for the worst bleached sample (NCL-7619120). The range in burial ages is very high and there is not that much consensus between the different samples. As described in the background it is expected from literature that the fading rate for the pIRIR150 is much lower than for the IRSL50 signal, this hypothesis is confirmed within this research. All burial ages are corrected for a fading rate of 0.89 ± 0.87 %/decade.

5.2.4. Radiocarbon overestimation ratio

Figure 17 shows the radiocarbon overestimation ratio over the Pokhara fan length for the IRSL50 signal. This ratio assesses the overestimation by the obtained luminescence burial ages in comparison to a best guessed age of the radiocarbon dataset, since it is expected that all deposits belong to the same single event. Two out of ten samples (NCL-7619111 and -123) agree within unity with the radiocarbon averaged age within their two sigma uncertainty. In total 5 out of 10 samples (NCL-7619109, -111, -112, -123 and -125) have an overestimation ratio of less than a factor of 3, those samples correspond to the samples indicated as population2 in figure 15. A higher overestimation ratio value means that the dated burial age (IRSL50 signal) overestimates the “true burial age”, as determined by the radiocarbon dataset, more. The average offset ratio is 8.55 ± 3.29 and the average age offset is 6.63 ± 2.18 [ka]. The ratio and age offset values are clearly higher than the offset values shown by population2. This interpretation supports the choice to divide the IRSL50 data into two subpopulations, as shown in figure 15.

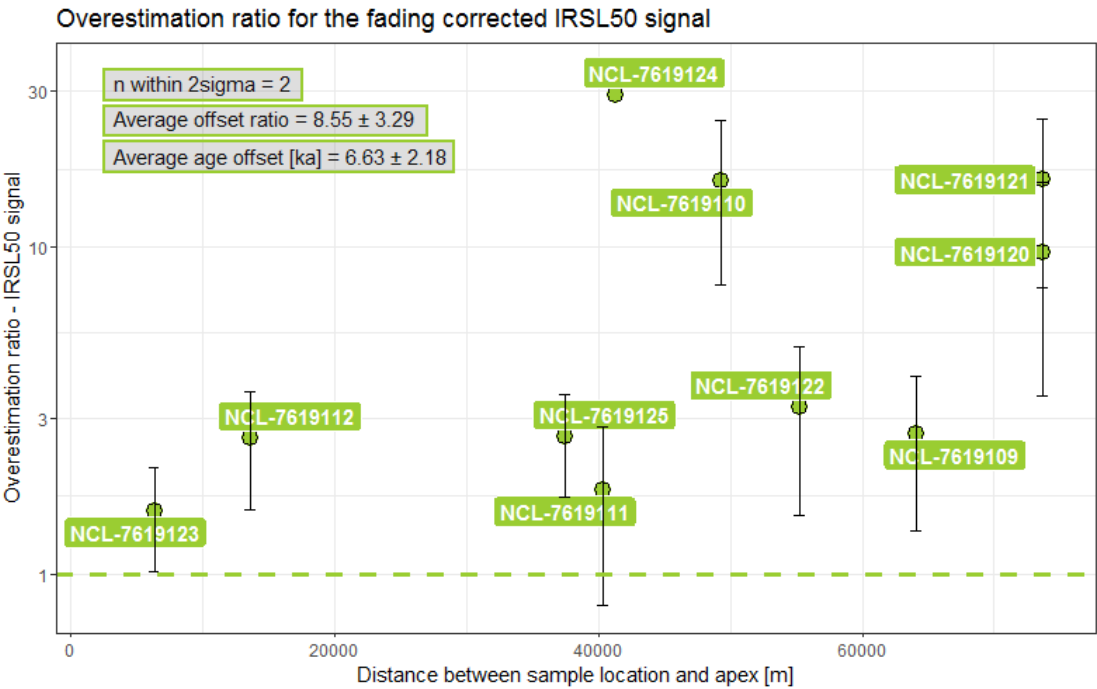


Figure 17: Radiocarbon overestimation ratio [-] for the IRSL50 signal, plotted against the distance between sample location and fan apex [m]. Distance is calculated along river network and expressed in meters. The dotted line indicates a ratio of 1; which corresponds with the averaged radiocarbon age. Furthermore, the amount of samples which are in unity with the radiocarbon age within their two sigma uncertainty, the average age offset ratio and the average age offset [ka], are shown in the graph.

Figure 18 shows the radiocarbon overestimation ratio over the Pokhara fan length for the pIRIR150 signal. Zero out of ten samples agree within unity with the radiocarbon averaged age within their two sigma uncertainty. In total only 2 out of 10 samples (NCL-7619109, and -125) have an overestimation ratio of less than a factor of 10. The average offset ratio is 36.38 ± 15.19 and the average age offset is 31.10 ± 8.62 [ka]. The ratio and age offset values are clearly higher than the offset values shown by the IRSL50 signal. This interpretation supports the choice to use the IRSL50 signal for burial age dating purposes within the scope of this thesis.

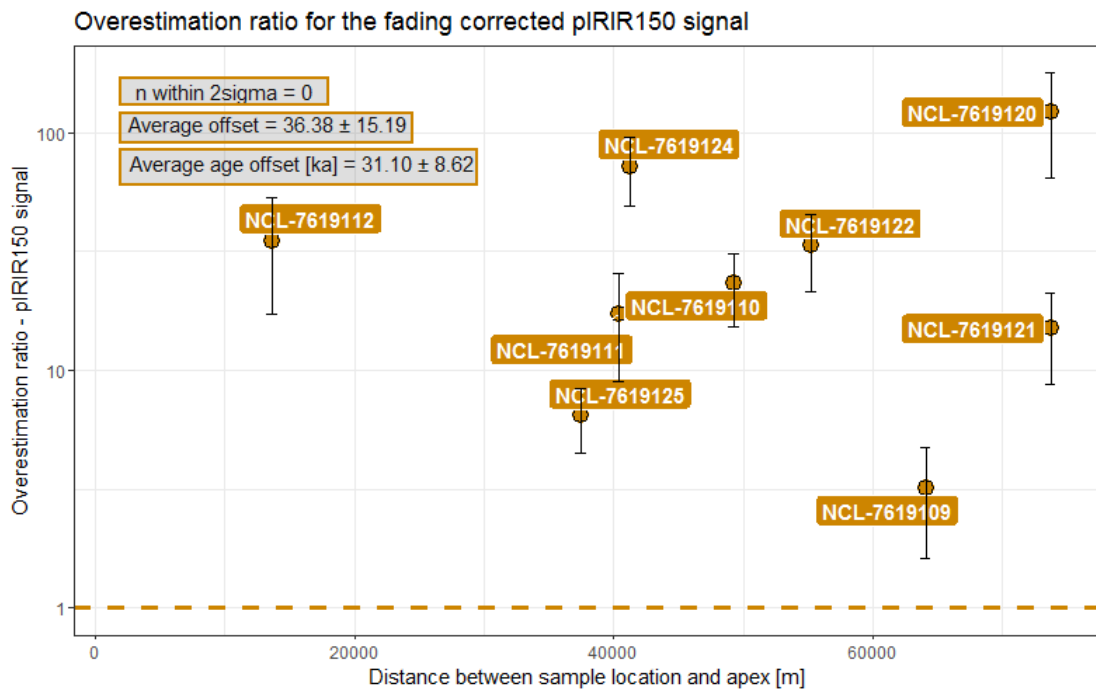


Figure 18: Radiocarbon overestimation ratio [-] for the pIRIR150 signal, plotted against the distance between sample location and fan apex [m]. Distance is calculated along river network and expressed in meters. The dotted line indicates a ratio of 1; which corresponds with the averaged radiocarbon age. Furthermore, the amount of samples which are in unity with the radiocarbon age within their two sigma uncertainty, the average age offset ratio and the average age offset [ka], are shown in the graph.

5.3. Reconstructing sediment dynamics

5.3.1. Saturation proxy

The saturation proxy is expressing the percentage of grains of the total population measured that is in saturation. Figure 19 shows this proxy in its spatial context, the percentages are ranging between the values 70 and 100. A bootstrapped version ($n = 1000$) of the linear regression model is applied, additionally the confidence intervals around the obtained regression line are indicated. A slight trend is visible from the plot: the further away from the apex, the higher the percentage of grains in saturation. A R^2 of 0.17 shows that at least a part of the dependent variable (% of grains) can be explained by the independent variable (distance between apex and sample location). However, this is a weak relationship.

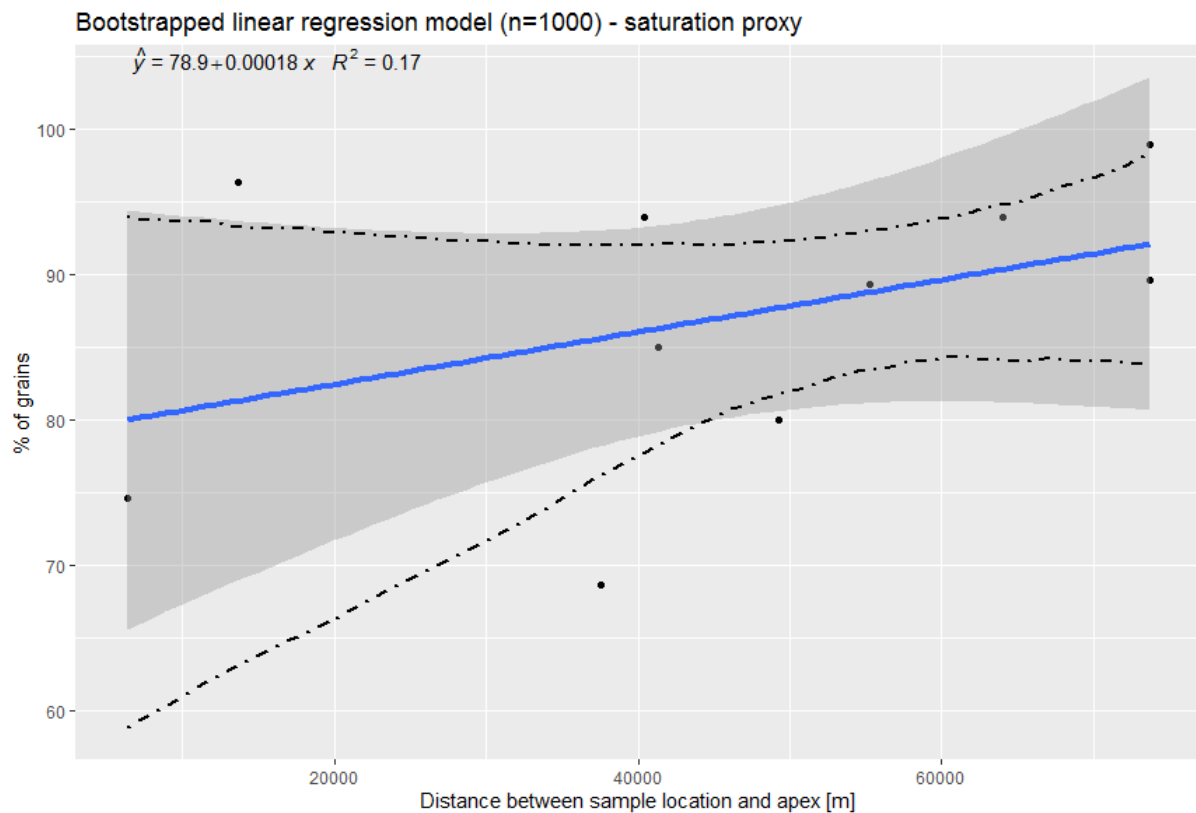


Figure 19: Spatial distribution of the saturation proxy [%] over the course of the Pokhara formation, based on the pIR150 dataset.

5.3.2. BootMAM proxy

The bootMAM proxy is expressed in the percentage of grains of the total population of which the uncertainties (2 sigma) around their De-values coincides with the estimated paleodose of the sample. A bootstrapped version (n = 1000) of the linear regression model is applied, additionally the confidence intervals around the obtained regression line are indicated. Figure 20 shows the spatial dependency of the proxy, according to the R^2 of 0.1 the spatial dependency of the bootMAM proxy is very low and not an important explainable factor in the variation of this proxy.

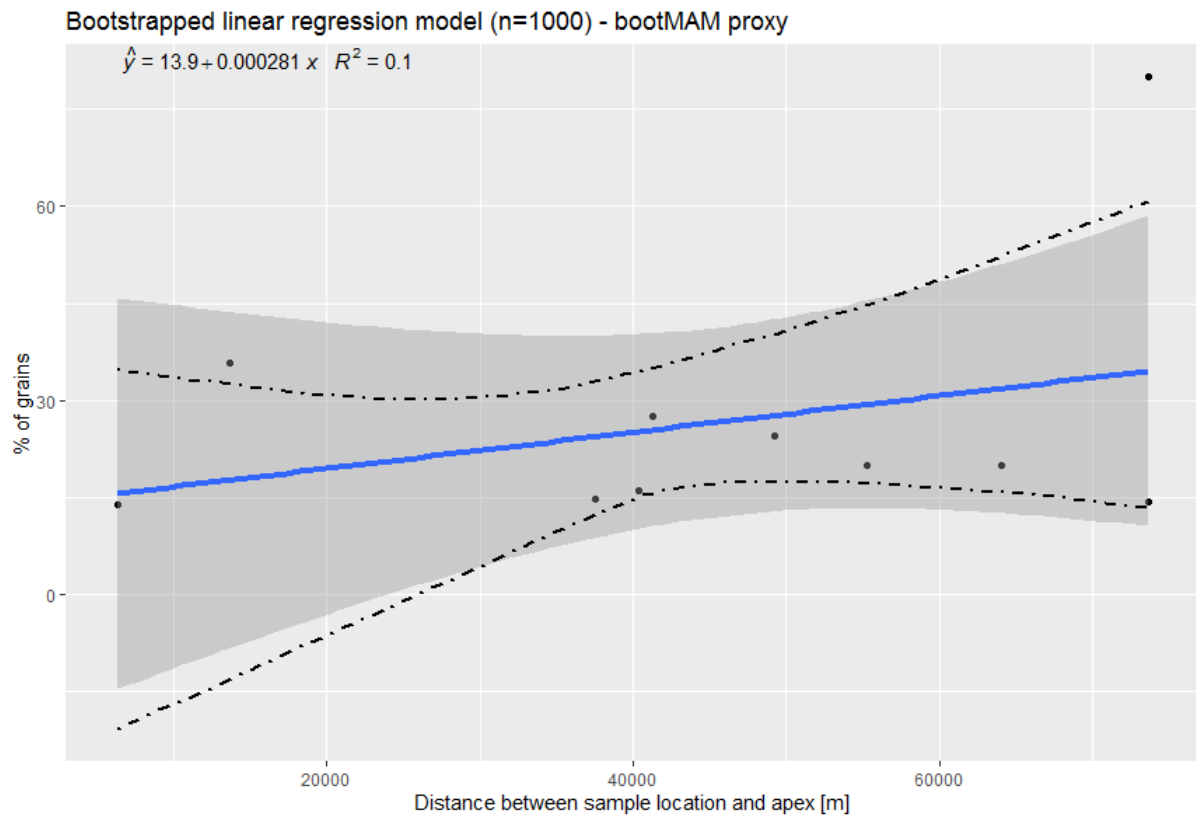


Figure 20: Spatial distribution of the bootMAM proxy [%] over the course of the Pokhara formation, based on the pIRIR150 dataset.

6. Discussion

6.1. Potential of luminescence dating in catastrophic settings

As expected from literature (Jaiswal *et al.*, 2009; Preusser *et al.*, 2006), dating quartz minerals (on a single-grain level) is virtually impossible for the field setting of this study. The measured quartz minerals showed less than 1% luminescence signal sensitivity. Therefore over 150 single-grain discs should be measured in order to retrieve enough De-measurements for reliable burial dating applications (Rodnight *et al.*, 2006). The insensitivity of the quartz luminescence properties in this setting is probably due to a combination of short transport distances and the fact that the quartz is sourced from close proximity metamorphic bedrock. Quartz minerals grow sensitisation after repeated (natural) irradiation and bleaching cycles (Preusser *et al.*, 2006). As a result of that, the luminescence insensitivity is mainly the effect of the immature sedimentary history of the grains.

Considering the poor quartz sensitivity, the focus is shifted to the use of feldspar minerals. To assess the introduced SAR-measurement protocol, a dose recovery test is conducted for both feldspar signals (IRSL50 and pIRIR150). The results of the dose recovery test show that the IRSL50 dose recovery ratio is conservative: 0.88 ± 0.01 (IRSL50). Whilst the pIRIR150 dose recovery ratio fits well within the acceptance range: 0.95 ± 0.01 (pIRIR150). The conservative IRSL50 ratio probably indicates problems with the sensitivity correction. High laboratory residual doses imply that there is an unbleachable component within the feldspar mineral. The residual dose is in general relatively bigger for younger sediments than for older ones (Preusser *et al.*, 2007). The term residual dose should not be confused with the remnant dose, the remnant dose is the natural dose remaining within the mineral where the residual dose is always a laboratory obtained measurement dose (R. Kars *et al.*, 2014). Consequently, no correction is conducted for the residual dose on the natural De-measurements, since it does not provide useful information on the remnant dose for this catastrophic depositional setting (R. Kars *et al.*, 2014). In lieu of corrections, the radiocarbon benchmark is used to get an estimation of the remnant dose within the luminescence data, in the form of an overestimation ratio.

In the calculation of the recovered doses, the Central Age Model (CAM) is applied. Because all samples are from the same lithological unit, one could expect that results will show one population and that there are no differences between the samples in terms of received microdosimetry. Based on this assumption, application of the CAM seems valid. The low IRSL50 recovered doses calculated with the CAM indicate the possibility of another contributing process.

A possible explanation could lie in temperature dependent change of the electron trap efficiency. In a dose recovery test the sample is only bleached and not preheated or irradiated. Because the sample is not preheated, the trap efficiency of a dose recovery measurement should be 100% (Wallinga *et al.*, 2000). Since the dose recovery measurements suggest a systematic underestimation of more than 10% for the IRSL50, it could be that trap efficiency influenced the measurements. However, it is important to keep in mind that all dose recovery measurements are only performed on one sample (NCL-7619125). In measuring the De-values samples are always preheated, thereby increasing the trap efficiency of electrons which results in an overestimation of the De-value. To prevent De-overestimation as much as possible, a low preheat temperature of 175 °C is applied on the single-grain feldspar measurements

(Appendix I). A SARA-SAR test can be conducted to test possible sensitivity changes (R. Kars *et al.*, 2014). An added dose protocol would have to be applied and results have to be plotted against the SAR-De values. If the slope of the line equals one, there would be no trap efficiency change. The line is extrapolated on the y-axis to obtain the SARA-De. If this value exceeds the SAR-De, trapping efficiency changes are present within the sample. Unfortunately, the SARA-SAR test could not be performed in the scope of this thesis due to laboratory closure related to the 2020 COVID19 pandemic. With results of the SARA-SAR test the current measurement protocol could be changed by optimizing the combination of preheat and measurement temperature.

As described in the result section, only the IRSL50 signal is used for burial age dating in this field setting. The IRSL50 signal is better bleached than the pIRIR150 signals, as is clear from the radial and KDE plots by smaller De-value ranges and less data scatter. However, this does not imply that the IRSL50 is well-bleached: the De-measurements still vary widely for this signal. In general the luminescence signal of IRSL50 is easier to bleach than the pIRIR150 signal (Thomsen *et al.*, 2008). However, the expected subaquatic transport conditions can presumably hamper sufficient light stimulation for resetting the signals. The effects, on different quartz and/ or feldspar signal resetting, of subaquatic transport are not crystallized out yet (Mayank Jain *et al.*, 2004; Stokes *et al.*, 2001). The better bleached IRSL50 signal is favourable in retrieving a paleodose from the De-distributions for burial dating of the sediment body. Considering this argumentation, it is valid to only interpret IRSL50 burial ages. On the other hand, the pIRIR150 signal is preferred to apply for sediment process reconstruction, since this signal is more stable and less prone to anomalous fading. The pIRIR150 signal is profitable to use in this case, the slower bleaching rate results in longer records of bleaching information than are captured by the faster resetting IRSL50 signal.

In order to retrieve the youngest subpopulation from the total population, a bootstrapped version of the Minimum Age Model (MAM) is applied. The youngest subpopulation is extracted, since this population represents the well-bleached grains within the heterogeneous distributions. Use of the bootstrapped MAM is in agreement with literature about the event type (Brill *et al.*, 2018; Cunningham & Wallinga, 2012), since the dynamic nature of the event leads to poor bleaching and therefore only certain grains are expected to be well-bleached and thus representing the burial age.

The IRSL50 and pIRIR150 burial age information is presented in table 6 and 7, respectively. Both tables contain the bootMAM-paleodoses [Gy], the dose rates [gy/ka], the burial ages [ka] and the for anomalous fading corrected burial ages [ka]. The dose rate values are aligning with each other, which could be expected since all samples are originating from the same sedimentological unit. The varying IRSL50 and pIRIR150 fading corrected burial ages indicate disagreement about the “true burial age”. The radiocarbon overestimation graphs, in figure 17 (IRSL50 signal) and in figure 18 (for the pIRIR150 signal), show important information in retrieving the “true burial age”. The best guessed radiocarbon age is determined at an average of 0.82 ± 0.49 ka (n=26), ideally this estimation would be replaced by an statistical substantiated age range. Notwithstanding, in the scope of this study the average value of previously published radiocarbon data is used. The newly obtained radiocarbon ages within this study still have to be calibrated. The uncalibrated ages are determined by the *Poznan Radiocarbon Laboratory* at 840 ± 30 BP and 910 ± 30 BP, both samples are taken at the location of OSL sample NCL-7619120

(and -121). The burial age of luminescence samples NCL-7619120 (and -121) are determined on 4.14 ± 1.50 [ka] and 6.69 ± 2.07 [ka] (non-fading corrected ages). However, a comparison with the newly obtained radiocarbon ages is not valuable since they are not calibrated.

As described in the results, figure 17 shows that 2 out of 10 samples (20%) agree within unity with the radiocarbon age within their two sigma uncertainty. Moreover, 5 out of 10 samples (50%) yield burial ages of the Pokhara formation overestimating the “true burial” age with a factor less than 3, those samples represent a distinct population (pop2) within the dataset (figure 15). The samples in unity with the radiocarbon burial age are representing Medieval burial ages: 1.59 ± 0.65 ka (NCL-7619111) and 1.37 ± 0.27 ka (NCL-7619123) and are thus aligning with the Medieval event age as described by Schwanghart et al. (2016). The IRSL50 burial ages are fading corrected for the high fading rate of 7.20 ± 0.89 %/decade. Since laboratory fading rates are often an overestimation of the true fading rate within the sample (A. Murray *et al.*, 2012), it can be expected that the “true burial age” and the radiocarbon overestimation ratio of the luminescence samples can be expected to be lower. The fading measurements in the scope of this thesis were conducted on multi-grain level. Preferable an additional single-grain fading procedure would be performed in order to retrieve a bootstrapped-MAM version from the g-values, instead of using an clearly overestimating average. Keeping in mind the catastrophic nature of this event which complicates luminescence dating in general, 20% of the IRSL50 samples succeeds well in determining the “true burial age” of the Pokhara formation. For the pIRIR150 samples this is a different story: 0 out of 10 samples agreed within unity with the radiocarbon age within their two sigma uncertainty (figure 18).

Against expectations the IRSL50 signal seems more suitable for dating applications in catastrophic sediment settings where the chance of poor bleaching, due to for example turbid flow conditions, is very high. Beforehand it was expected that the pIRIR150 signal would be of more potential in dating this settings, since this signal is more stable than the IRSL50 signal. However, the faster bleaching potential of the IRSL50 signal resulted in its luminescence dating applicability. Since 20% of the IRSL50 samples yields a systematic error of the true burial age plausible with the best guess of the radiocarbon age dataset, it can be concluded that this method could also be applied in similar low-frequency high-magnitude sedimentological settings without the use of an independent age checker. Sample NCL-7619123 is part of that 20% and is marked by some interesting statistics: the percentage of grains assigned to the bootMAM-value ($n=116$ (IRSL50) and $n=76$ (pIRIR150)) is higher than the average ($n=44$ (IRSL50) and $n=39$ (pIRIR150)) and the percentage of saturated grains is ($n=75$ (IRSL50) and $n=11$ (pIRIR150)) lower than the average ($n=167$ (IRSL50) and $n=13$ (pIRIR150))) (Appendix II & III). To distinguish between samples representing the “true burial age” and samples overestimating this age in setting without age control, it could be useful to look at the samples with the highest percentages of grains assigned to the bootMAM value and the lowest percentages of saturated grains. Moreover, the calculated systematic age offset values, which represent the remnant dose range (displayed in figures 17 and 18), underline this theory. The average age offset for the IRSL50 signal is 6.63 ± 2.18 ka, for the pIRIR150 signal it is much higher at 31.10 ± 8.62 ka. As indicated earlier, it is valid to expect lower remnant dose ranges, and therefore higher reliability of luminescence burial dating in catastrophic settings, if more sophisticated anomalous fading corrections are applied. All in all, dating similar

catastrophic mass movements by the use of (IRSL50) feldspar signals clearly shows potential, even when no independent age control is available as is the unique case for this study.

The Medieval burial age of this field setting is very young on a geological timescale. Another main advantage of using feldspar minerals is its property to grow higher doses than quartz, therefore dating feldspar signals can go as far back as a few hundred thousand years (Auclair *et al.*, 2003; Wallinga *et al.*, 2007). The ability of feldspar minerals to grow high doses in combination with the proven potential for dating low-frequency high-magnitude events in this study, is promising in applying this knowledge for comparable settings but on different geological timescales. On longer timescales, the contribution of the systematic error, related to insufficient bleaching, will be relatively smaller for older burial ages. For this reason, it is expected that there is an even more promising application in dating highly dynamic events further back on the geological timescale.

6.2. Potential of luminescence in reconstructing mass movement processes

The spatial distributions of the paleodoses, as presented in figure 15 (IRSL50) and figure 16 (pIRIR150), show in general the same correlation between spatial variability and the paleodoses: a clear trend is lacking. Although, the IRSL50 paleodoses can be subdivided into two populations: one centring around a paleodose of roughly 3 Gy and one population centring around 20 Gy. By subdividing the IRSL50 paleodoses in two populations, the r-squared value improved: from 0,041 for all the IRSL50 paleodoses to 0.29 for population1 and 0.34 for population 2 (figure 15). Population1 shows a slight decreasing trend over transport distance, whilst population2 shows a slight increasing trend. The r-squared for the pIRIR150 signal is significantly lower: 0,0064. The presence of two paleodose populations (IRSL50) could mean that there has been a reactivation of the mass movement event. However, this is not reflected by the pIRIR150 data, which is a more stable signal than the IRSL50 signal. Therefore, it is hard to draw an unified conclusion about this hypothesis; more samples spread over the Pokhara fan could enlighten this topic. On the other hand, the results provide information on the mass movement process itself: the lack of spatial correlation of the paleodoses is consistent with the hypothesized event dynamics. An earthquake induced displacement of sediment is associated with turbid flow conditions in which light exposure is limited (Reimann *et al.*, 2015). This limited light exposure results in insufficient resetting of the luminescence signal and therefore in poor bleaching and non-spatial dependent paleodose variations. Therefore the lack of correlation is convenient in highlighting the dynamic nature of the deposition event.

The dynamic event nature is underlined by the results of the saturation and bootMAM proxies (figure 19 and 20). The saturation proxy shows a slight positive correlation for the percentage of grains in saturation over the fan apex with a low R^2 of 0.17. This proxy tells something about the percentage of bedrock grains without an exposure history present in the sample. According to the work of Bonnet *et al.* (2019), this proxy is expected to reflect somehow the flux of bedrock grains: the higher the percentage of grains in saturation, the more bedrock grains are in situ. Therefore it might be a measure of local denudation rates: the higher the percentage of bedrock grains, the higher the denudation rate should have been to obtain this higher percentage of bedrock grains. Beforehand, it was expected that the saturation proxy would reflect the highest percentages of grains in saturation closest to the apex. Thereby reflecting extreme turbid conditions and therefore possibly higher denudation rates at the

spatial onset of the event. However, the bootstrapped linear regression model shows that there is only a weak correlation between the saturation proxy and spatial variability. The results, as presented in figure 19, only substantiate the catastrophic nature of the mass movement event. Since the saturation proxy shows weak spatial correlation, no differences in bedrock input over the course of the Pokhara fan can be expected. If the bedrock input is truly representing denudation rates, then no strong varying denudation rates can be extracted from the obtained saturation proxy. The confidence intervals around the regression line show that proximal and distal from the apex, the intervals are the broadest. Presumably, since those locations are underrepresented in the amount of sampling locations.

The bootMAM proxy, as presented in figure 20, also does not show a clear spatial correlation, the R^2 is as low as 0.1. This means that there is no spatial variation in the amount of well-bleached grains contributing to the bootMAM paleodose calculation. Thereby implying that there is no difference in the amount of bleaching over the course of the Pokhara fan. This knowledge further imposes that the nature of the event is very turbid.

The concept of reconstructing sediment processes is a novel tool in luminescence research applications (Bonnet *et al.*, 2019; Chamberlain & Wallinga, 2019; Riedesel *et al.*, 2018). Bonnet *et al.* (2019) applied sediment tracing techniques on fluvial sediments deposited under extreme conditions and could prove its functionality by deriving a relationship between high river terrace incision rates and fewer bleached grains. The work of this study shows additionally that reconstructing sediment processes is also applicable on catastrophic low-frequency high-magnitude events, thereby enabling to corroborate the dynamic nature of the event.

6.3. Local sediment dynamics of the Pokhara valley

The newly obtained luminescence burial ages substantiate the Medieval age indications as obtained by Schwanghart *et al.* (2016). 20% agreement of the luminescence IRSL50 burial ages with the calibrated radiocarbon ages confirm that the mass movement event (Pokhara formation deposits) took place during the Middle Ages, ranging between 1.37 ± 0.27 and 1.59 ± 0.65 . However, 80% of the determined IRSL50 paleodoses overestimated the radiocarbon burial age. This seems to be of significant value that it is too uncertain to conclude that the mass movement deposits certainly are of Medieval age. Nonetheless, the Medieval age can be underlined by assessing statistical parameters of the paleodose calculations (n , 2sigma range and n_{sat}). The 20% IRSL50 paleodoses in unity with the radiocarbon ages, show a higher number of grains contributing to the paleodose calculation and a lower amount of grains in saturation than the 80% of the IRSL50 burial ages which are in disagreement with the radiocarbon age.

The IRSL50 burial ages are dividable into two age populations (figure 15). The fading corrected burial ages of population1 range between 8.50 ± 4.14 and 25.73 ± 8913.71 ka and of population2 between 1.37 ± 0.27 and 2.84 ± 1.08 ka. As discussed previously, it could well be that the two populations indicate reactivation of the mass movement dynamics. The first population could reflect late-Pleistocene fan building and the second population could reflect younger Holocene reactivation. However, the non-corrected fading burial ages of the IRSL50 signal (Table 6) indicate a younger age. As extensively described in this thesis, the measured laboratory anomalous fading rates are expected to be

overestimated and are therefore not seen as the true natural fading rates (A. Murray *et al.*, 2012). Therefore, it is highly likely that the Pokhara formation has a Medieval burial age. Additional samples and anomalous fading rate studies, could lead to preclusions.

The age offset values, as presented in figure 17 (IRSL50) and figure 18 (pIRIR150), clearly indicate that the IRSL50 is more suitable in obtaining a valid luminescence burial age than the pIRIR150 signal, if compared with radiocarbon ages as benchmark. The IRSL50 signal is on average overestimating the Pokhara formation burial age by 6.63 ± 2.18 ka, whilst the pIRIR150 signal overestimates it by 31.10 ± 8.62 ka on average. However, the previous paragraph showed how important it is to use additional statistical parameters and caution with fading rates, in order to derive a reliable burial age for catastrophic mass movement deposits.

The sample location lithology as shown in Appendix IV, the detailed lithological descriptions made by Stolle (2017) and the mass movement process reconstruction results (section 6.2) confirm the turbid character behind the mass movement deposits. There are no big lithological changes within the sediment body, however it seems that the grain size decreases with increasing distance to the apex. A decreasing grain size over transport distance is expectable, since heavier particles settle out of flow in earlier transport stages (Pratt-Sitaula *et al.*, 2007). Moreover, it is likely that earthquake activity has been the triggering factor for this catastrophic event. As described in the geology section, both the geological and climatological circumstances could have functioned as non-limiting conditional factors.

As described in the result section the single-grain feldspar measurements on the Ghachok samples unfortunately did not result in a good burial age dataset. Almost all grains were in saturation, this can be a consequence of very poor bleaching mechanisms and/ or infinitely old grains. In literature it is indicated that the Ghachok formation could have a burial age of 10.000 years BP (Yamanaka, 1982). Unfortunately, this age indication could not be accepted or rejected with the results in this study. In order to establish a more detailed geochronology of the Pokhara valley, the Ghachok and even the Tallakot formation should be dated (by luminescence) in the future. However, due to the calcification and concretion of both outcrops this remains a challenge. The positive side of the high saturation levels is that the very limited light exposure probably means that the Ghachok deposits could have the same dynamics origin mechanism as the Pokhara deposits. Since the Ghachok data is only based on two samples, conclusions are hard to drawn at this point of research.

7. Conclusions

Single-grain feldspar luminescence dating is proven to be a suitable method in obtaining burial ages for catastrophic mass movement deposits in highly dynamic mountain ranges such as the Himalayas. Burial ages are obtained for the Pokhara formation, unfortunately more Ghachok samples should be studied in order to also obtain burial ages for these stratigraphically older deposits. Against expectations, the anomalous fading suffering IRSL50 signal turned out to overestimate the independent calibrated radiocarbon dataset less than the pIRIR150 signal. 20% of the burial ages obtained by the IRSL50 signal show a reproduction of the radiocarbon age within 2sigma uncertainty, thereby confirming the Medieval age of the mass movement event in the Pokhara valley [Nepal]. 0% of the pIRIR150 burial ages show reproduction of the radiocarbon age within 2sigma. In comparable settings without age control, "true burial ages" derived from the IRSL50 signal can be pinned down by looking at additional sample statistics. The 20% samples reproducing the radiocarbon age in this study, distinguish themselves from the other samples by a higher number of grains contributing to the bootMAM-paleodose and a lower number of grains in saturation than on average. The proven potential of luminescence burial dating in catastrophic settings, leads to dating possibilities in similar setting where no other age control is available. It is also advantageous that feldspar burial dating can go as far back as a few hundred thousand years, which is definitely not the case for radiocarbon dating (figure 1). Moreover, the systematic uncertainty, due to heterogeneous bleaching related to catastrophic event dynamics, is relatively lower for older deposits. Therefore, presumably leading to less age overestimation if dating geologically older deposits.

The stable pIRIR150 signal proves its benefits in reconstructing the transport dynamics of the Pokhara formation. The heterogeneous bleaching patterns indicate highly turbid flow conditions of the water-lain sediments, in which grains were limitedly exposed to light resulting in poor-bleaching. The IRSL50 paleodose distributions indicate two populations (figure 15), possibly implying reactivation of the fan. Since this trend is not shown by paleodoses of the more stable pIRIR150 signal, an unified conclusion can't be drawn. All in all, clear is that the deposition environment had to be very dynamic in order to explain the obtained paleodose distributions. The saturation proxy - assessing the percentage of grains that were not light exposed during transport - as well as the bootMAM proxy - assessing the percentage of well-bleached grains present - underline the catastrophic nature of the event. Absence of clear spatial correlations, imply that over the whole course of the Pokhara formation the sediments were deposited under similar turbid conditions without variations in denudation and bleaching rates. The Ghachok formation could well be deposited in a comparable dynamic transport setting, high percentages of saturated grains indicate turbid conditions as well. The application of poorly bleached samples to reflect transport dynamics is a novel luminescence tool: the insights into transport dynamics obtained within this study, entails promising applications in future research in similar dynamic settings.

8. Recommendations

As mentioned in the discussion, conducting a SARA-SAR test could give insight if trap efficiency changes occurred within the samples used in this study (R. Kars *et al.*, 2014). Extensive application of the dose recovery test could in combination with the SARA-SAR test results help in optimizing the measurement protocol. Moreover, an additive (single-grain) study of the anomalous fading rates has the potential to ensure the reliability of the laboratory fading corrections made.

The laboratory anomalous fading rate of the IRSL50 signal is clearly overestimated, which is in general the case when assessing fading in a laboratory (A. Murray *et al.*, 2012). The fading rates are based on multi-grain measurements. By measuring on single-grain level, it would be possible to apply a Minimum Age Model (MAM) on the g-value distribution. In this way a MAM g-value could be extracted per sample instead of using one average for all samples. Then, it is possible to see if variations in g-values can be related to bleaching and/or spatial patterns. Moreover, the MAM g-value presumably will be lower than the average g-value applied in this study and therefore could improve age offset ranges and burial age determinations.

The valley of the Mardi Khola is situated just westwards of the Pokhara valley and featured with some beautiful river terraces. Since the potential of burial age dating and sediment dynamics reconstruction in this region is proven by the Pokhara valley case-study, this concept could also be applied to the Mardi Khola valley. However, in this different geomorphological setting, sediment reconstructing is promising in deriving erosion rate patterns of river terrace incision. Erosion rates can eventually be translated into local landscape dynamics as shown by Bonnet (2019) for the Rangitikei River catchment in New Zealand. Studying a river valley within the same geological and climatic settings but with less dynamic transport dynamics offers opportunities to complement this current study.

Acknowledgments

The process of writing my MSc thesis was a pleasure and even convinced me to further develop a career in science. I enjoyed the combination of breath-taking fieldwork in Nepal, dark hours in the luminescence laboratory and discussing the results.

First of all, I want to thank Tony Reimann giving me the opportunity to work on this challenging but most of all exciting project. I also value your critical input and the time you took for our discussions. I want to thank Jakob Wallinga for his critical and supportive feedback on my work. Wolfgang Schwanghart and Jürgen Mey, I want to thank both of you for the pleasurable field trip and sharing your (field) knowledge with me. Moreover, I appreciate the enthusiasm of Basanta Raj Adhikari in the field about local geology and Nepalese culture. I also want to thank Erna and Alice for their support. The skilled help from Erna Voskuilen helped me to conduct my luminescence measurements smoothly in the laboratory. The motivational talks and in-depth luminescence discussions with Alice Versendaal were very welcome. I enjoyed the geological discussions with Selçuk Aksay and our occasional laughs in the laboratory. Last I want to thank my two dear friends, Vera and Xander, for their support and humourful distractions.

References

- Aitken, M. J. (1998). *Introduction to optical dating: the dating of Quaternary sediments by the use of photon-stimulated luminescence*: Clarendon Press.
- Anoop, A., Prasad, S., Basavaiah, N., Brauer, A., Shahzad, F., & Deenadayalan, K. (2012). Tectonic versus climate influence on landscape evolution: A case study from the upper Spiti valley, NW Himalaya. *Geomorphology*, 145-146, 32-44.
- Auclair, M., Lamothe, M., & Huot, S. (2003). Measurement of anomalous fading for feldspar IRSL using SAR. *Radiation Measurements*, 37(4), 487-492.
- Avouac, J.-P. (2015). Mountain Building: From earthquakes to geological deformation. *Treatise on geophysics*, 6, 381-432.
- Bollinger, L., Sapkota, S. N., Tapponnier, P., Klinger, Y., Rizza, M., Van Der Woerd, J., ... & Bes de Berc, S. (2014). Estimating the return times of great Himalayan earthquakes in eastern Nepal: Evidence from the Patu and Bardibas strands of the Main Frontal Thrust. *Journal of Geophysical Research: Solid Earth*, 119(9), 7123-7163.
- Bonnet, S., Reimann, T., Wallinga, J., Lague, D., Davy, P., & Lacoste, A. (2019). Landscape dynamics revealed by luminescence signals of feldspars from fluvial terraces. *Scientific Reports*, 9(1), 8569.
- Bookhagen, B., Thiede, R. C., & Strecker, M. R. (2005a). Abnormal monsoon years and their control on erosion and sediment flux in the high, arid northwest Himalaya. *Earth and Planetary Science Letters*, 231(1), 131-146.
- Bookhagen, B., Thiede, R. C., & Strecker, M. R. (2005b). Late Quaternary intensified monsoon phases control landscape evolution in the northwest Himalaya. *Geology*, 33(2), 149-152.
- Bookhagen, B., & Burbank, D. W. (2010). Toward a complete Himalayan hydrological budget: Spatiotemporal distribution of snowmelt and rainfall and their impact on river discharge. *Journal of Geophysical Research: Earth Surface*, 115(F3).
- Bøtter-Jensen, L., Andersen, C., Duller, G. A., & Murray, A. S. (2003). Developments in radiation, stimulation and observation facilities in luminescence measurements. *Radiation Measurements*, 37(4-5), 535-541.
- Brill, D., Reimann, T., Wallinga, J., May, S. M., Engel, M., Riedesel, S., & Brückner, H. (2018). Testing the accuracy of feldspar single grains to date late Holocene cyclone and tsunami deposits. *Quaternary Geochronology*, 48, 91-103.
- Bungum, H., Lindholm, C. D., & Mahajan, A. K. (2017). Earthquake recurrence in NW and central Himalaya. *Journal of Asian Earth Sciences*, 138, 25-37.
- Carling, P. A. (2013). Freshwater megaflood sedimentation: What can we learn about generic processes? *Earth-Science Reviews*, 125, 87-113.
- Catto, N. (2019). Handbook of Luminescence Dating. *Geoscience Canada: Journal of the Geological Association of Canada/Geoscience Canada: journal de l'Association Géologique du Canada*, 46(4), 195-196.
- Chamberlain, E. L., & Wallinga, J. (2019). Seeking enlightenment of fluvial sediment pathways by optically stimulated luminescence signal bleaching of river sediments and deltaic deposits. *Earth Surface Dynamics*, 7(3), 723-736.
- Chamberlain, E. L., Wallinga, J., Reimann, T., Goodbred Jr, S. L., Steckler, M. S., Shen, Z., & Sincavage, R. (2017). Luminescence dating of delta sediments: Novel approaches explored for the Ganges-Brahmaputra-Meghna Delta. *Quaternary Geochronology*, 41, 97-111.
- Choi, J., Kim, J., Murray, A., Hong, D., Chang, H., & Cheong, C.-S. (2009). OSL dating of marine terrace sediments on the southeastern coast of Korea with implications for Quaternary tectonics. *Quaternary international*, 199(1-2), 3-14.
- Cunha, P. P., Martins, A. A., Huot, S., Murray, A., & Raposo, L. (2008). Dating the Tejo river lower terraces in the Ródão area (Portugal) to assess the role of tectonics and uplift. *Geomorphology*, 102(1), 43-54.

- Cunningham, A. C., Evans, M., & Knight, J. (2015). Quantifying bleaching for zero-age fluvial sediment: A Bayesian approach. *Radiation Measurements*, 81, 55-61.
- Cunningham, A. C., & Wallinga, J. (2012). Realizing the potential of fluvial archives using robust OSL chronologies. *Quaternary Geochronology*, 12, 98-106.
- Dietze, M. (2012). plot_RadialPlot: Function to create a Radial Plot.
- Dietze, M., Kreutzer, S., Fuchs, M., Burow, C., Fischer, M., & Schmidt, C. (2013). A practical guide to the R package Luminescence. *Ancient TL*, 31, 11-18.
- Duller, G. (2000). Dating methods: geochronology and landscape evolution. *Progress in Physical Geography*, 24(1), 111-116.
- Duller, G. (2015). The Analyst software package for luminescence data: overview and recent improvements.
- Duller, G. A. (2006). Single grain optical dating of glacial deposits. *Quaternary Geochronology*, 1(4), 296-304.
- Duller, G. A. T. (2008). Single-grain optical dating of Quaternary sediments: why aliquot size matters in luminescence dating. *Boreas*, 37(4), 589-612.
- Eriksson, M. G., Olley, J. M., & Payton, R. W. (2000). Soil erosion history in central Tanzania based on OSL dating of colluvial and alluvial hillslope deposits. *Geomorphology*, 36(1), 107-128.
- Fort, M. (1984). Phases d'accumulations sédimentaires internes et phases orogéniques au Sud du massif de l'Annapurna: L'exemple du bassin de Pokhara (Népal). *Revue géographique des Pyrénées et du Sud-Ouest*, 1, 25-47.
- Fort, M. (1986). Glacial extension and catastrophic dynamics along the Annapurna Front, Nepal Himalaya. *Göttinger Geographische Abhandlungen*, 81, 105-125.
- Fort, M. (1987). Sporadic morphogenesis in a continental subduction setting: an example from the Annapurna Range, Nepal Himalaya. *Zeitschrift für Geomorphologie*, 63(9), 36.
- Fort, M. (1996). Late Cenozoic environmental changes and uplift on the northern side of the central Himalaya: a reappraisal from field data. *Palaeogeography, Palaeoclimatology, Palaeoecology*, 120(1-2), 123-145.
- Fort, M. (2010). The Pokhara valley: a product of a natural catastrophe. In *Geomorphological Landscapes of the World* (pp. 265-274): Springer.
- Fuchs, M., Fischer, M., & Reverman, R. (2010). Colluvial and alluvial sediment archives temporally resolved by OSL dating: Implications for reconstructing soil erosion. *Quaternary Geochronology*, 5(2), 269-273.
- Fuchs, M., & Lang, A. (2001). OSL dating of coarse-grain fluvial quartz using single-aliquot protocols on sediments from NE Peloponnese, Greece. *Quaternary Science Reviews*, 20(5-9), 783-787.
- Fuchs, M., & Owen, L. A. (2008). Luminescence dating of glacial and associated sediments: review, recommendations and future directions. *Boreas*, 37(4), 636-659.
- Gabet, E. J., Burbank, D. W., Pratt-Sitaula, B., Putkonen, J., & Bookhagen, B. (2008). Modern erosion rates in the High Himalayas of Nepal. *Earth and Planetary Science Letters*, 267(3-4), 482-494.
- Galbraith, R. F., Roberts, R. G., Laslett, G. M., Yoshida, H., & Olley, J. M. (1999). Optical dating of single and multiple grains of quartz from Jinmium rock shelter, northern Australia: Part I, experimental design and statistical models. *Archaeometry*, 41(2), 339-364.
- Gautam, P., Raj Pant, S., & Ando, H. (2000). Mapping of subsurface karst structure with gamma ray and electrical resistivity profiles: a case study from Pokhara valley, central Nepal. *Journal of Applied Geophysics*, 45(2), 97-110.
- Godfrey-Smith, D., & Cada, M. (1996). IR stimulation spectroscopy of plagioclase and potassium feldspars, and quartz. *Radiation Protection Dosimetry*, 66(1-4), 379-385.
- Godfrey-Smith, D. I., Huntley, D. J., & Chen, W.-H. (1988). Optical dating studies of quartz and feldspar sediment extracts. *Quaternary Science Reviews*, 7(3-4), 373-380.
- Gong, Z., Sun, J., Lü, T., & Tian, Z. (2014). Investigating the optically stimulated luminescence dose saturation behavior for quartz grains from dune sands in China. *Quaternary Geochronology*, 22, 137-143.

- Grandin, R., Doin, M. P., Bollinger, L., Pinel-Puységur, B., Ducret, G., Jolivet, R., & Sapkota, S. N. (2012). Long-term growth of the Himalaya inferred from interseismic InSAR measurement. *Geology*, *40*(12), 1059-1062.
- Gray, H. J., Jain, M., Sawakuchi, A. O., Mahan, S. A., & Tucker, G. E. (2019). Luminescence as a Sediment Tracer and Provenance Tool. *Reviews of Geophysics*, *0*(0).
- Gray, H. J., Tucker, G. E., Mahan, S. A., McGuire, C., & Rhodes, E. J. (2017). On extracting sediment transport information from measurements of luminescence in river sediment. *Journal of Geophysical Research: Earth Surface*, *122*(3), 654-677.
- Guralnik, B., Li, B., Jain, M., Chen, R., Paris, R. B., Murray, A. S., . . . Herman, F. (2015). Radiation-induced growth and isothermal decay of infrared-stimulated luminescence from feldspar. *Radiation Measurements*, *81*, 224-231.
- Hagen, T. (1969). Report on the Geological survey of Nepal, Vol. 1: preliminary reconnaissance. *Denkschriften der Schweizerischen Naturforschenden Gesellschaft Memoires de la Societe Helvetique des Sciences Naturelles*, *84*(1), 185.
- Hanisch, J., & Koirala, A. (2010). Pokhara Valley: a place under permanent threat. *NEPAL GEOLOGICAL SOCIETY*, 119.
- Heiri, O., Lotter, A. F., & Lemcke, G. (2001). Loss on ignition as a method for estimating organic and carbonate content in sediments: reproducibility and comparability of results. *Journal of paleolimnology*, *25*(1), 101-110.
- Hormann, K. (1974). Die Terrassen an der Seti Khola—Ein Beitrag zur quartären Morphogenese in Zentralnepal (Terraces on the Seti Khola—A Contribution to Quaternary Morphogenesis in Central Nepal). *Erdkunde*, 161-176.
- Hu, G., Yi, C.-L., Zhang, J.-F., Liu, J.-H., & Jiang, T. (2015). Luminescence dating of glacial deposits near the eastern Himalayan syntaxis using different grain-size fractions. *Quaternary Science Reviews*, *124*, 124-144.
- Huntley, D. J., Godfrey-Smith, D. I., & Thewalt, M. L. (1985). Optical dating of sediments. *Nature*, *313*(5998), 105.
- Hütt, G., Jaek, I., & Tchonka, J. (1988). Optical dating: K-feldspars optical response stimulation spectra. *Quaternary Science Reviews*, *7*(3-4), 381-385.
- Jackson, M. E., & Bilham, R. (1994). 1991–1992 GPS measurements across the Nepal Himalaya. *Geophysical Research Letters*, *21*(12), 1169-1172.
- Jain, M., & Ankjærgaard, C. (2011). Towards a non-fading signal in feldspar: insight into charge transport and tunnelling from time-resolved optically stimulated luminescence. *Radiation Measurements*, *46*(3), 292-309.
- Jain, M., Murray, A., & Botter-Jensen, L. (2004). Optically stimulated luminescence dating: how significant is incomplete light exposure in fluvial environments?[Datation par luminescence stimulée optiquement: quelle signification en cas de blanchiment incomplet des sédiments fluviaux?]. *Quaternaire*, *15*(1), 143-157.
- Jain, M., Murray, A., Bøtter-Jensen, L., & Wintle, A. (2005). A single-aliquot regenerative-dose method based on IR (1.49 eV) bleaching of the fast OSL component in quartz. *Radiation Measurements*, *39*(3), 309-318.
- Jaiswal, M. K., Bhat, M. I., Bali, B. S., Ahmad, S., & Chen, Y. G. (2009). Luminescence characteristics of quartz and feldspar from tectonically uplifted terraces in Kashmir Basin, Jammu and Kashmir, India. *Radiation Measurements*, *44*(5), 523-528.
- Karki, R., Talchabhadel, R., Aalto, J., & Baidya, S. K. (2016). New climatic classification of Nepal. *Theoretical and Applied Climatology*, *125*(3), 799-808.
- Kars, R., Reimann, T., Ankjærgaard, C., & Wallinga, J. (2014). Bleaching of the post-IR IRSL signal: new insights for feldspar luminescence dating. *Boreas*, *43*(4), 780-791.
- Kars, R., Reimann, T., & Wallinga, J. (2014). Are feldspar SAR protocols appropriate for post-IR IRSL dating? *Quaternary Geochronology*, *22*, 126-136.
- King, G. E., Herman, F., & Guralnik, B. (2016). Northward migration of the eastern Himalayan syntaxis revealed by OSL thermochronometry. *Science*, *353*(6301), 800-804.

- Koirala, A., Hanisch, J., & Geyh, M. (1997). *Recurrence history of debris flow events in Pokhara valley: A preview*. Paper presented at the Nepal Geological Congress, Kathmandu.
- Krbetschek, M., Götze, J., Dietrich, A., & Trautmann, T. (1997). Spectral information from minerals relevant for luminescence dating. *Radiation Measurements*, 27(5-6), 695-748.
- Kreutzer, S., Schmidt, C., Fuchs, M. C., Dietze, M., Fischer, M., & Fuchs, M. (2012). Introducing an R package for luminescence dating analysis. *Ancient TL*, 30(1), 1-8.
- Lavé, J., & Avouac, J. (2001). Fluvial incision and tectonic uplift across the Himalayas of central Nepal. *Journal of Geophysical Research: Solid Earth*, 106(B11), 26561-26591.
- Li, B., Jacobs, Z., Roberts, R., & Li, S.-H. (2014). Review and assessment of the potential of post-IR IRSL dating methods to circumvent the problem of anomalous fading in feldspar luminescence. *Geochronometria*, 41(3), 178-201.
- Madsen, A. T., Buylaert, J.-P., & Murray, A. S. (2011). Luminescence dating of young coastal deposits from New Zealand using feldspar. *Geochronometria*, 38(4), 379.
- McGuire, C., & Rhodes, E. J. (2015). Downstream MET-IRSL single-grain distributions in the Mojave River, southern California: Testing assumptions of a virtual velocity model. *Quaternary Geochronology*, 30, 239-244.
- Merritt, W. S., Letcher, R. A., & Jakeman, A. J. (2003). A review of erosion and sediment transport models. *Environmental Modelling & Software*, 18(8-9), 761-799.
- Murray, A., Thomsen, K. J., Masuda, N., Buylaert, J.-P., & Jain, M. (2012). Identifying well-bleached quartz using the different bleaching rates of quartz and feldspar luminescence signals. *Radiation Measurements*, 47(9), 688-695.
- Murray, A. S., Thomsen, K. J., Masuda, N., Buylaert, J. P., & Jain, M. (2012). Identifying well-bleached quartz using the different bleaching rates of quartz and feldspar luminescence signals. *Radiation Measurements*, 47(9), 688-695.
- Murray, A. S., & Wintle, A. G. (2000). Luminescence dating of quartz using an improved single-aliquot regenerative-dose protocol. *Radiation Measurements*, 32(1), 57-73.
- Murray, A. S., & Wintle, A. G. (2003). The single aliquot regenerative dose protocol: potential for improvements in reliability. *Radiation Measurements*, 37(4-5), 377-381.
- Nelson, M., Rittenour, T., & Cornachione, H. (2019). Sampling Methods for Luminescence Dating of Subsurface Deposits from Cores. *Methods and protocols*, 2(4), 88.
- Ollerhead, J., & Huntley, D. (2011). Optical dating of young feldspars: the zeroing question. *Ancient TL*, 29(2).
- Parsons, A. J., Law, R. D., Searle, M. P., Phillips, R. J., & Lloyd, G. E. (2016). Geology of the Dhaulagiri-Annapurna-Manaslu Himalaya, Western Region, Nepal. 1:200,000. *Journal of Maps*, 12(1), 100-110.
- Pietsch, T. J. (2009). Optically stimulated luminescence dating of young (<500 years old) sediments: Testing estimates of burial dose. *Quaternary Geochronology*, 4(5), 406-422.
- Pratt_Sitaula, B., Garde, M., W. Burbank, D., Oskin, M., Heimsath, A., & Gabet, E. (2007). Bedload-to-suspended load ratio and rapid bedrock incision from Himalayan landslide-dam lake record. *Quaternary Research*, 68(1), 111-12-.
- Prescott, J. R., & Hutton, J. T. (1994). Cosmic ray contributions to dose rates for luminescence and ESR dating: large depths and long-term time variations. *Radiation Measurements*, 23(2-3), 497-500.
- Preusser, F., Blei, A., Graf, H., & Schlüchter, C. (2007). Luminescence dating of Würmian (Weichselian) proglacial sediments from Switzerland: methodological aspects and stratigraphical conclusions. *Boreas*, 36(2), 130-142.
- Preusser, F., Chithambo, M. L., Götte, T., Martini, M., Ramseyer, K., Sendezera, E. J., . . . Wintle, A. G. (2009). Quartz as a natural luminescence dosimeter. *Earth-Science Reviews*, 97(1-4), 184-214.
- Preusser, F., Ramseyer, K., & Schlüchter, C. (2006). Characterisation of low OSL intensity quartz from the New Zealand Alps. *Radiation Measurements*, 41(7-8), 871-877.
- Rajaure, S., & Paudel, L. P. (2018). A comprehensive earthquake catalogue for Nepal and its adjoining region. *Journal of Nepal Geological Society*, 56(1), 65-72.

- Rajendran, K., Parameswaran, R. M., & Rajendran, C. P. (2017). Seismotectonic perspectives on the Himalayan arc and contiguous areas: Inferences from past and recent earthquakes. *Earth-Science Reviews*, 173, 1-30.
- Reimann, T., Notenboom, P. D., De Schipper, M. A., & Wallinga, J. (2015). Testing for sufficient signal resetting during sediment transport using a polymineral multiple-signal luminescence approach. *Quaternary Geochronology*, 25, 26-36.
- Reimann, T., Román-Sánchez, A., Vanwalleghem, T., & Wallinga, J. (2017). Getting a grip on soil reworking – Single-grain feldspar luminescence as a novel tool to quantify soil reworking rates. *Quaternary Geochronology*, 42, 1-14.
- Reimann, T., Thomsen, K. J., Jain, M., Murray, A. S., & Frechen, M. (2012). Single-grain dating of young sediments using the pIRIR signal from feldspar. *Quaternary Geochronology*, 11, 28-41.
- Reimann, T., Tsukamoto, S., Naumann, M., & Frechen, M. (2011). The potential of using K-rich feldspars for optical dating of young coastal sediments—A test case from Darss-Zingst peninsula (southern Baltic Sea coast). *Quaternary Geochronology*, 6(2), 207-222.
- Rhodes, E. J. (2011). Optically Stimulated Luminescence Dating of Sediments over the Past 200,000 Years. *Annual Review of Earth and Planetary Sciences*, 39(1), 461-488.
- Riedesel, S., Brill, D., Roberts, H. M., Duller, G. A., Garrett, E., Zander, A. M., . . . Cunningham, A. (2018). Single-grain feldspar luminescence chronology of historical extreme wave event deposits recorded in a coastal lowland, Pacific coast of central Japan. *Quaternary Geochronology*, 45, 37-49.
- Rimal, B., Baral, H., Stork, N. E., Paudyal, K., & Rijal, S. (2015). Growing City and Rapid Land Use Transition: Assessing Multiple Hazards and Risks in the Pokhara Valley, Nepal. *Land*, 4(4), 957-978.
- Roback, K., Clark, M. K., West, A. J., Zekkos, D., Li, G., Gallen, S. F., ... & Godt, J. W. (2018). The size, distribution, and mobility of landslides caused by the 2015 Mw7. 8 Gorkha earthquake, Nepal. *Geomorphology*, 301, 121-138.
- Roberts, H. M. (2012). Testing Post-IR IRSL protocols for minimising fading in feldspars, using Alaskan loess with independent chronological control. *Radiation Measurements*, 47(9), 716-724.
- Rodnight, H., Duller, G., Wintle, A., & Tooth, S. (2006). Assessing the reproducibility and accuracy of optical dating of fluvial deposits. *Quaternary Geochronology*, 1(2), 109-120.
- Rosati, J. D. (2005). Concepts in sediment budgets. *Journal of Coastal Research*, 307-322.
- Sawakuchi, A. O., Jain, M., Mineli, T. D., Nogueira, L., Bertassoli, D. J., Häggi, C., . . . Cunha, D. F. (2018). Luminescence of quartz and feldspar fingerprints provenance and correlates with the source area denudation in the Amazon River basin. *Earth and Planetary Science Letters*, 492, 152-162.
- Schwanghart, W., Bernhardt, A., Stolle, A., Hoelzmann, P., Adhikari, B. R., Andermann, C., . . . Korup, O. (2016). Repeated catastrophic valley infill following medieval earthquakes in the Nepal Himalaya. *Science*, 351(6269), 147-150.
- Smedley, R., Duller, G., & Roberts, H. (2015). Bleaching of the post-IR IRSL signal from individual grains of K-feldspar: Implications for single-grain dating. *Radiation Measurements*, 79, 33-42.
- Smedley, R. K. (2014). *Testing the use of single grains of K-feldspar for luminescence dating of proglacial sediments in Patagonia*. Aberystwyth University,
- Sohbati, R., Borella, J., Murray, A., Quigley, M., & Buylaert, J. P. (2016). Optical dating of loessic hillslope sediments constrains timing of prehistoric rockfalls, Christchurch, New Zealand. *Journal of Quaternary Science*, 31(7), 678-690.
- Spooner, N. A. (1994). The anomalous fading of infrared-stimulated luminescence from feldspars. *Radiation Measurements*, 23(2-3), 625-632.
- Stokes, S., Bray, H., & Blum, M. (2001). Optical resetting in large drainage basins: tests of zeroing assumptions using single-aliquot procedures. *Quaternary Science Reviews*, 20(5-9), 879-885.
- Stolle, A., Bernhardt, A., Schwanghart, W., Hoelzmann, P., Adhikari, B. R., Fort, M., & Korup, O. (2017). Catastrophic valley fills record large Himalayan earthquakes, Pokhara, Nepal. *Quaternary Science Reviews*, 177, 88-103.

- Tatumi, S. H., Peixoto, M. N. O., Moura, J. R. S., Mello, C. L., Carmo, I. O., Kowata, E. A., . . . Kassab, L. R. P. (2003). Optical dating using feldspar from Quaternary alluvial and colluvial sediments from SE Brazilian Plateau, Brazil. *Journal of Luminescence*, *102-103*, 566-570.
- Taylor, L. L., Quirk, J., Thorley, R. M. S., Kharecha, P. A., Hansen, J., Ridgwell, A., . . . Beerling, D. J. (2016). Enhanced weathering strategies for stabilizing climate and averting ocean acidification. *Nature Climate Change*, *6*(4), 402-406.
- Thomsen, K. J., Murray, A. S., Buylaert, J.-P., Jain, M., Hansen, J., & Aubry, T. (2016). Testing single-grain quartz OSL methods using sediment samples with independent age control from the Bordes-Fitte rockshelter (Roches d'Abilly site, Central France). *Quaternary Geochronology*, *31*, 77-96.
- Thomsen, K. J., Murray, A. S., Jain, M., & Bøtter-Jensen, L. (2008). Laboratory fading rates of various luminescence signals from feldspar-rich sediment extracts. *Radiation Measurements*, *43*(9-10), 1474-1486.
- Tucker, G. E., & Hancock, G. R. (2010). Modelling landscape evolution. *Earth Surface Processes and Landforms*, *35*(1), 28-50.
- Walker, M. (2005). *Quaternary dating methods*: John Wiley and Sons.
- Wallinga, J. (2002). Optically stimulated luminescence dating of fluvial deposits: a review. *Boreas*, *31*(4), 303-322.
- Wallinga, J., Bos, A. J. J., Dorenbos, P., Murray, A. S., & Schokker, J. (2007). A test case for anomalous fading correction in IRSL dating. *Quaternary Geochronology*, *2*(1), 216-221.
- Wallinga, J., Murray, A., & Duller, G. (2000). Underestimation of equivalent dose in single-aliquot optical dating of feldspars caused by preheating. *Radiation Measurements*, *32*(5), 691-695.
- Weltje, G. J., & von Eynatten, H. (2004). Quantitative provenance analysis of sediments: review and outlook. *Sedimentary Geology*, *171*(1-4), 1-11.
- Wintle, A. G. (1973). Anomalous fading of thermo-luminescence in mineral samples. *Nature*, *245*(5421), 143-144.
- Wintle, A. G. (2008). Luminescence dating: where it has been and where it is going. *Boreas*, *37*(4), 471-482.
- Wintle, A. G., & Murray, A. S. (2006). A review of quartz optically stimulated luminescence characteristics and their relevance in single-aliquot regeneration dating protocols. *Radiation Measurements*, *41*(4), 369-391.
- Yamanaka, H. (1982). Radiocarbon ages of upper Quaternary deposit in central Nepal and their geomorphological significance. *Science Reports of the Tohoku University, 7th Series, Geography*, *32*(1), 46-60.
- Zervas, D., Nichols, G. J., Hall, R., Smyth, H. R., Lüthje, C., & Murtagh, F. (2009). SedLog: A shareware program for drawing graphic logs and log data manipulation. *Computers & Geosciences*, *35*(10), 2151-2159.

Appendix

Appendix I: Measurement sequences

Appendix I Table I: Multi-grain Quartz IR test measurement protocol, which is a preliminary test to check if quartz grains are suitable for luminescence dating in this field setting.

Multi-grain quartz IR test protocol: sample NCL-7619124 and -125		
Step	Treatment	Measurement
1	Natural or regenerative dose	
2	Preheat at 220 °C for 10 s	
3	IR LED at 30 °C for 40 s	
4	Blue LED OSL at 125 °C for 20 s	Lx
5	Test dose: 3 Gy	
6	Preheat at 200 °C for 10 s	
7	Blue LED OSL at 125 °C for 20 s	Tx
8	Hot-bleach at 230 °C for 40 s	
	Repeat steps 1 till 8 for irradiation [Gy]: Natural – 5 – 10 – 20 – 0 – 5 – 5	

Appendix I Table II: Single-grain feldspar dose recovery test measurement protocol, which is a test to assess the residual dose (first irradiation cycle – one discs) and dose recovery (second irradiation cycle – two different discs) of the sample set.

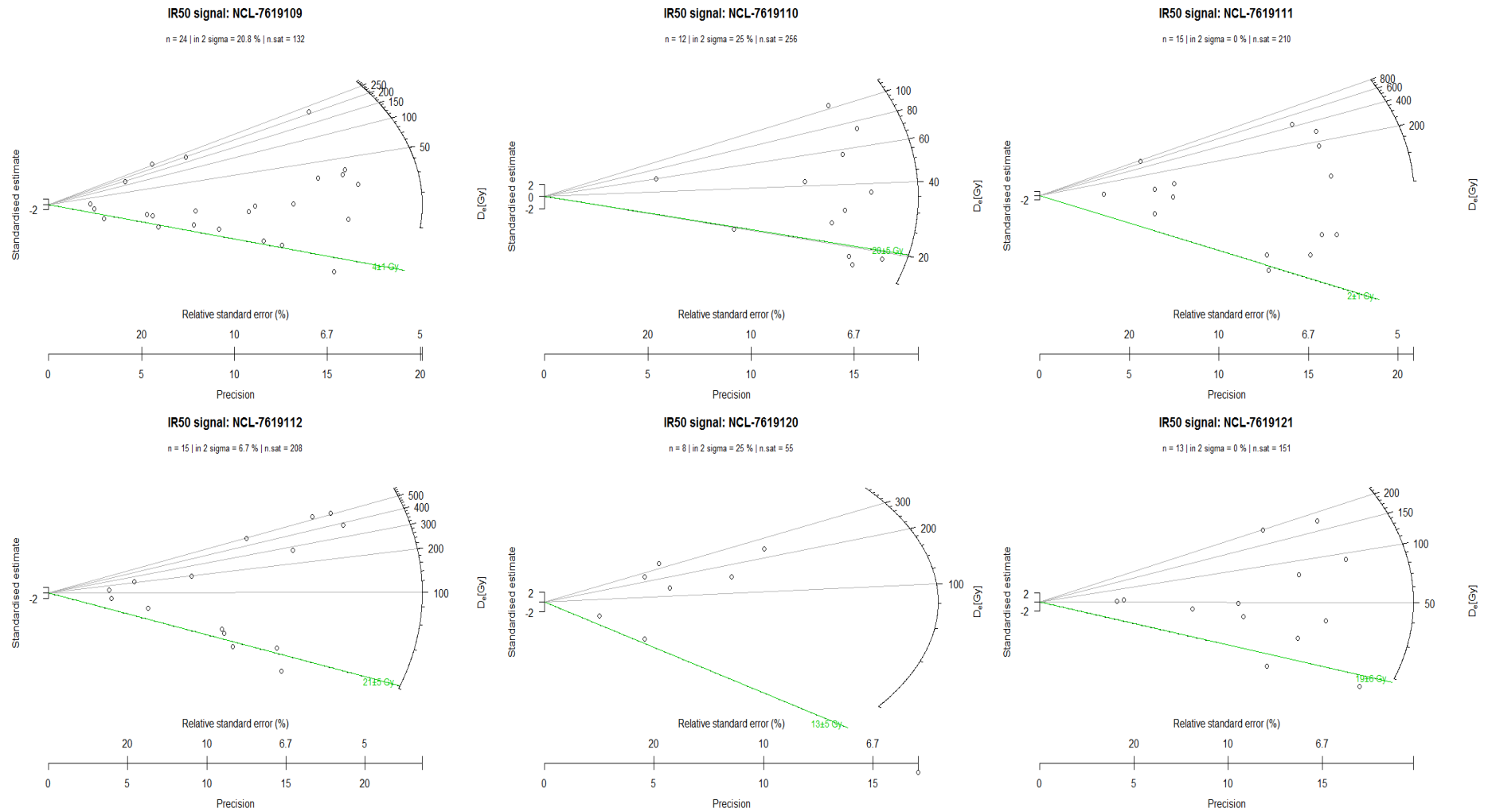
Single-grain feldspar dose recovery test protocol: sample NCL-7619125		
Step	Treatment	Measurement
1	Natural or regenerative dose	
2	Preheat at 175 °C for 120 s	
3	SG infrared stimulation at 50 °C for 2 s	Lx – IRSL50
4	SG infrared stimulation at 150 °C for 2 s	Lx – pIRIR150
5	Test dose: 10 Gy	
6	Preheat at 175 °C for 120 s	
7	SG infrared stimulation at 50 °C for 2 s	Tx – IRSL50
8	SG infrared stimulation at 150 °C for 2 s	Tx – pIRIR150
9	IR wash at 150 °C for 500 s	
	Repeat steps 1 till 9 for irradiation [Gy]: Natural – 5 – 10 – 0 – 5 (residual dose) AND 15 – 10 – 20 – 40 – 80 – 0 – 25 (dose recovery)	

Appendix I Table III: Multi-grain feldspar fading test measurement protocol. This sequence is however, complemented by pauses in order to measure the anomalous fading after different delay times. The sequence is organised in such a way that it is time-wise most efficient. The time between irradiation and first prompt measurements is 172800 seconds (2 days).

Multi-grain feldspar fading test protocol: samples NCL-7619109, -111, -122 and -123		
Step	Treatment	Measurement
1	Natural or regenerative dose	
2	Preheat at 175 °C for 120 s	
3	MG infrared stimulation at 50 °C for 100 s	Lx – IRSL50
4	MG infrared stimulation at 150 °C for 100 s	Lx – pIRIR150
5	Test dose: 5 Gy	
6	Preheat at 175 °C for 120 s	
7	MG infrared stimulation at 50 °C for 100 s	Tx – IRSL50
8	MG infrared stimulation at 150 °C for 100 s	Tx – pIRIR150
9	MG infrared stimulation at 150 °C for 500 s	
	Repeat steps 1 till 9 for irradiation [Gy]: Natural – 10 – 10 – pause 500 s – 10 – 10 – 10	

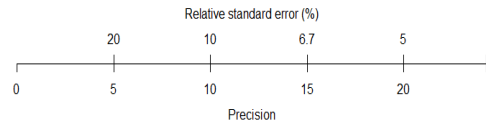
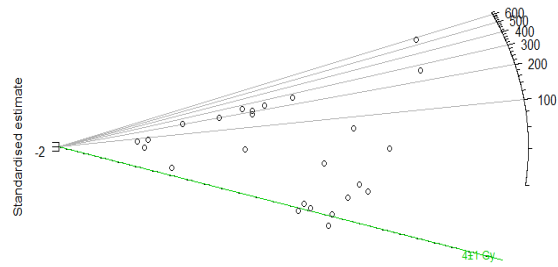
Appendix II: Radial plots

Appendix II Table I: Radial plots showing the dose equivalent (D_e) spread per sample for the IRSL50 signal. The green line indicates the paleodose [Gy] by the bootstrapped Minimum Age Model (bootMAM) ($\sigma = 0.3$) and its corresponding uncertainty. Moreover, the number of grains used to calculate the paleodose (data points in plot) and the number of grains in saturation (not shown grains) are stated in the subtitle.



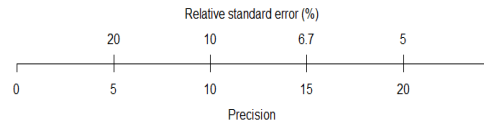
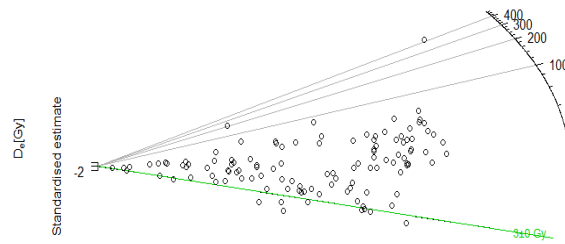
IR50 signal: NCL-7619122

n = 25 | in 2 sigma = 12 % | n.sat = 195



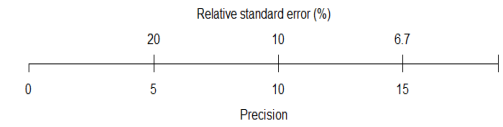
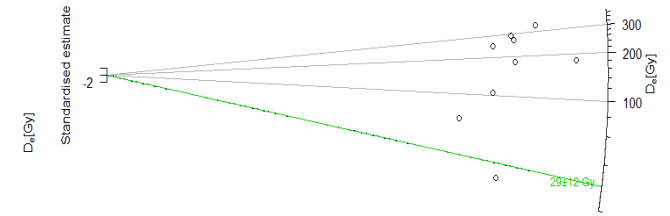
IR50 signal: NCL-7619123

n = 116 | in 2 sigma = 11.2 % | n.sat = 75



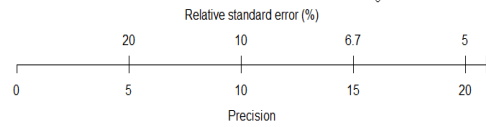
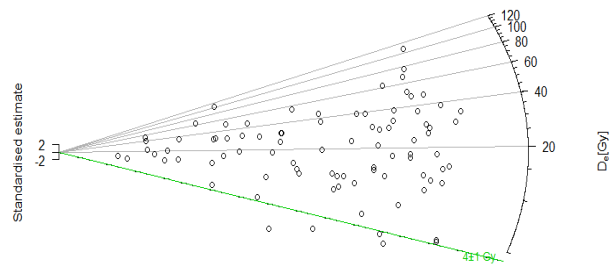
IR50 signal: NCL-7619124

n = 9 | in 2 sigma = 0 % | n.sat = 224

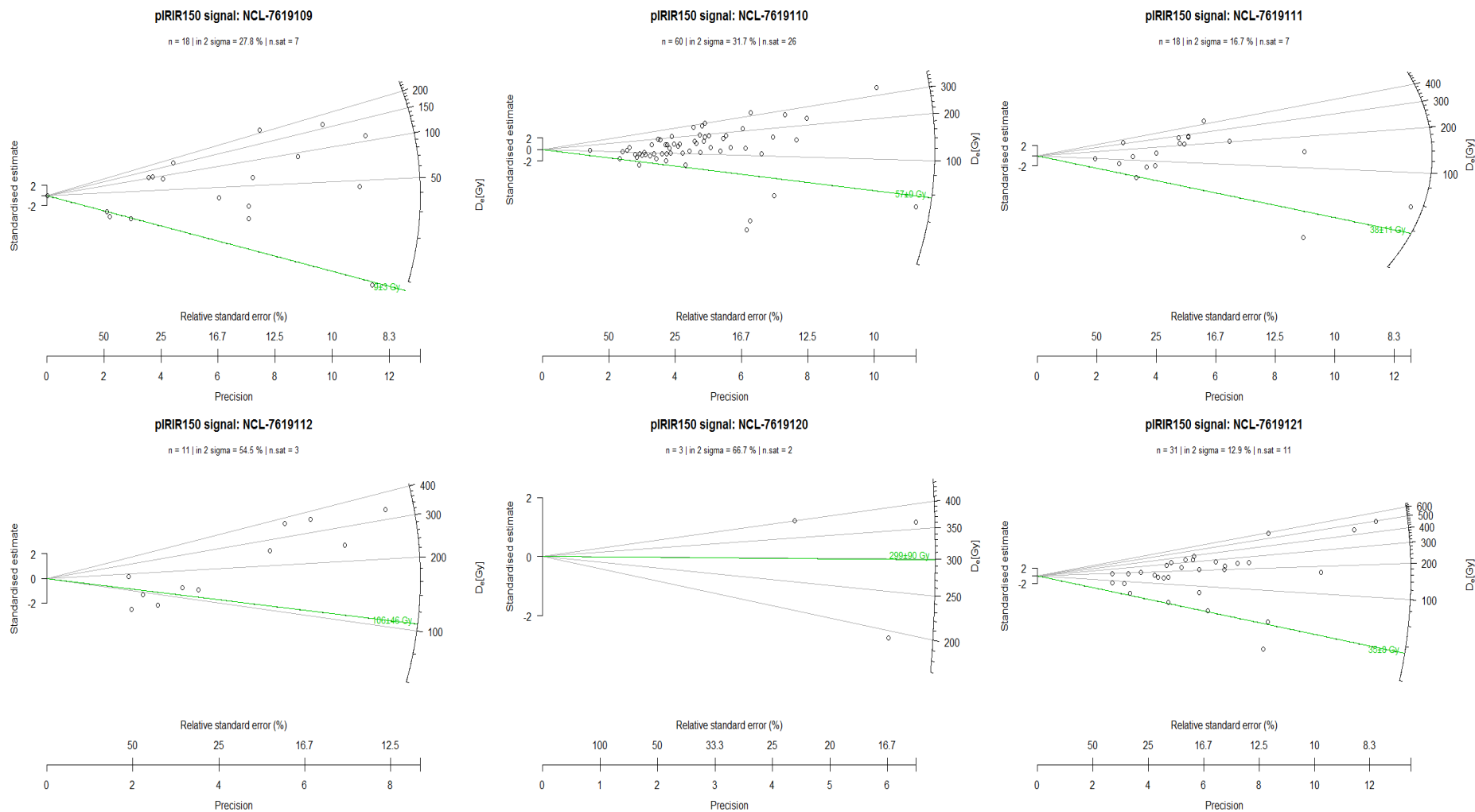


IR50 signal: NCL-7619125

n = 90 | in 2 sigma = 5.6 % | n.sat = 166

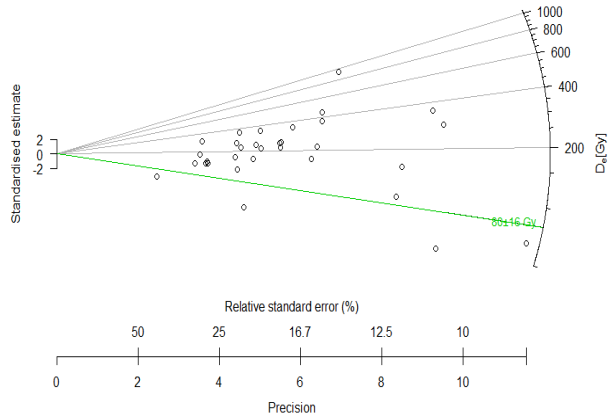


Appendix II Table II: Radial plots showing the dose equivalent (D_e) spread per sample for the pIRIR150 signal. The green line indicates the paleodose [Gy] by the bootstrapped Minimum Age Model (bootMAM) ($\sigma = 0.3$) and its corresponding uncertainty. Moreover, the number of grains used to calculate the paleodose (data points in plot) and the number of grains in saturation (not shown grains) are stated in the subtitle.



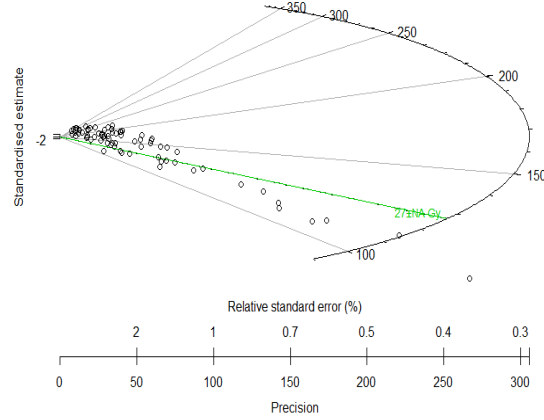
PIRIR150 signal: NCL-7619122

n = 32 | in 2 sigma = 18.8 % | n.sat = 13



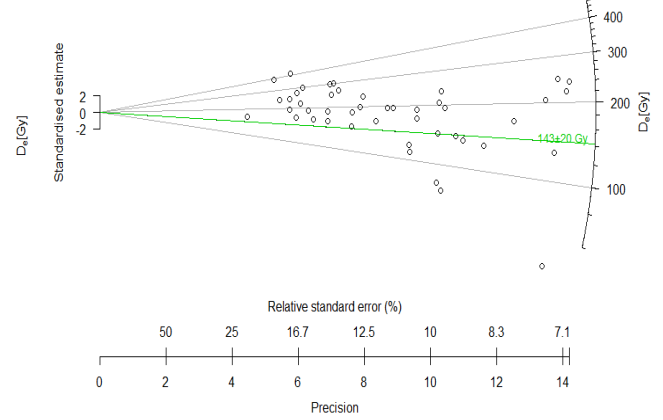
PIRIR150 signal: NCL-7619123

n = 76 | in 2 sigma = 9.2 % | n.sat = 11



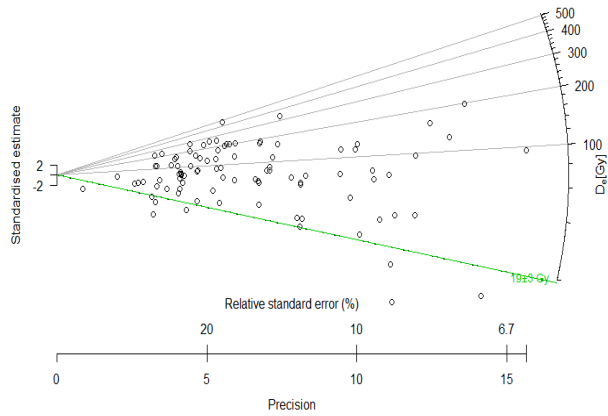
PIRIR150 signal: NCL-7619124

n = 45 | in 2 sigma = 37.8 % | n.sat = 24



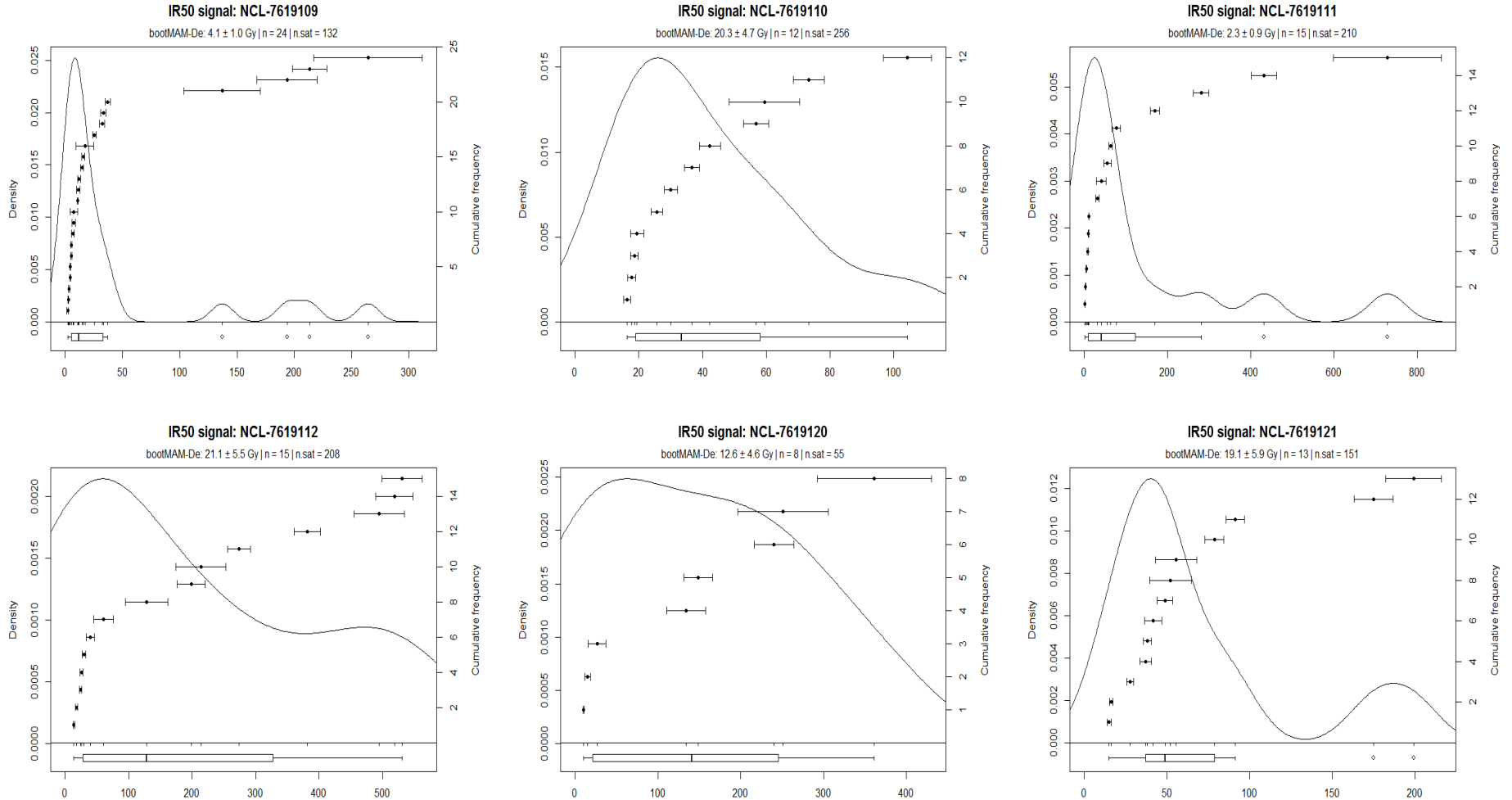
PIRIR150 signal: NCL-7619125

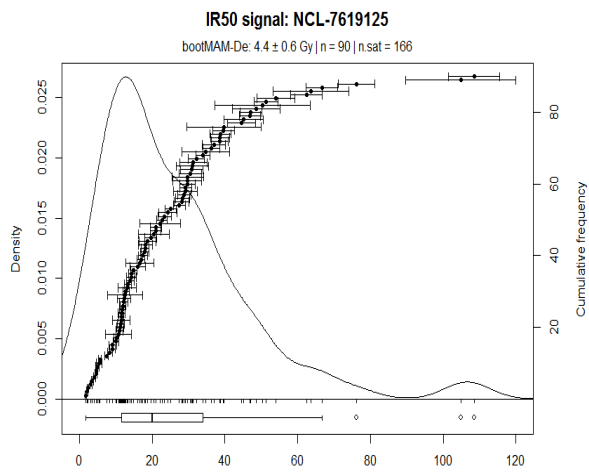
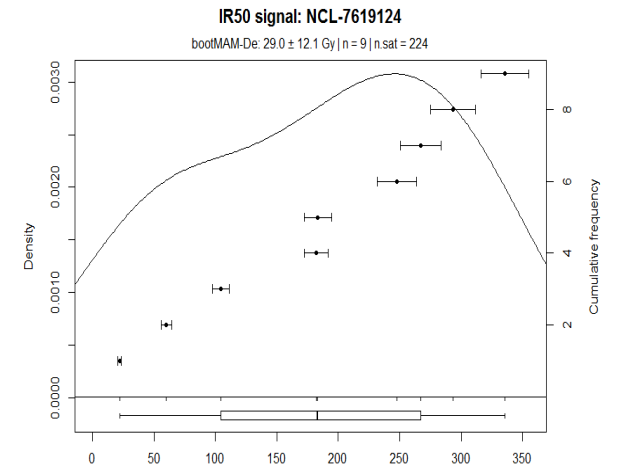
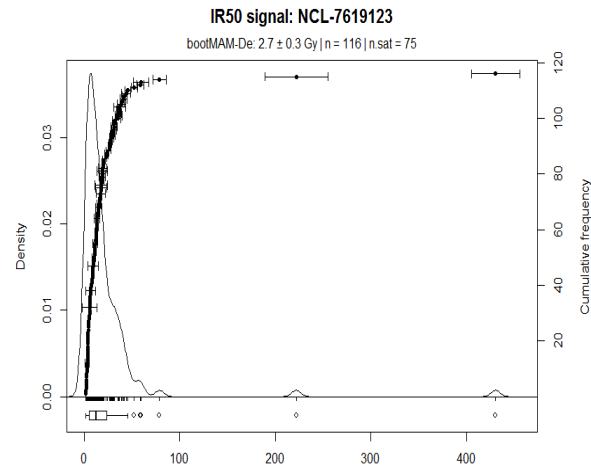
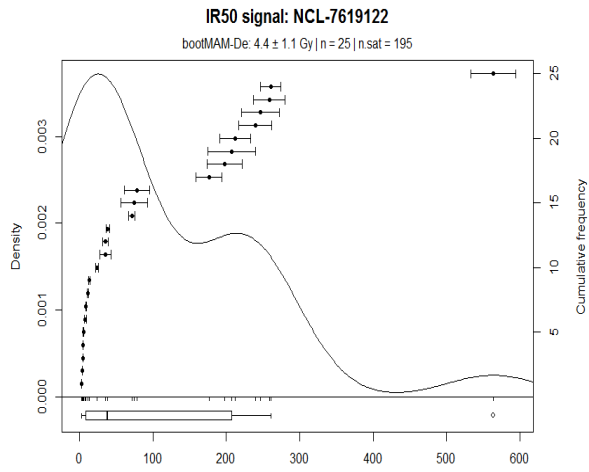
n = 94 | in 2 sigma = 16 % | n.sat = 22



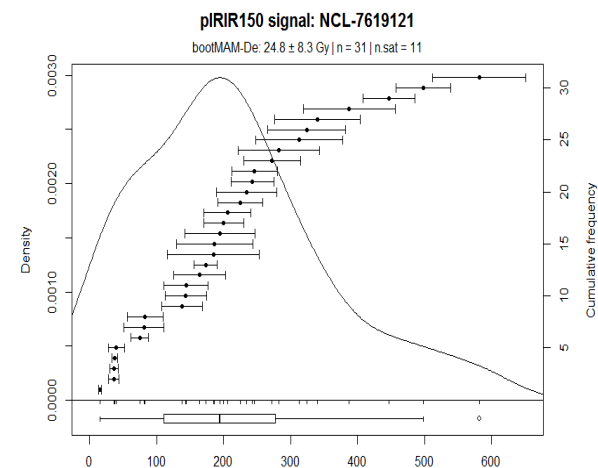
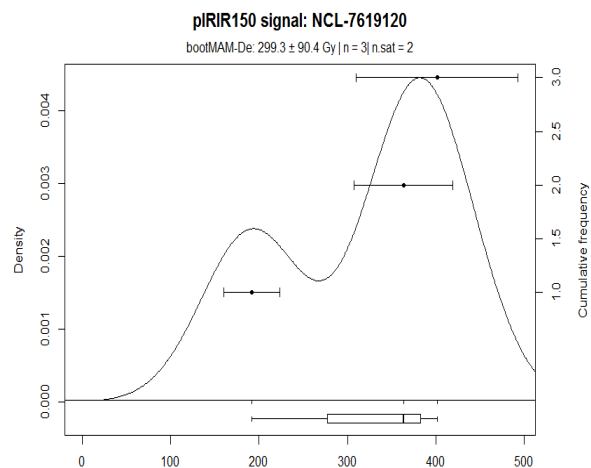
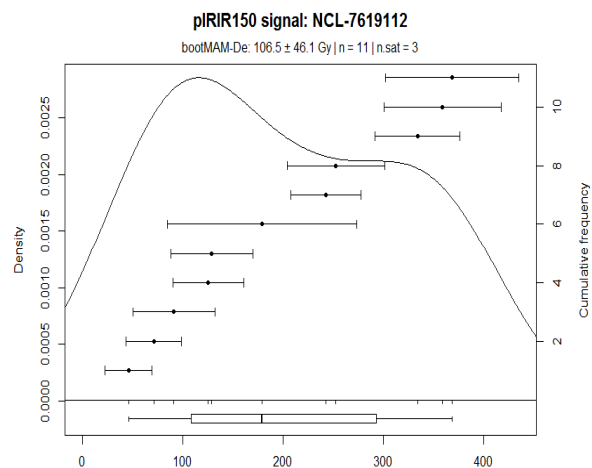
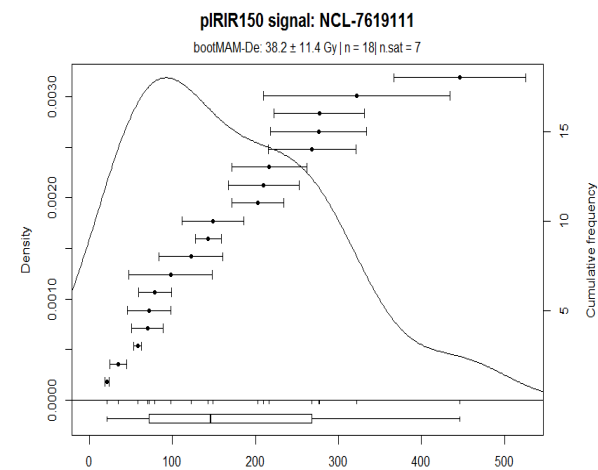
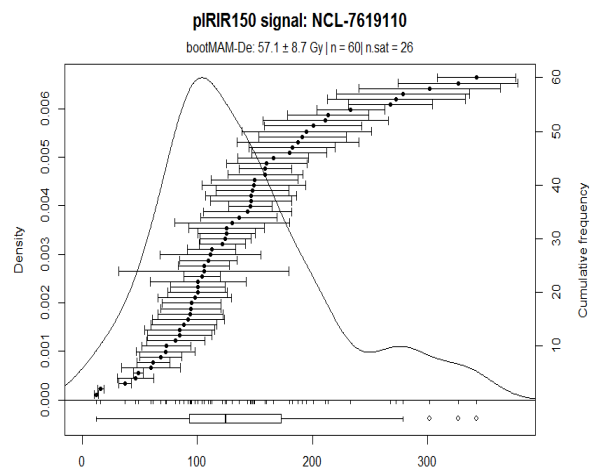
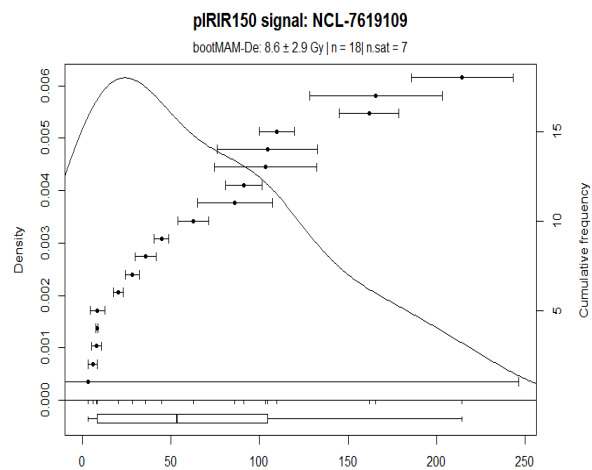
Appendix III: Kernel Density plots

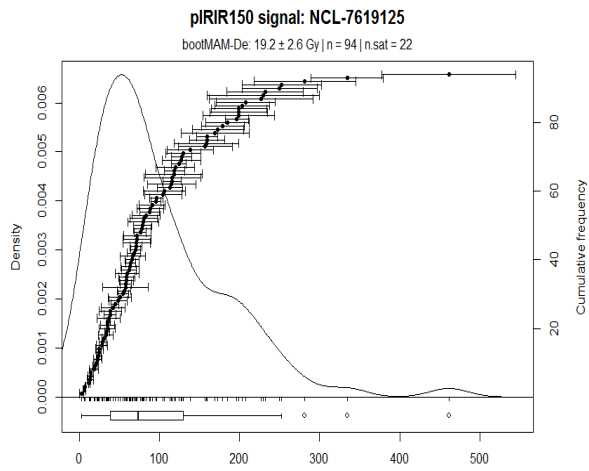
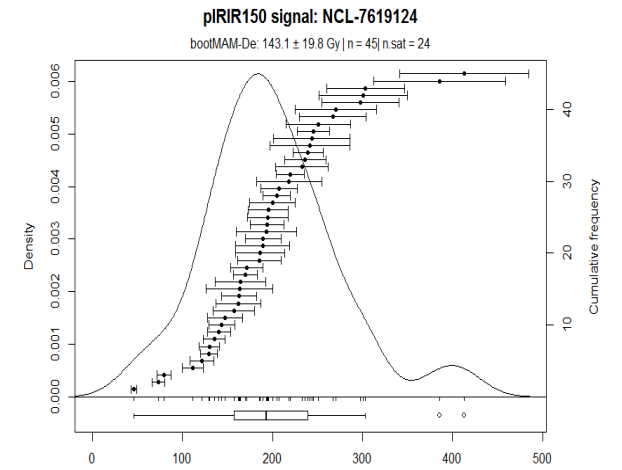
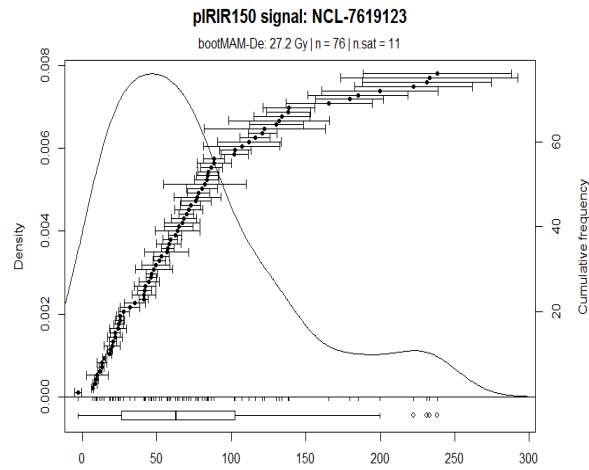
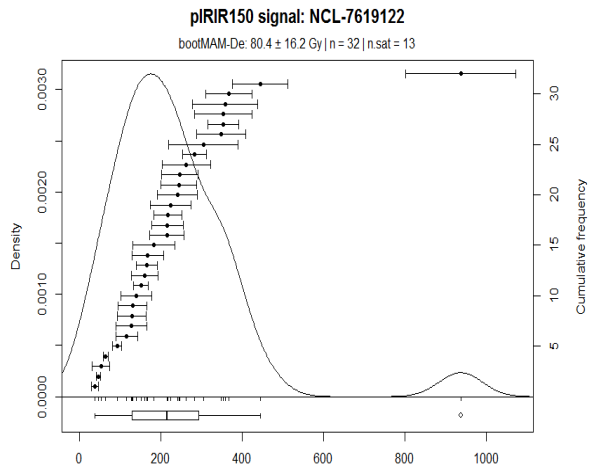
Appendix III Table I: Kernel Density plots showing the dose equivalent (De) spread and its corresponding density per sample for the IRSL50 signal. Moreover, the bootMAM determined De paleodose (sigmab = 0.3), the number of grains used to calculate the paleodose (data points in plot) and the number of grains in saturation (not shown grains) are stated in the subtitle.









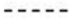





Appendix III Table II: Kernel Density plots showing the dose equivalent (De) spread and its corresponding density per sample for the pIRIR150 signal. Moreover, the bootMAM determined De paleodose ($\sigma_{\text{bootMAM}} = 0.3$), the number of grains used to calculate the paleodose (data points in plot) and the number of grains in saturation (not shown grains) are stated in the subtitle.



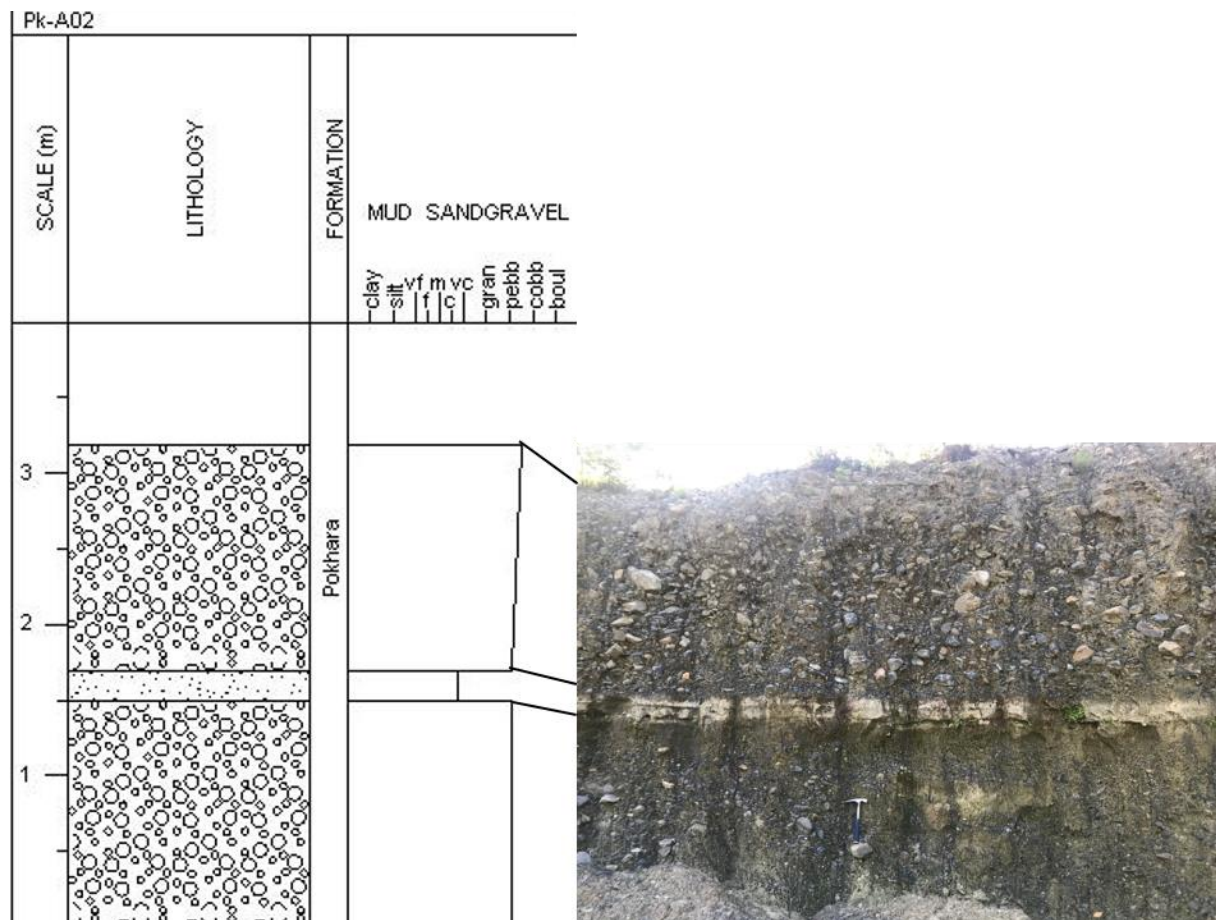


Appendix IV: Sedimentary logs

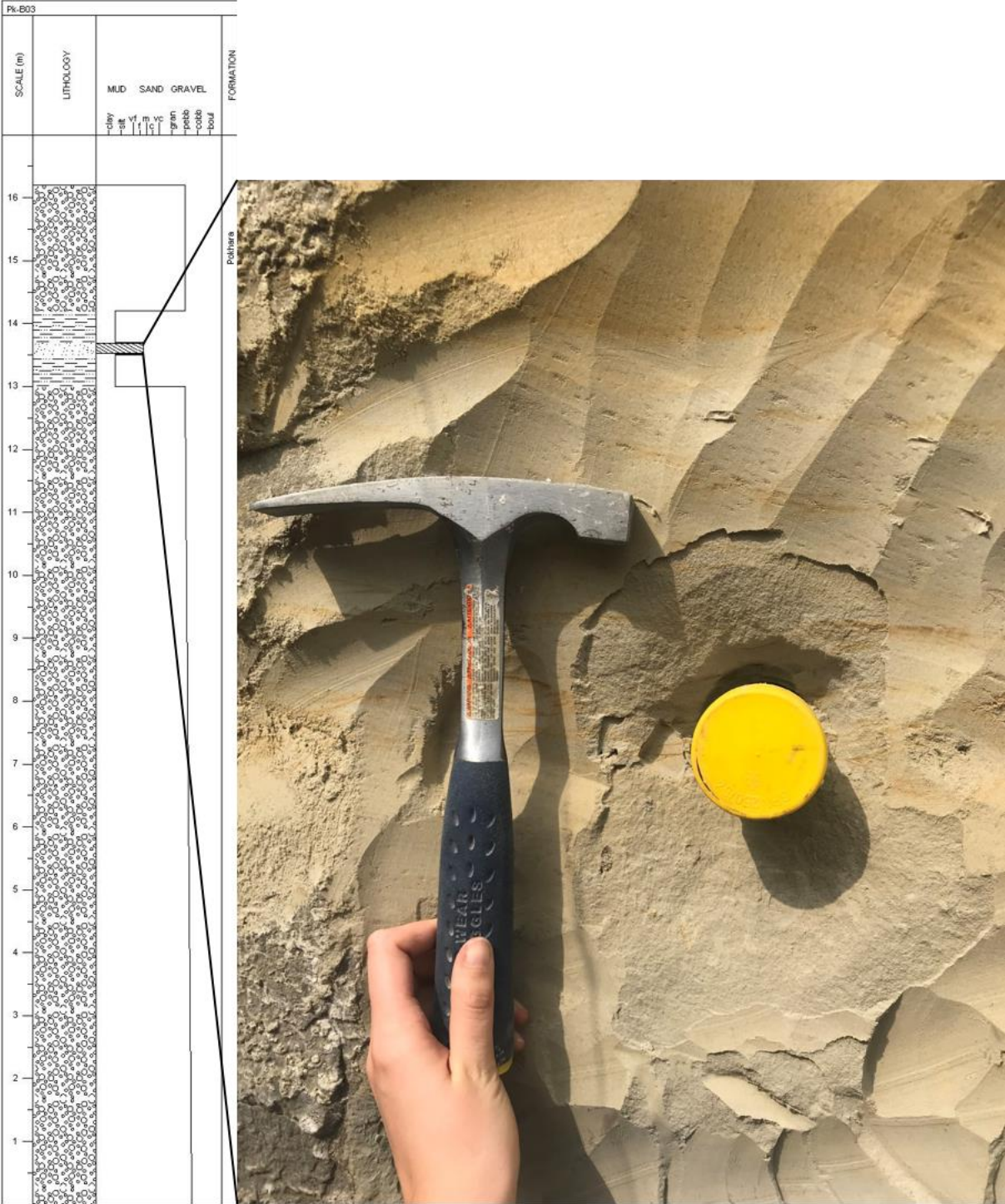
Appendix IV Table I: Legend of the sedimentary logs with indications for the lithology, the base boundaries and other types of symbols.

Lithologies	Base Boundaries	Symbols
 Sand bodies	 Sharp	 Rip-up clast
 Slackwater deposits	 Gradational	 Planar cross-bedding
 Matrix-supported conglomerate	 Erosion	
 Clast-supported conglomerate		
 Phyllite		

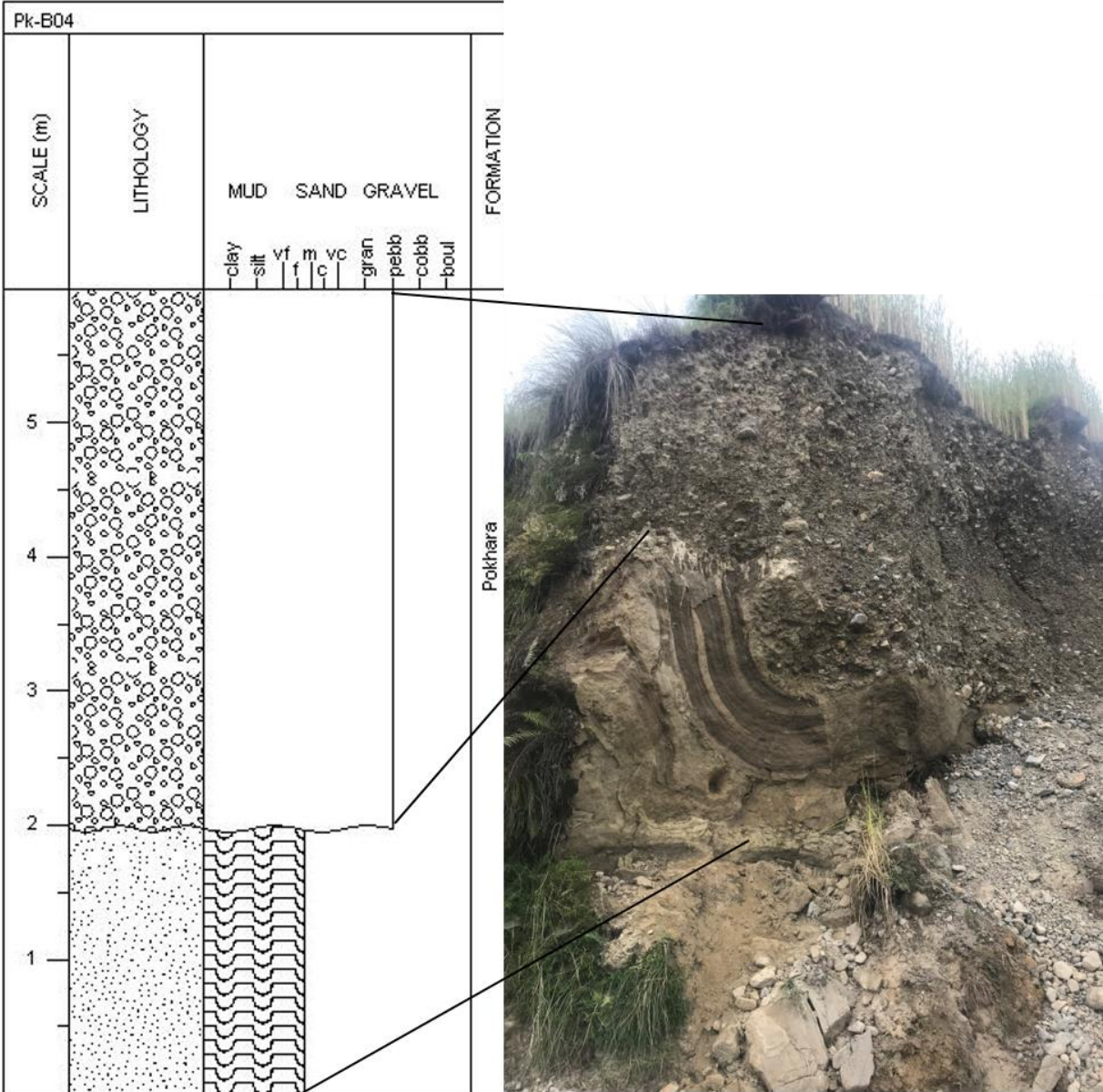
Appendix IV Table II: Sedimentary log and field picture of sample location Pk-A02 corresponding to NCL-7619109.



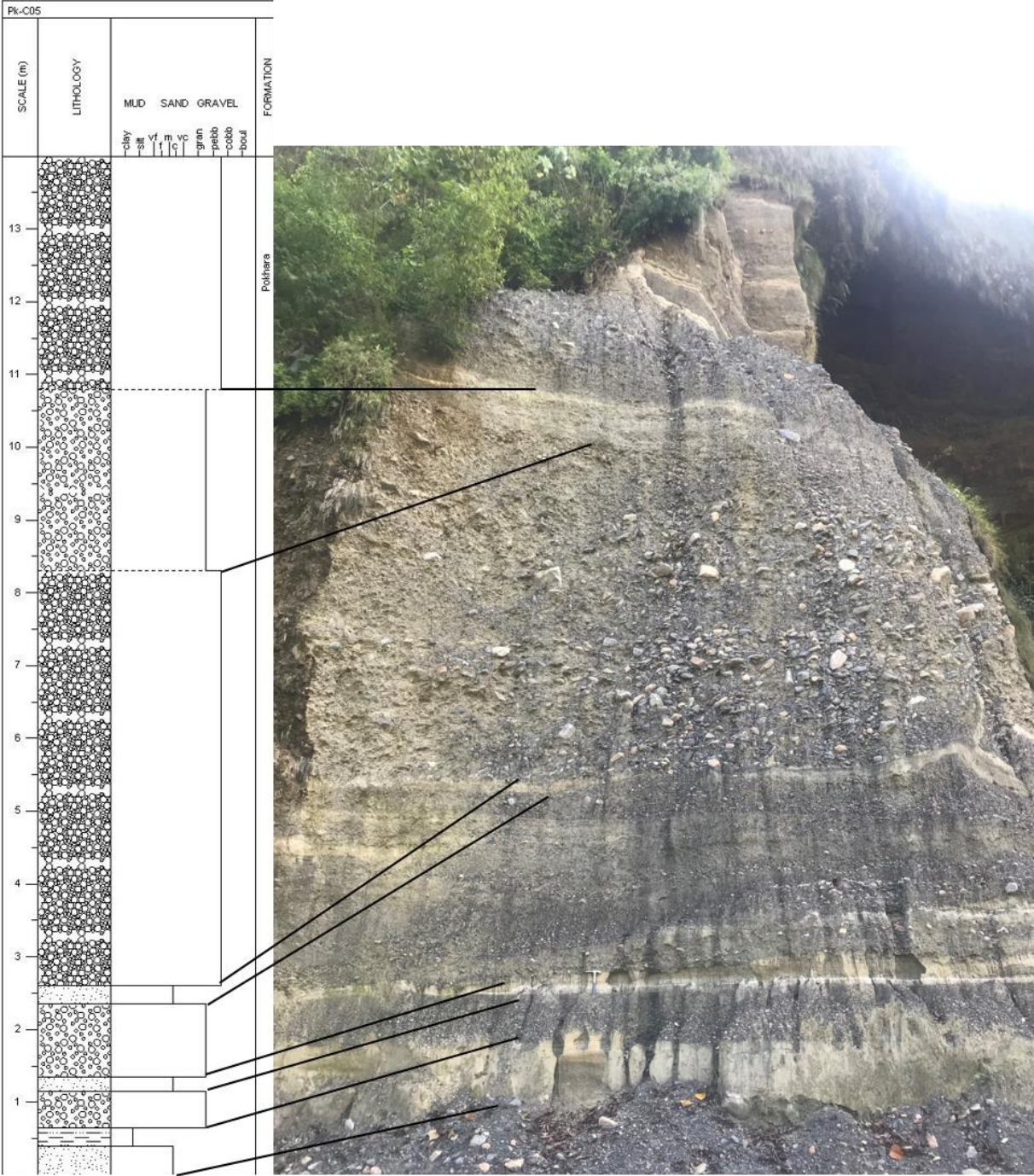
Appendix IV Table III: Sedimentary log and field picture of sample location Pk-B03 corresponding to NCL-7619110.



Appendix IV Table IV: Sedimentary log and field picture of sample location Pk-B04 corresponding to NCL-7619111.



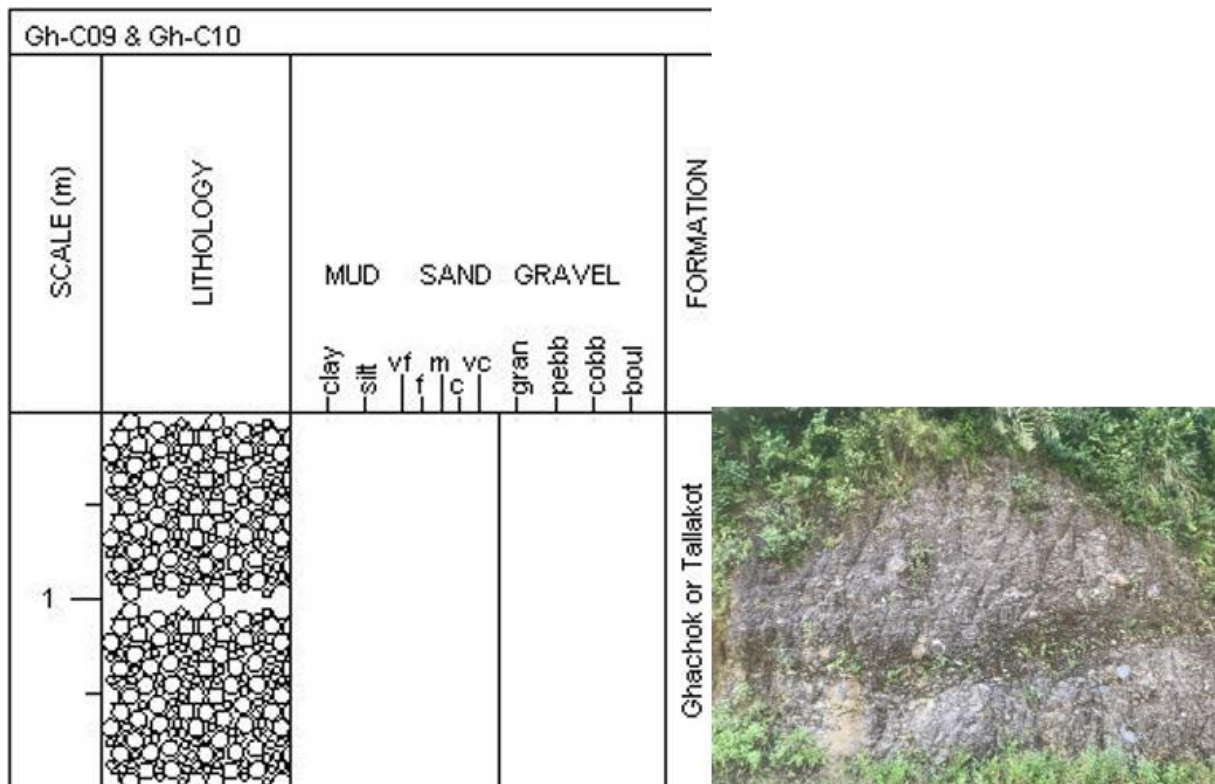
Appendix IV Table V: Sedimentary log and field picture of sample location Pk-C05 corresponding to NCL-7619112.



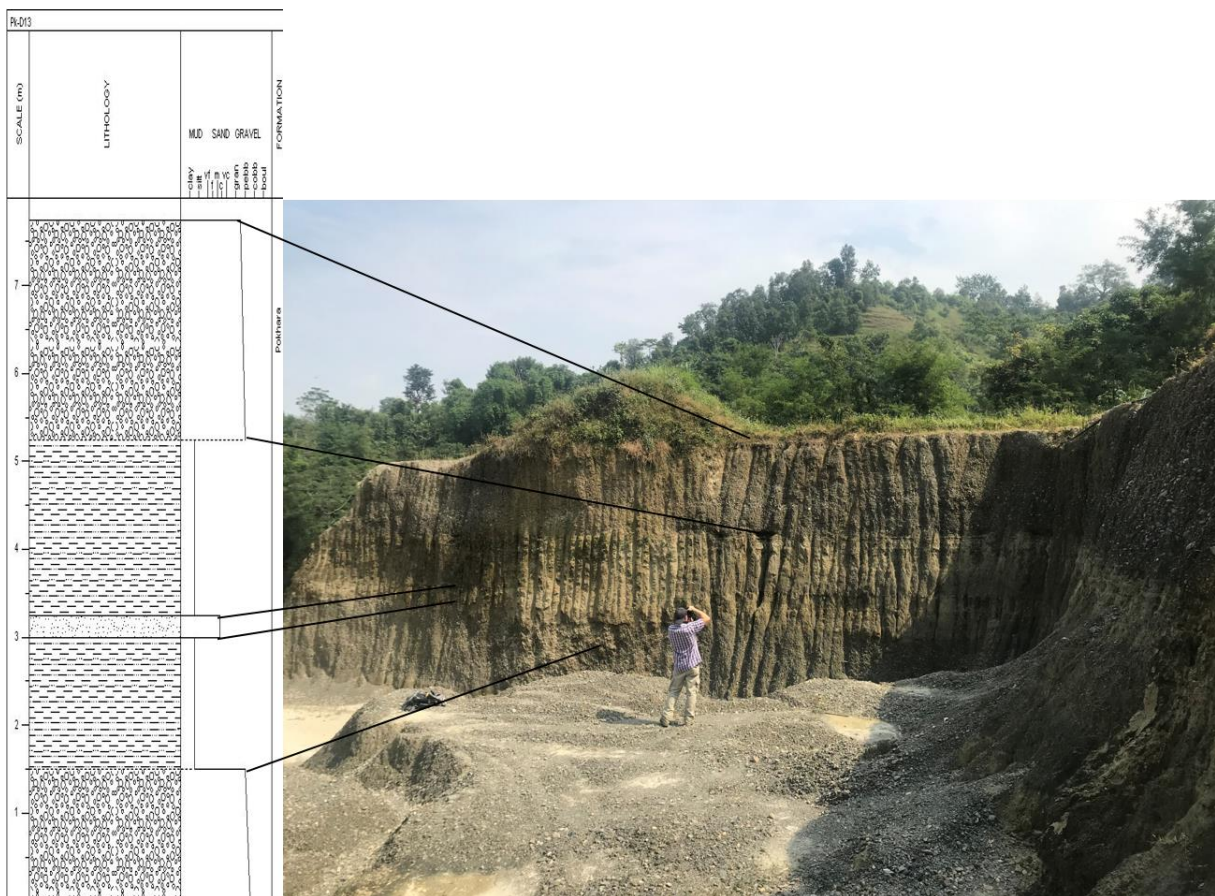
Appendix IV Table VI: Sedimentary log and field picture of sample location Gh-C07 & Gh-C08 corresponding to NCL-7619114 and -115.



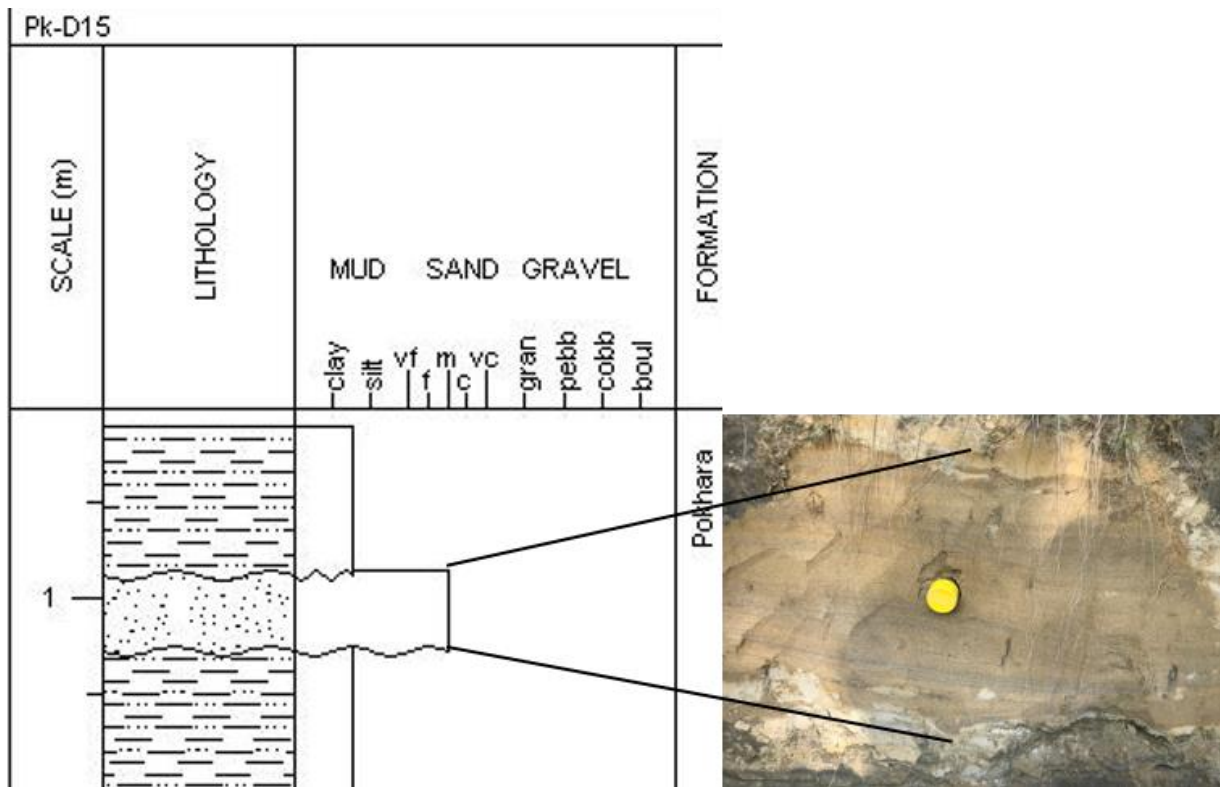
Appendix IV Table VII: Sedimentary log and field picture of sample location Gh-C09 & Gh-C10 corresponding to NCL-7619116 and -117.



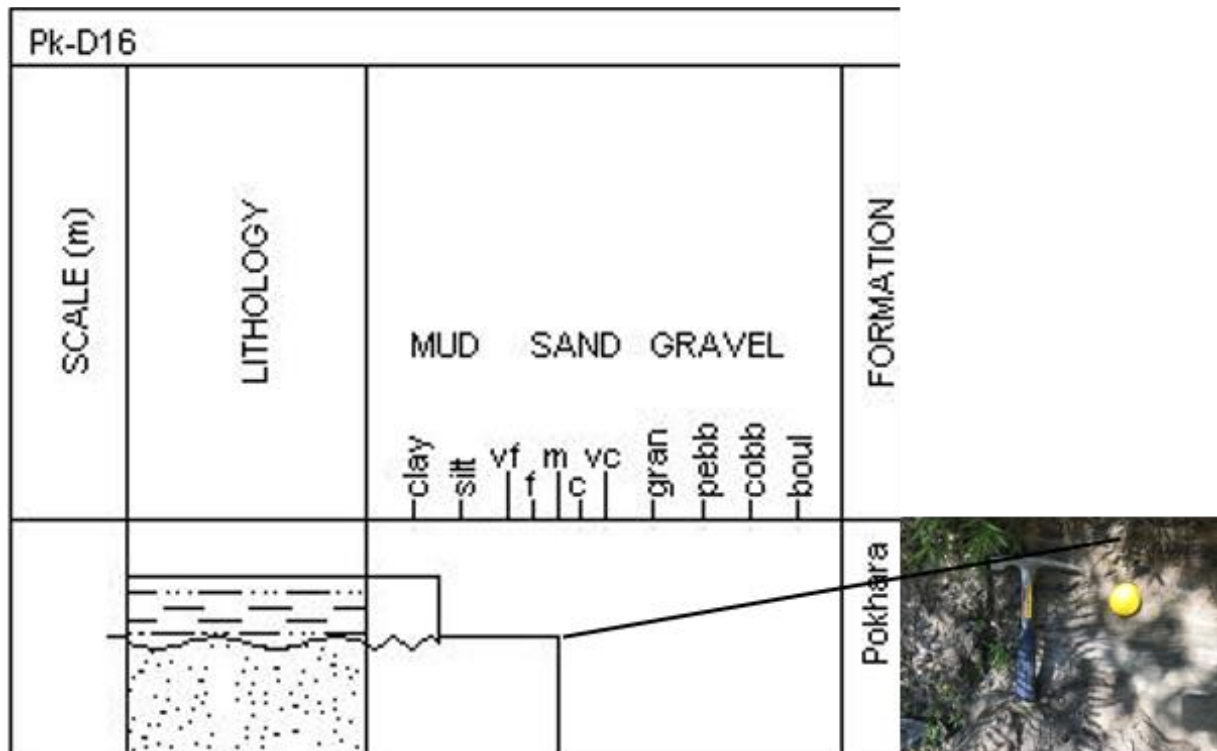
Appendix IV Table VIII: Sedimentary log and field picture of sample location PK-D13 corresponding to NCL-7619120.



Appendix IV Table IX: Sedimentary log and field picture of sample location Pk-D15 corresponding to NCL-7619122.



Appendix IV Table X: Sedimentary log and field picture of sample location Pk-D16 corresponding to NCL-7619123.



Appendix V: Snapping distance

Appendix V Table I: Snapping distance (distance between OSL sample location and main river network (Seti Khola)) displayed against the frequency of sampling.

